A Joint Search for Gravitational Wave Bursts by the AURIGA Resonant Detector and the LIGO Interferometer Observatories

Silvia Poggi

Department of Physics

University of Trento - Italy

Supervisor: prof. Giovanni A. Prodi

A thesis submitted for the degree of

Doctor of Philosophy

Trento - February 17, 2006

To Andrea, who motivate me to continue this work. Thank you for your suggestions, your patience, and your daily encouragement.

Abstract

This PhD thesis describes issues and methodological aspects concerning the first collaboration to search gravitational waves bursts with non-homogeneous detectors. The work included in the thesis is representative of a small number of individuals and is still under review from the LSC and AURIGA collaboration, thus subject to possible revision before publication.

The resonant gravitational wave detector AURIGA and the LIGO interferometric observatories were simultaneously acquiring data for the first time in a 2-weeks period from the end of 2003. The first effort of the two collaborations towards a joint analysis forced us to face the challenge of a coincidence between detectors with different spectral sensitivity, bandwidth and antenna pattern.

I will start presenting a study of the directional sensitivity of the network. In particular, different strategies have been compared to combine the different antenna pattern of each detector and quantify the directional sensitivity of the network as a whole. The study has been completed considering the hypothesis of reorienting the bar. In addition to the difference in directional sensitivity, another aspect which must be taken into account in dealing with a network of non-homogeneous detectors is the different sensitivity band. To overcome the problem, a search strategy has been developed which performs a broad-band cross correlation between the LIGO interferometers triggered by AURIGA events in the 850-950 Hz band.

This work describes the analysis strategy and the results of the search. It is important to stress that, because of non-optimal performances of the detectors and the short duration of the coincident run, the

relevance of this work is mostly methodological. Results must be interpreted by taking into account the uncertainties which affects our estimation of the “off-source” accidental coincidences.

Contents

List of Figures

Chapter 1

Introduction

From December 24, 2003 to January 9, 2004, for the first time, the newly upgraded AURIGA detector and the LIGO interferometers took data simultaneously. This opened the coincidence analysis between the two collaborations, even if the shortness of the coincidence run force us to consider the results of a joint analysis as a playground for future, longer, runs. In July 2004, the spokespersons of the two collaborations signed a Memorandum of Understanding (LIGO-AURIGA MoU (2004)) for the first joint data analysis between the two experiments. A *Joint Working Group* was formed to join the efforts of the two collaborations and to develop a methodology for a coincidence bursts search. The Joint Working Group agreed to implement a wide-band cross-correlation search on the LIGO timeseries triggered by the AURIGA candidate events. Cross-correlation has been applied between the interferometers of Hanford (LHO1 with a 4 Km arm and LHO2 with a 2 Km arm) and Livingston (LLO) in the case of quadruple coincidence network AURIGA-LHO1-LHO2-LLO. The same analysis has been repeated for the triple coincidences AURIGA-LHO1-LHO2. The relevance of the results relies in the test of a methodology for a joint search between non-homogeneous detectors.

1. INTRODUCTION

Chapter 2

Gravitational wave detectors

In this chapter a short introduction of the gravitational waves is given (section 2.1). Purpose of the section is just giving a short derivation of gravitational waves from General Relativity. For a more exhaustive outline of gravitation we remand to Misner, Thorne & Wheeler (1973). Another elementary introduction is given in Chakrabarty (1999).

Since this work has been developed within the AURIGA collaboration, section 2.3 focuses on the main features and problems of this resonant detector in its newly updated setup.

About the interferometric detectors which will be involved in the AURIGA-LIGO analysis (treated in the following chapters), we limit the description to the informations given in section 2.2, where the main principles of operation are discussed.

2.1 Gravitational waves

In analogy to the prediction of electromagnetic waves by the Maxwell equations of electrodynamics, gravitational waves can be derived as a radiative solution of the Einstein field equation under certain approximations.

The Einstein equation, in its general form, is written as:

$$R_{\mu\nu} - \frac{1}{2} g_{\mu\nu} R = \frac{8\pi G}{c^4} T_{\mu\nu} \tag{2.1}$$

where $R_{\mu\nu}$[1] and R are the Ricci tensor and scalar, $g_{\mu\nu}$ is the metric tensor, $T_{\mu\nu}$ is the stress-energy tensor, c is the speed of light and G is the gravitational constant. The Ricci tensor depends on the metric through the equation:

$$R_{\mu\nu} = \partial_\beta \Gamma^\beta_{\mu\nu} - \partial_\nu \Gamma^\beta_{\mu\beta} + \Gamma^\beta_{\nu\mu}\Gamma^\gamma_{\beta\gamma} - \Gamma^\gamma_{\mu\beta}\Gamma^\beta_{\nu\gamma} \tag{2.2}$$

where $\Gamma^\mu_{\alpha\beta}$ are the Christoffel symbols:

$$\Gamma^\mu_{\alpha\beta} = \frac{1}{2} g^{\mu\nu}(\partial_\beta g_{\nu\alpha} + \partial_\alpha g_{\nu\beta} - \partial_\nu g_{\alpha\beta}) \tag{2.3}$$

Equation 2.1 results difficult to solve because of the dependence of the Ricci tensor and scalar on the metric $g_{\mu\nu}$. However, approximations are usually adopted in these cases to find the solutions $g_{\mu\nu}$ of the Einstein fields equations (called "metrics" of space-time).

A first simplification of equation 2.1 is the *weak field approximation*. In absence of gravity, space-time is flat and described by the simple Minkowsky metric $g_{\mu\nu} = \eta_{\mu\nu} = diag(-1, 1, 1, 1)$. Introducing a *weak* gravitational field means introducing a small perturbation on the metric ($|h_{\mu\nu}| \ll 1$):

$$g_{\mu\nu} = \eta_{\mu\nu} + h_{\mu\nu} \tag{2.4}$$

This formalism is known as *"linearized theory of General Relativity"*. Now, it is possible to define the tensor:

$$\phi^\nu_\mu = h^\nu_\mu - \frac{1}{2}\eta^\nu_\mu h \tag{2.5}$$

Since the coordinate system in space-time is not fully specified by equation 2.4 we must fix a gauge, for example:

$$\partial_\nu \phi^\nu_\mu = 0 \tag{2.6}$$

which is often referred to as the *Lorentz gauge* (see Misner, Thorne & Wheeler (1973)). From equation 2.5 and equation 2.6 we get:

$$\partial_\nu (h^\nu_\mu - \frac{1}{2}\eta^\nu_\mu h) = 0 \tag{2.7}$$

[1] as usual, indexes with Greek letters are referring to the 4 space-time components. Repeated indexes imply the sum over all components.

while, from equation 2.2 (neglecting the quadratic terms) we have:

$$R_{\mu\nu} = -\frac{1}{2}\partial_\beta \partial^\beta h_{\mu\nu} \tag{2.8}$$

By introducing equation 2.8 in the general form of Einstein equation 2.1 we get the simpler formula:

$$\Box \phi_{\mu\nu} = -\frac{16\pi G}{c^4} T_{\mu\nu} \tag{2.9}$$

In vacuum, $T_{\mu\nu} = 0$ and

$$\Box \phi_{\mu\nu} = 0 \tag{2.10}$$

The simplest solution of equation 2.10 is the monochromatic plane wave:

$$\phi_{\mu\nu} = A_{\mu\nu} e^{ik_\alpha x^\alpha} \tag{2.11}$$

with frequency $\omega_0^2 = c^2 k_0^2 = c^2(k_1^2 + k_2^2 + k_3^2)$ and propagation speed c. The direction of the wave will be $\hat{k} = \frac{1}{2}(k_1, k_2, k_3)$.

As can be seen from equation 2.11, a gravitational wave must be specified by means of 10 coefficients $A_{\mu\nu}$ (in fact $A_{\mu\nu}$ is a symmetrical matrix).

However, in equation 2.11 there is still a gauge freedom which can be fixed (for example) in this way:

$$A^\mu_\mu = 0 \tag{2.12}$$

$$A_{\mu\nu} U^\beta = 0 \tag{2.13}$$

where U^β is a constant time-like unit vector arbitrarily chosen. Equation 2.12 imposes a null trace for $A_{\mu\nu}$, while equation 2.13 imposes its orthogonality to the wavefront. This gauge is called *transverse-traceless* (TT) gauge. By imposing these conditions, we reduce from 10 to 2 the components describing the gravitational wave.

In other words, it is always possible to choose a gauge (the TT gauge) for which a monochromatic wave in vacuum is described by means of only 2 scalars. Now, if we take the coordinate axes so that our gravitational wave propagate along the z direction, we can write:

$$\mathbf{A}^{\mathbf{TT}} = \begin{pmatrix} 0 & 0 & 0 & 0 \\ 0 & A_{xx} & A_{xy} & 0 \\ 0 & A_{xy} & -A_{xx} & 0 \\ 0 & 0 & 0 & 0 \end{pmatrix} \tag{2.14}$$

If we call $A_{xx} = A_+$ and $A_{xy} = A_\times$ the 2 independent polarizations, matrix 2.14 becomes:

$$\mathbf{A^{TT}} = \begin{pmatrix} 0 & 0 & 0 & 0 \\ 0 & A_+ & A_\times & 0 \\ 0 & A_\times & -A_+ & 0 \\ 0 & 0 & 0 & 0 \end{pmatrix} \tag{2.15}$$

Every gravitational wave can be described as a combination of the $+$ and $\times$ components just defined. As a gravitational wave passes by, massive objects change their length as shown in figure 2.1. A survey of the principles and details of gravitational detection will be given in section 2.2.

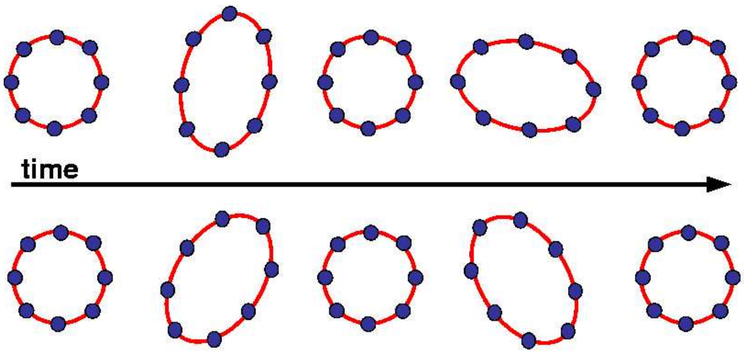

Figure 2.1: Time evolution (from left to right) of the effect of a gravitational wave which propagates perpendicularly to the plane. A circular ring composed by free particles is squeezed and stretched, depending on the phase of the wave, to form an ellipse. The ellipses formed in accord to the two orthogonal polarizations (top and bottom) are rotated by 45 degrees.

In 1993, Joseph H. Taylor Jr. and Russell A. Hulse were awarded with Nobel Prize in Physics "*for the discovery of a new type of pulsar ($PSR1913+16$), a discovery that has opened up new possibilities for the study of gravitation*". With this study they demonstrated that the orbiting period of the pulsar $PSR1913+16$ around its companion gradually diminishes accordingly to an energy loss consistent with the emission of gravitational waves predicted for such a system. In this way an indirect proof of the existence of gravitational waves was given, even if, nowadays, no one succeeded in a direct detection.

2.2 Bars and interferometric detectors

As presented in the previous section, gravitational waves cause tiny variations in the dimensions of objects as the waves pass by. The operating gravitational wave detectors exploit two main methods of detection. The first is the measure of the elastic deformation of a body, close to its resonance frequency, due to the incoming wave. The second is based on the measure of changes in the distance between almost freely moving test particles.

The earliest attempt to measure ripples in the space-time was performed by Joseph Weber in the early 1960s using *resonant bar detectors*. Detectors of this kind are shaped as cylindrical masses of some tons. When a gravitational wave passes and excites the longitudinal mode of the bar, these devices sense a change in the spatial distance between their ends. Nowadays, the operating resonant bar detectors are: AURIGA at LNL, Padova (see the AURIGA web page), NAUTILUS at LNF, Frascati (Astone *et al.* (1997)), EXPLORER at CERN (Astone *et al.* (1993)) and ALLEGRO at Baton Rouge (Mauceli *et al.* (1996)). For the precise sites and orientations of these detectors see Astone *et al.* (2003). A more detailed description of the operating principles for the AURIGA bar is given in section 2.3.

The second class of gravitational wave detectors is constituted by the *interferometric detectors* (or *interferometers*). These kind of technology has been thought to detect ripples in space-time by means of a laser interferometer: through this device it is possible to measure (with a very high precision) the time spent by light to travel between two freely suspended mirrors, hang at the extremes of the two "arms" of the interferometer. The arms have been designed to be perpendicular. Laser light is introduced in the detector splitted in two beams (by means of a beam splitter). Each one travels through one arm, bounces back and forth along it (because of the mirrors) and returns to the beam splitter, where the two beams are recombined. If the arm lengths are exactly the same, the light returning to the beam splitter will fully recombine and return toward the laser. If some disturbances (e.g. a gravitational wave) cause a small relative change in the arms length, light will return to the beam splitter with a phase difference between the beams. In this case there will be a difference interference pattern for the light from the two arms; a part of the combined beam will reach the laser while another portion will spill onto a photodetector. LIGO interferometers operate in keeping the photodetector in the dark: a feedback system keeps the mirrors in their places by means of a force opposite to the one trying to change their positions. This feedback is realized through a system of magnets and currents. The measure of the force needed to feed back the mirrors provides an indirect measure of the force acting on them.

The observation of gravitational waves through interferometers permits (with respect to use resonant detectors) to inquire with a better sensitivity a larger range of frequencies. Actually, several projects for interferometric detectors exist. The French-Italian experiment VIRGO (with arm-length of 3 Km, see the VIRGO web page) is going to approach its design sensitivity. The GEO600 (see the GEO web page) project has an arm-length of 600 m and is located in Hannover, Germany. Another interferometer, TAMA300 (see the TAMA web page), is located in Japan and it is meant to be a prototype for the advanced interferometric detector LCGT, also to be built in Japan. Both GEO600 and TAMA300 have already approached their design sensitivity and taken data in science-mode in this configuration.

Yet, the largest project is LIGO (see the LIGO web page), which includes 3 detectors: one at Livingston (LLO, with arm-length of 4 Km) and two at Hanford: LHO1 with arm-length of 4 Km and LHO2 with arm-length of 2 Km (see figure 2.2). In the last case the same facility hosts 2 different interferometers: the vacuum tubes are the same but the test masses (and the arm-lengths) are different. This causes, necessarily, a correlation in the environmental noise of the 2 devices which cannot be considered as affected by uncorrelated noise. However, the coincidence between the two interferometers LHO1 and LHO2 permits relevant advantages:

1. it helps to reject false alarms due to any non-correlated noise source, such as the intrinsic noises of the detectors;
2. if coincident displacements occur between the two detectors, we can test the signal consistencies since the gravitational wave would produce the same displacements, apart from the scale factor due to the ratio between the arm lengths.

For a detailed description of the sites and orientation of the interferometers see Allen (2004).

The best performances reached by an interferometric detector can be represented by a typical spectrum of the LIGO detectors (the most sensitive operating interferometers). In figure 2.3 the typical noise spectra of LHO1 during the last scientific runs are compared with the design sensitivity for that detector. The present configuration of LHO1 guarantees performances very near to the goal sensitivity.

The best sensitivity reached by a resonant bar detector has been obtained by AURIGA during the present run at 4.5 K (see figure 2.4). The strain noise is better than 10^{-20} Hz$^{-1/2}$ over a sensitivity band of 110 Hz. A strain noise of the order of some 10^{-22} Hz$^{-1/2}$ was obtained by NAUTILUS and AURIGA (in its first run) at $T \approx 0.1$ K, but on a much smaller bandwidth (see figure 2.6, section 2.3).

Regardless of the sensitivity, it is of main importance, for each kind of detector, to associate with other collaborations in order to form a network. The multiple observation, achievable by a network of independent detectors, guarantees an higher confidence the more detectors are contributing. Moreover, with a network of detectors, it is possible to solve (by triangulation) the so-called *"inverse problem"*, i.e. to determine all the informations the wave carries and locate the source in the sky by means of the direction. Several papers formalize a joint observation of a source using a non-homogeneous (i.e. bars and interfermeters) network, e.g. Gursel & Tinto (1989) or Astone *et al.* (1994). This last work

Figure 2.2: On the top: the LIGO (Laser Interferometer Gravitational-wave Observatory) of Hanford, WA. The interferometer is an L-shaped vacuum system which houses 2 co-located detectors (LHO1, 4 Km of arm-lengths and LHO2, 2 Km of arm-lengths) which share the same vacuum system but have different test masses at the extremes. On the bottom: the LIGO facility at Livingston, LA (4 Km of arm-lengths). (Photos: courtesy of the LIGO Laboratory).

refers to time-coincidences and (on the contrary of the approach described in this thesis) addresses the issue of different sensitivity bands by narrowbanding the interferometer.

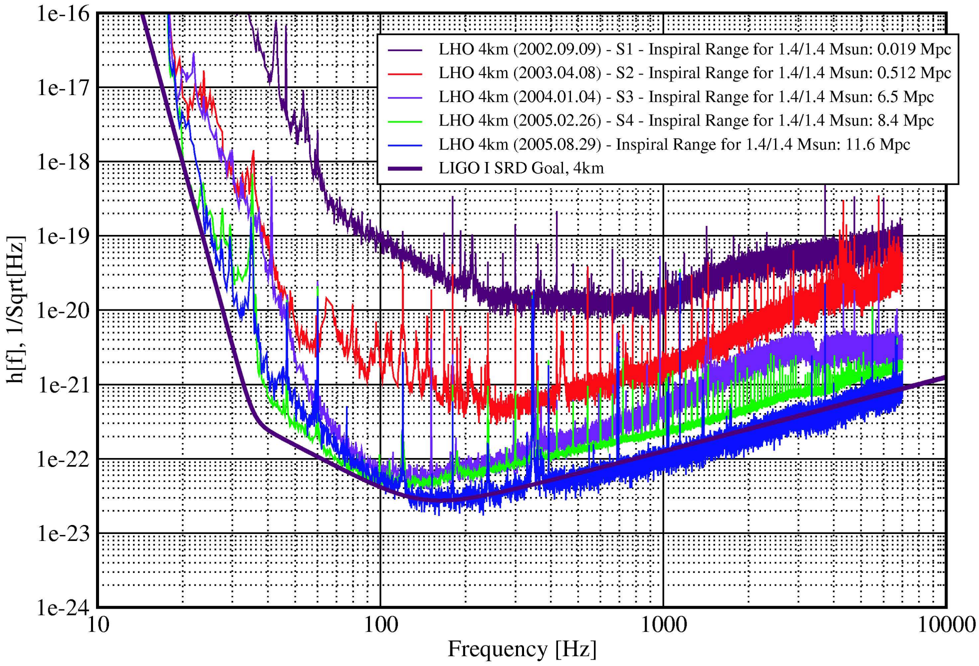

Figure 2.3: Typical strain sensitivity of LHO1 during the past scientific runs: S1 (August 23 - September 9, 2002), S2 (February 14 - April 14, 2003), S3 (October 31, 2003 - January 9, 2004), S4 (February 22 - March 23, 2005). The blue curve refers to the most recent performances and proves that LIGO is approaching its design sensitivity (the solid violet curve). (LIGO document LIGO-G050483-01-Z - courtesy of LIGO laboratory).

In the next chapters we will describe the first data exchange between the observatories LHO1, LHO2, LLO and AURIGA.

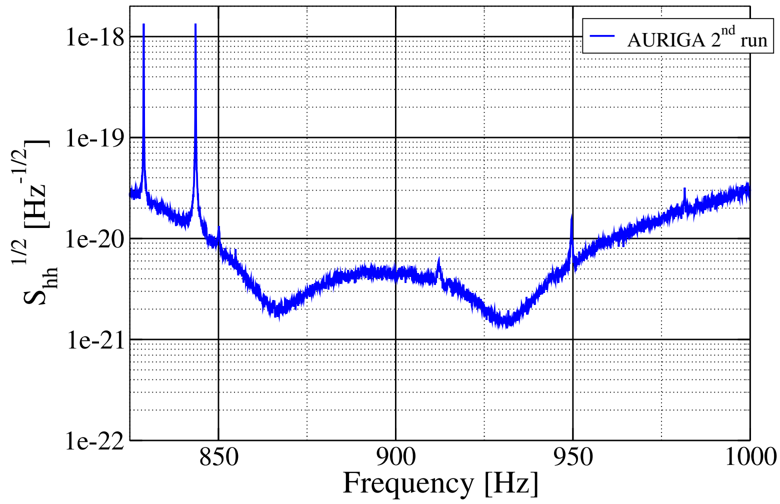

Figure 2.4: One-sided strain noise of the AURIGA detector during summer 2005. In the current setup, a readout upgrade increased the bandwith up to more than 100 Hz. The detector, running at a temperature of 4.5 K reaches a strain noise of the order of 10^{-20} Hz$^{-1/2}$ over all its bandwidth.

2.3 The AURIGA detector

2.3.1 General scheme

The AURIGA[1] detector is one of the 4 operating resonant bar detectors.

A resonant detector of gravitational waves is a system of one or more free moving masses. The physical effect of an incoming gravitational wave, impinging on the detector, is to excite its quadrupolar modes. In particular, in a resonant bar, one looks at the fundamental longitudinal mode. This can be modeled by a system of free falling particles (of masses $m/2$, where m is the mass of the bar) coupled by a spring. A gravitational wave with amplitude h modifies the relative distance l of the 2 masses by an amount $\delta l = h\, l$.

The natural frequency of oscillation depends on the mass and the material of the mechanical resonator. The body of AURIGA is a 3 m-long cylinder with a diameter of 60 cm and it is made of aluminum enriched in magnesium ($Al5056$). The mass of the bar results about 2.3 tons and the resonant frequency of its first

[1]AURIGA is a project financed by INFN (Istituto Nazionale di Fisica Nucleare).

longitudinal mode is around 1 KHz. The exact value of this frequency depends on the temperature: at room temperature it is about 874 Hz, at 100 mK it is about 920 Hz. This makes of gravitational wave bursts around 1 KHz (see section 3.1) the best candidates for detection.

In a resonant detector, the main, unavoidable, source of noise is constituted by the thermal noise of the mechanical resonator. Thermal noise is due to thermal motion of the atoms inner to the bar which causes a vibration of the bar itself. This kind of disturbance can be carefully modeled by considering the detector as affected by a stochastic force noise which spectral density is given by the fluctuation-dissipation theorem (Nyquist (1928)):

$$S_F(\omega) = 4\frac{\omega}{Q} m K_B T \tag{2.16}$$

where T is the temperature, m is the mass of the oscillator, K_B is the Boltzmann constant and Q represents the mechanical quality factor. Hence, in order to minimize thermal noise, one must keep temperature as low as possible and use materials with an high Q-factor. AURIGA belongs to the class of ultracryogenic detectors because it can reach temperatures around 100 mK. The quality factor is 4×10^6.

To measure the displacement of the bar resonator, the mechanical signal from the bar must be converted in an electric signal which will be read by a low noise amplifier. A scheme of the AURIGA transducer and readout is given by figure 2.5.

The conversion of the signal from mechanical to electromagnetic is performed by a resonant capacitive transducer (Crivelli-Visconti *et al.* (2000)). The transducer is a "mushroom" shaped oscillator which frequency is tuned to the resonance frequency of the bar. Because of its lighter mass (of the order of Kg), the transducer produces a mechanical amplification of the signal proportional to the square root of the masses ratio. In this way, bar and transducer can be modelled as a system of two coupled harmonic oscillators which resonate at the two frequencies of their mechanical normal modes. These modes correspond to the minima of the curves in figure 2.6. The "mushroom" resonator constitutes one

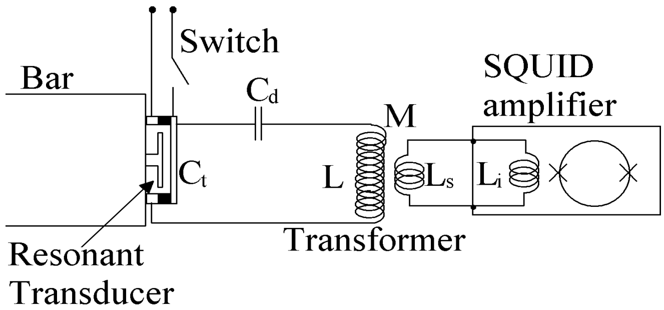

Figure 2.5: The readout chain of the AURIGA detector. On the left, the bar is directly attached to a plate of a resonant capacitive transducer. The other plate works as a resonator which induces a modulation on the transducer capacitance C_t. This capacitance is kept constant thanks to a decoupling capacitor (C_d). Then, before being amplified by a SQUID amplifier, the electrical signal passes through a matching transformer. This optimizes the signal transfer from the transducer to the SQUID.

the plates of a capacitor C_t. The second plate is rigidly attached to the bar. The capacitor is biased with a DC electric field, kept by means of a decoupling capacitor C_d (see figure 2.5). In this way, the motion of the bar results in a modulation of the transducer capacitance, and hence in an electrical output signal.

The final step in the detection chain is the readout of the electrical signal, which is performed by a low noise dc SQUID (Superconducting Quantum Interference Device)[1], the most sensitive amplifier available in the kHz frequency range. A matching transformer is interposed in order to optimize the signal transfer from the transducer to the SQUID.

All the components of the transducer chain introduce additional noise components. In particular, both transducer and electrical circuit contain dissipating elements and introduce thermal noise accordingly to equation 2.16. The SQUID noise consists of 2 distinct components: an additive current noise with noise spectral density S_i, which superimposes on the input signal, and a back action voltage noise (S_v) which acts as a real disturbance on the input circuit. A useful figure of merit to characterize the SQUID noise is the noise temperature

[1]The dc SQUID is a superconducting device, based on the Josephson effect, which can measure very small magnetic fields.

$T_n = (S_v S_i)^{-1/2}/K_B$. It has been demonstrated that $K_B T_n$ represents a lower limit on the energy sensitivity of the detector (Giffard (1976), Price (1987)).

Thermal noise and electronic noise of the amplifier are *internal* noises because they are directly related to the apparatus. Besides this class of noise (which can be carefully modeled), a second class of noise limits the detection capability of the experimental apparatus. It is the *external* noise: mechanical and acoustic noise belong to this class because related to human activity and environmental noise in the laboratory. These kind of disturbances introduce non-Gaussianity in the data and (typically) they are very difficult to control because non-modelable.

The principal way to control external noises is to suppress them by means of a careful isolation system. This is reached by the AURIGA detector through two vacuum chambers (which isolate the bar from the acoustic noise) and through a damping system (which isolates from the mechanical noise). The damping of low frequencies is reach by placing the AURIGA detector on a sand layer which damps up to 20 dB of the mechanical low-frequency vibrations of the floor. A second stage of isolation is reached by means of the system of damped harmonic oscillators (which will be described in next section 2.3.2) and which suppress noise in the kHz range of frequency. Another strategy to suppress external noises is implement an anti-coincidence veto on some known environmental noises (such as the anti-coincidence with seismometers).

2.3.2 Setup for the second run

To improve the performances and overcome some problems met during the first run (1997-1999), the AURIGA detector was forced to stop and undertake a 4 years period of R&D. The upgrade of the detector regarded: the suspension system (Bignotto *et al.* (2005), Zendri *et al.* (2003)), the cryogenics (Zendri *et al.* (2002)), the readout (Baggio *et al.* (2005)), the data acquisition and data analysis (Cesaracciu *et al.* (2003)).

The AURIGA suspension system has been completely redesigned with respect to its first run (see figure 2.7). Now, the filtering of environmental noise is reached through "spring-mass" elements capable to guarantee an attenuation of about 40 dB each one at 1 kHz, (see Bignotto *et al.* (2005) and Zendri *et al.* (2003)). The "spring-mass" are combined in a cascade of 6 elements to form the body of 4 columns, for a total attenuation of 240 dB. The new suspension system is free from internal resonances in the range of frequencies 700-1200 Hz. A further attenuation of the environmental noise has been reached by changing the bar hanging method. Instead of the old cable around the bar middle section, now AURIGA hangs from its barycenter through a rod. This should limit the coupling between the bar longitudinal mode and the suspension motion (Zendri *et al.* (2002)).

At present, the detector operates at a temperature of about 4.5 K, while cooling down at ultracryogenic temperature ($\approx$ 0.1 K) is scheduled for 2007. This final cooling will be achieved by means of a diluition refrigerator, not yet integrated in the cryostat, which exploits the phase migration of ^3He towards ^4He to absorb heat.

The most significant improvement in the passing from the first to the second run has been a drastic enlargement of the AURIGA sensitive band (see figure 2.6) as a consequence of the new readout system. The basic scheme is the classical capacitive transducer shown in figure 2.5. The main new feature is the tuning of a third electrical mode, constituted by the LC resonance of the electrical readout circuit, to the frequency of the mechanical modes (see Baggio *et al.* (2005) and Zendri *et al.* (2002)). This procedure improves the signal transfer from the bar to the amplifier and allows to obtain a significant increase of the bandwidth, provided that the quality factor of the electrical mode is at least of the order of the mechanical quality factor. This condition has substantially been achieved (Baggio *et al.* (2005)). The electrical bias field is about $7 \cdot 10^6$ V/m and is similar to the one obtained in the first run. However, there are prospects to improve this value by at least a factor 2.5 in the next ultracryogenic run. Besides the transducer improvements, a low noise two-stage SQUID amplifier has been implemented (see Vinante *et al.* (2001) and Vinante *et al.* (2002)). The noise temperature is of the order of $600\hbar$ at $T = 4.5$ K, to compare with the $4000\hbar$ of the first run. It has been shown that the noise of this device scales with temperature down to

0.2 K (Mezzena *et al.* (2001)), so that a large noise reduction is expected at ultracryogenic temperature. As a consequence of the readout improvements, a sensitivity $S_{hh}^{1/2}$ better than 10^{-20} Hz$^{-1/2}$ over a bandwidth of 110 Hz has been achieved (Vinante (2006)).

Side by side to the hardware upgrades, the AURIGA data acquisition and data analysis pipelines have been redesigned. In particular, the data acquisition system (DAQ) and the AURIGA data analysis (`ada`) have been rewritten using an "object oriented" language and exploiting several "open source" libraries. For technical details on the data acquisition see Cesaracciu *et al.* (2003). A description of the `ada` analysis pipeline will be given in section 5.2.1.

On December 2003, the AURIGA detector started a period of data taking (at a temperature of 4.5 K) for purpose of diagnostic and calibration. During this period, even if affected by spurious non-modeled lines, the antenna achieved a sensitivity very closed to the predicted one. Data used for the AURIGA-LIGO joint analysis have been acquired during this period.

The effect of environmental noises (and related nonlinear phenomena producing spurious lines in band) significantly decreased in spring 2005 when the inner suspensions system of figure 2.7 has been enriched with external suspensions (see figure 2.8) which guaranteed a good mechanical isolation at low frequency. These seismic isolations consist of active-air mounts, welded to the cryostat while keeping liquid helium in. The result achieved is a very stable behavior (duty cycle of $\sim 98\%$) and a good gaussianity of data (Taffarello (2005)).

Up to now, AURIGA operated at cryogenic temperatures ($1.5-4.2$ K) because this setup guarantees the longer duty cycle. A cool down to ultra-cryogenic temperature ($50-100$ mK) is planned for the year 2007 and will be reached with the use of a diluition refrigerator. Noise predictions of the future performances are given in figure 2.6 where the effect of the cool down to 100 mK (green curve) is shown together with the effect of increasing the transducer field by a factor 2.5 (magenta curve).

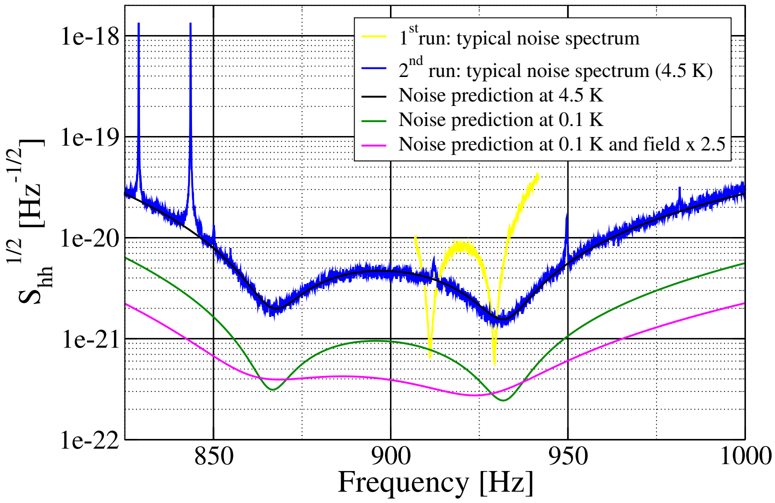

Figure 2.6: One-sided noise spectra featured by the AURIGA detector during its first run (in yellow) and its second run (in blue). More informations on the spurious lines featured in the second run will be given in section 5.2. Noise theoretical predictions are also indicated for the 4.5 K setup (in black), the ultracryogenic setup (in dark green) and in case of ultracryogenic setup with transducer bias field increased by a factor 2.5 (in magenta). The agreement between the current sensitivity and the expected one is remarkable.

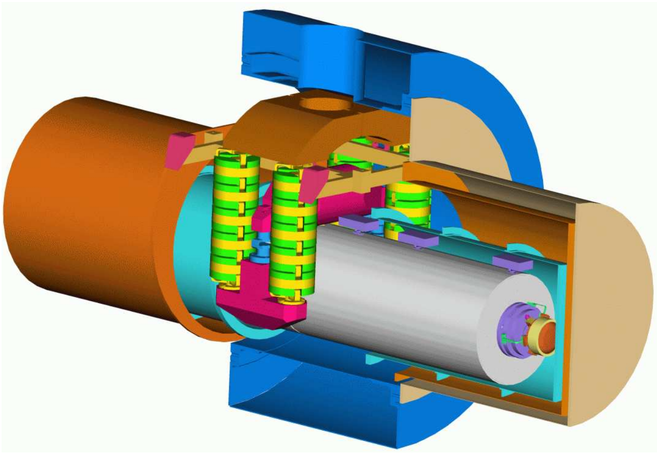

Figure 2.7: In this figure the inner suspensions of AURIGA are shown inside the liquid Helium vessel (in blue). A system of 4 columns consisting of 6 aluminum springs (in yellow) loaded by bronze masses (in green) supports a structure (in magenta) where a rod is fixed to support the bar (in gray) from its center of mass. The rod (which is not visible in this picture) has also the aim of providing thermal link between the bar and the refrigerator. At the visible extremity of the bar, the transducer and the SQUID readout system.

Figure 2.8: Photograph of the external suspensions of AURIGA: these active-air mounts consent a good damping of the environmental oscillations above 2 Hz. Thanks to this damping system (set up on spring 2005) AURIGA achieved a very good duty cycle and improved the Gaussianity of data.

Chapter 3

Science goals and overview of gravitational wave bursts searches

As anticipated in the previous chapters, the target signals for the first AURIGA-LIGO joint search are gravitational waves bursts. In this chapter, an overview of the possible sources for this kind of signal is given in section 3.1.

Gravitational wave bursts are one of the most targeted by network analyses, since this kind of search has been extensively treated in literature. Section 3.2 gives an overview of the works which inspired the analysis described in next chapters. Works analyzed here are all devoted to a search using networks of detectors. In fact, as stressed in section 2.2, only a multiple observation could be a reliable detection and could resolve direction and polarization of the signal.

The methodologies for bursts search studied within the AURIGA-LIGO Joint Working Group are presented in section 3.3, where an outline of the performances of the network, during the coincidence run, is also introduced. A more detailed description of the methodology applied in the final analysis will be given in chapters 5 and 6.

3.1 Sources

The kind of network analysis greatly affects the detection efficiency to different sources. In the AURIGA-LIGO network we choose to target signals with short duration (≤ 20 ms) in the AURIGA sensitivity band. The most suitable sources for these signals are black holes ring-downs, mergers of coalescing neutron stars (NSs) or black holes (BHs) binary systems.

In literature, it is well known that coalescence of compact objects constitutes an interesting source of high-frequency gravitational waves (Thorne (1987)). Among them, the coalescence of NS-NS, NS-BH, BH-BH binary systems are expected to emit gravitational radiation in the kHz range (Thorne (1995)). Binary black hole systems are the most massive and, as a consequence, the most promising sources. During the coalescence, the following phases of emission can be distinguished: the *inspiral phase*, the *merger phase* and the *ringdown*.

In the *inspiral phase* two distinct bodies spiral towards one another, losing energy and angular momentum (Thorne (1987)). During this phase the waveform increases its amplitude and sweeps upward in frequency (forming the so called "chirp" waveform). The rate of frequency sweeping (df/dt) depends on the masses involved. In the case of circular orbit, it is proportional to the ratio $(M_1 M_2)^{3/5}/(M_1 + M_2)^{1/5}$. The mass of a neutron star is less than $1.4 M_{\odot}$, that of a BH reaches some tens of $M_{\odot}$. Binary pulsars (such as the Hulse-Taylor binary, see Taylor (1994)) emit roughly at 10^{-4} Hz but, in their final coalescence stage, they are expected first to reach the ground-based interferometer range of frequencies and then (in few minutes) the resonant detectors' band ($\sim 10^3$ Hz). For such a kind of sources, the internal, nonspherical kinetic energy as been estimated (Thorne (1995)) to be of the order of a solar mass, and the amplitude h of the emitted gravitational waves is evaluated as $h \sim 10^{-21}$ at 200 Mpc (the best-guessed distance to have few NS-NS binaries per year). Even if this kind of signal could (in principle) be detected both by interferometers and resonant detectors, the chirp signals are not the target of the joint analysis which this thesis is devoted to. Instead, the subsequent stages of the coalescence are of primary interest because expected to emit gravitational wave bursts. The inspiral of a binary BH system is not so fully understand as the inspiral of binary NS systems. Some works (such for example Abbott *et al.* (2005a)) performed the search using the implementation of specific phenomenological templates. Abbott *et al.* (2005a) also set an upper limit on this kind of sources using data from the LIGO scientific run S2.

The inspiral phase ends in a freely falling plunge when a dynamical instability is encountered by the bodies. The collision between the inspiralling objects, which should be quick, constitutes the *merger phase*, and is expected to emit gravitational waves (Cutler *et al.* (1993)). Even if the signals waveforms during this phase are not known, their duration is supposed to be about some milliseconds and the signal can be considered as a burst. Several scenarios exist to model this kind of emission (Baker *et al.* (2002)). Thorne (1995) indicates 800-2500 Hz as the possible range of gravitational wave emission in a NS/NS merger. A kHz range is expected also for the system NS-BH. Flanagan & Hughes (1998) explored the possibility of detection of a binary black hole system (at ~ 200 Mpc) during the merger phase through ground-based interferometers and estimated the possible SNR as few tens (in a range of masses of few $M_{\odot} - 2000 M_{\odot}$). A numerical simulation of the signal waveform from merger and ringdown is given by Baker *et al.* (2002). According to Baker *et al.* (2002) the gravitational radiation during the merger of a binary system with masses of some tens of $M_{\odot}$ would have an high energy content around 1 kHz, so it should be detectable also by AURIGA. At the end of this phase, the waveform is expected to slowly resemble that of the ringdown phase.

The final stage of the binary system evolution is represented by the *ringdown* of the merged black hole. During this phase the system settles down through a series of oscillations (quasinormal modes) whose signal waveform can be thought as an exponentially damped sinusoid (Flanagan & Hughes (1998)).

Another important source of gravitational wave signals is constituted by the collapse of a massive star in a neutron star or a black hole. This happens when the star exhausts its nuclear fuel. Sometimes, the collapse causes a subsequent explosion of the star's mantle and we have a supernova explosion. The collapse can give rise to several possible evolutions, with subsequent emission of gravitational waves. Thorne (1995) provided a short review of different scenarios with an emission of gravitational waves in the range few hundreds-1000 Hz. The LIGO full-band sensitivity to supernovae has been evaluated to be of the order of $\sim$ 1 kpc or less for the Zwerger-Muller sources (Zwerger & Muller (1997)) and Dimmelmeier-Font-Muller sources (Dimmelmeier, Font & Muller (2002)). A larger distance has been evaluated for the Ott-Burrows-Levine-Walder waveforms (Ott *et al.* (2004))

The joint working group decided to test the efficiency of the AURIGA-LIGO network on three waveforms: a damped sinusoid waveform (motivated by the ring-down phase) and simpler pulses waveforms as a Gaussian pulse and sinusoidal oscillations with a Gaussian envelope of the amplitude (see section 6.2 and appendix B). These last class of signals has not an astrophysical meaning but, since they are very simple linear polarized waveforms, Gaussians and sine-Gaussians are very useful for reference and tuning of the analysis algorithms.

3.2 Overview of gravitational wave bursts searches

Before the first AURIGA-LIGO joint analysis, both the LIGO and the AURIGA collaborations have taken part to previous burst searches which produced upper limits. In the following, I report on the works which inspired the methodologies and the considerations proposed for the first AURIGA-LIGO burst search.

Astone *et al.* (2003) present final results for the first burst search within the International Gravitational Event Collaboration (IGEC). This analysis, which covers a 4-year observation time, involved the greatest number of detectors ever combined in a worldwide network. In fact, all the existing bars (all nearly co-aligned) were considered to form networks of two or more detectors in simultaneous observation. Target of the search were δ-like gravitational wave bursts with frequency $\sim$ 1 kHz and a duration of $\sim$ 1 ms.

Each bar detector is searched by the responsible group for δ-like signals with an adaptive amplitude threshold at a fixed SNR (ranging from 3 to 5 in amplitude). The information exchanged within IGEC include the candidate event lists (with arrival time and estimated amplitude) and the value of detector absolute threshold during time. The amplitudes are given in terms of the Fourier component (units 1/Hz):

$$H_0 = \frac{1}{4L\nu_0^2}\sqrt{\frac{E_s}{M}} \tag{3.1}$$

where L, M, ν_0 and E_s are (respectively) the length, the mass, the mean resonant frequency and the energy released in each bar.

The network analysis is based on a data selection and a time coincidence search as a function of the amplitude of the target signal. In particular, the detector threshold information is used to determine, from time to time, which configuration of detectors is more efficient for a target signal amplitude and direction. Then, the time coincidence is required only within the more suitable configurations, and exploits the informations on the arrival time uncertainties to keep under control the false dismissal. The methodology provided an accurate estimation of the statistics of accidental coincidences obtained by repeating the whole analysis procedure on a set of time-shifted lists (from 10^3 to 10^6 shifts). The first crucial result has been an extremely low false alarm rate for three-fold and four-fold accidental coincidences, less than $1/10^4$ per year. The final result consisted in an upper limit for the rate of short bursts as low as few per year.

From LIGO side, the first search of gravitational waves bursts (see LSC (2004)) regarded the analysis of its first scientific run, S1 (August 23 - September 9, 2002). This was the first chance to test the two event trigger generators `SLOPE` and `TFCLUSTER`, thought to cover a broad range of possible waveforms. Targets of the search were short unmodeled bursts ($4-100$ ms) in the LIGO sensitivity band ($150-3000$ Hz). The only hypothesis on the signal amplitude was to be sufficiently high to be observed over all the detectors noises. For this first burst search, only the configuration of triple coincidence LHO1-LHO2-LLO was considered as a network. Part of the observation time in 3-fold coincidence (about 10%) was used as a "playground" data set, to optimize the data processing pipeline and its parameters. After this procedure, the analysis pipeline was frozen and applied to the full set (which covered the remaining period, about 35.5 h). The strategy for estimating the accidental coincidences for this analysis was the same we will apply in the AURIGA-LIGO burst search: the population of time-shifted coincident burst events (which should be Poisson distributed) has been studied to look for statistically significant excesses in the not-shifted data set. The "off-source" data sets were formed, in this first LIGO analysis, by 24 time shifted data sets. The analysis method consisted in the search of coincident trigger triplets in the network LHO1-LHO2-LLO, which occurred within an interval consistent with the light travel time between the sites and the uncertainties due to the used event trigger generator (ETG). The sets of candidate events were separately produced in each detector using the same ETG. For this analysis, two ETG have been used: `SLOPE` (used to detect, in the time domain, a large time derivative in the data stream, see Pradier *et al.* (2001)) and `TFCLUSTER` (which searches clusters of excess power in time-frequency spectrograms, see Sylvestre (2002)). The parameters which characterize these two techniques can be fixed in part without reference to the data and in part using the playground. The tuning has been performed in order to expect about 1 accidental coincidence in the remaining full data set. However, the playground resulted to be not representative of the data set because of a series of additional effects appeared in the full data set. As a consequence, both event trigger generators resulted non optimally tuned respect to the data and the not shifted data set showed more than 1 coincidence event. Since the "off-source" data sets showed an high variability, `SLOPE` has not been used to produce the final events rate because of limits due to its non-adaptive thresholding. The upper limit rate obtained by this analysis was of 1.6 events per day with a 90% confidence level. This upper limit rate is higher respect to IGEC results because, in this first LIGO-only analysis, the observation time was only 35.5 h. The efficiency of the method has been tested through sinusoidal calibration excitations injected in the data, as will be done in the AURIGA-LIGO analysis (see section 6.2).

The previous search method was repeated by the LIGO collaboration on the second scientific run S2 (February 14 - April 14, 2003) with some changes (LSC (2005)). The goal of the analysis was, once again, to determine an upper limit on the rate of gravitational wave bursts (without assumptions on the waveform) using the network LHO1-LHO2-LLO. Candidates signals for this analysis were all the short signals ($\ll 1$ s) with enough signal strength in the band 100-1100 Hz. As in LSC (2004), thresholds have been tuned to predict less than 1 event over the course of the full run (~ 10 days). However, with respect to the S1 analysis, a different ETG (`WaveBurst`) has been introduced, which consents the r-statistic test (a time-domain cross-correlation test, which checks the consistency between the output of the detectors, see appendix A.1.1). In particular, rather than analyzing separately each single data stream and combine the triggers lists to form coincidences, `WaveBurst` analyzes simultaneously pairs of detectors and finds clusters of excess power after decomposing the signal in the wavelet domain. For each pair, it identifies and writes a list of the transients with consistent features in both the timeseries. The three lists formed analyzing the possible pairs are then compared, in order to check consistency and form a final triple coincidence list. Finally, a waveform consistency test, based on the r-statistic (see appendix A) was performed on this list. The rate of accidental coincidences has been studied, once again, in a set of un-physical time shifted data. An upper limit of 0.26 events per day was set on this data with a confidence level of 90%. The interpretation of the results and the efficiency of the method have been studied using the same classes of injected signal used in S1.

Same data used by LIGO on LSC (2005) were exchanged with the TAMA interferometer for the first upper limit between the LIGO and TAMA observatories (Abbott *et al.* (2005b)). This analysis targeted unmodeled, millisecond-duration gravitational wave bursts.

This heterogeneous network faced new problems with respect to the LIGO-only analysis, in particular different noise spectra and orientations. Abbott *et al.* (2005b) showed that the LIGO and TAMA interferometers have maximum sensitivity to different portions of the sky. This issue was addressed for the first time because both the IGEC and the LIGO-only analysis involved co-aligned detectors. The LIGO-TAMA collaboration issued the problem by neglecting the effect of the antenna pattern during the analysis (the least sensitive detector determined the overall sensitivity of the network) and re-introducing the matter in the study of efficiency (performed using signal injections). To cope with the different noise spectra, the analysis was limited to the search in the range 700-2000 Hz (where all the interferometers featured comparable sensitivity).

For all other aspects, the analysis is similar to LSC (2004) and LSC (2005)): both LIGO and TAMA collaborations produced a list of candidate events to be inquired for coincidences. This was done by LIGO using the `TFCLUSTER` ETG, while TAMA used an excess power algorithm such that used in Ando *et al.* (2005). The rate of accidental coincidences have been studied, once again, in a set of shifted time series. The same consistency test used in LSC (2005) has been performed but only on LIGO data, since it is not clear what one expects from the r-statistic when detectors have different orientations. The "off-source" data sets, after tuning, predict a rate of accidental coincidences of less than 0.1 events over the entire observation time. No events were observed in the "on-source" data set. An upper limit of 0.12 events per day was set at 90% of confidence.

3.3 Methodologies for the first AURIGA-LIGO joint analysis

The most important benefit of a multi-detector data analysis, compared to a single detector analysis, is the provision of a procedure to estimate the statistics of the false alarms occurring by chance (i.e. "switching off" the sources of gravitational waves). In all network burst searches (see previous section) this has been accomplished by investigating the accidental coincidences occurring on time-shifted data sets: the data analysis is repeated many times adding different offsets to the time coordinate of one or more detectors. The time offsets are chosen larger than the light travel time between detectors plus the expected signal duration and the timing uncertainty of the detectors, so to cancel the effects of any coincident gravitational wave present in the data. To ensure independent repetitions of the "off source" experiment, the different time offsets are separated by a length greater than the autocorrelation length of the network coincidences. This method has proven to work well in predicting the statistics of accidental coincidences with a network of independent detectors (such for example in Astone *et al.* (2003)), so that it has been applied also in the AURIGA-LIGO analysis with the caveat of not shifting the two Hanford detectors with respect to one another, since they show some noise correlation.

In Baggio *et al.* (2004), two different approaches have been proposed for the joint analysis, both focused on the search of gravitational wave bursts through an exchange of triggers: a directional method (*method 1*) (to be repeated for several directions in order to map the sky) and a non-directional method (*method 2*) (thought to be an "all-sky" search). The choice of bursts as a target signal has been dictated by the requirement to maximize the potential of the network. This can be achieved only focusing on waveforms seen with more or less the same sensitivity in all the detectors. In other words, we need a signal with a detectable component in the frequency range 800-1000 Hz (the sensitivity band of AURIGA), like signals described in section 3.1.

The so-called *method 1* consists in a time coincidence directional search on the guidelines of the IGEC analysis (Astone *et al.* (2003)). Accordingly to this strategy a list of candidate events (triggers) would be produced by the collaborations involved. This method requires the use of homogeneous estimates of signal arrival times and amplitudes, despite the different spectral sensitivities of the detectors (Cadonati *et al.* (2005)). In fact, we are constrained to a template-less search[1] because of the current uncertainties in the waveform of the target signal. We are still investigating on this issue. One approach, which we are currently testing, is computing the time and amplitude estimators for a common reduced bandwidth (see LIGO Parameter Estimation web page). In this way we sacrifice the most sensitive zone of LIGOs' spectra (i.e. the lower frequencies). Another approach is to exploit some more priors on the waveform, of course loosing some generality. We impose some constraints on the shape of the signal so that LIGO can make the estimates in all its sensitivity band, while AURIGA aims at the narrow-band components at high frequency.

[1]A template search exploits the information of a specific signal shape to optimize its detection efficiency; therefore a good efficiency to different kinds of signals is not assured. A template-less search, instead, uses much weaker assumptions on the signal waveform (e.g. duration) and aims to achieve good performances on a much wider class of signals.

An additional difficulty which must be solved (and was not present in the first IGEC analysis) comes from the signal polarization. In fact the detectors show different sensitivity to the same polarization. This issue can be solved by repeating the search for each direction, with all possible signal polarizations (see section 4).

Method 2 consists in an "all-sky" triggered search (see Cadonati *et al.* (2005) and Poggi *et al.* (2006)). By "all-sky" we mean that the procedure is not optimized for a particular sky direction but, instead, it is tuned to a population of sources uniformly distributed in the sky and with random polarization angles. Of course, this is motivated by lack of knowledge on the signal waveform, polarization and direction. This kind of analysis has been developed on the guidelines of previous LIGO analysis (such as LSC (2004) and LSC (2005)). AURIGA provides a list of candidate events obtained by the usual δ-matched filter. These events work as triggers for a search of excesses of coherent power between the LIGO interferometers in the full bandwidth of the detectors. This search is performed (as usual for the LIGO collaboration) using *CorrPower* (see appendix A.1) a MatLab code which implement a cross-correlation algorithm between the three data stream of the LIGO observatories (Cadonati & Marka (2005)). Once implemented, the detection efficiency of method 2 is estimated using Monte Carlo simulations, by simulating the effects of a set of uniformly distributed sources (with random polarization angles) on all the detectors. Using these injected signals it is possible to evaluate the efficiency of our search method. A more detailed description of this method and the results it returns will be given in chapters 5 and 6.

The Joint Working Group decided to give priority to method 2 which, in fact, has been implemented first. The collaboration agreed on the intention of interpreting the results of this first joint analysis as a methodological study to be considered as a guideline for future, longer runs. For this reason, any excess of candidate events, with respect to the expected accidentals, will be first investigated as a possible hint of problems in the analysis procedure (namely in the estimation of the accidental coincidences) or as the presence of unknown correlated noise.

3.3.1 Performances of the detectors during the coincidence run

With respect to the previous scientific run S2, the upgrade of the LIGO detectors can be summarized as a significant reduction of correlated noise between the collocated LHO1 and LHO2 and a general better sensitivity achieved (see figure 2.3). The main problems of the three detectors during the coincidence run were: transient glitches (for the LHO1 detector) and low duty cycle (30%) for LLO. Moreover, during the course of the run, the noise spectrum of LLO, in the frequency range of AURIGA bandwidth, fluctuated by up to a factor 3. For the Hanford observatories the duty cycles were: 77% for LHO1 and 66% for LHO2. The period of total triple coincidence during S3 reaches 23%.

As extensively explained in section 2.3, during its second run the AURIGA spectrum featured a lower sensitivity (on the dips) respect to its first run (1997-1999) while the band was significantly enlarged (close to 100 Hz) (see figure 2.6). Unfortunately, the AURIGA-LIGO coincidence run took place in the first phase of the AURIGA data taking (December 2003 - January 2004, before setting up the new external suspensions system) when the spectrum was still affected by several, not fully understand, classes of noise lines. One of them produced 4 spurious lines in band (see figure 3.1). The spurious peaks in the AURIGA band during the coincidence run were not stationary, showing day-night variations related to the human activities in the lab and nearby facilities. Usually they stand over the modeled noise by one order of magnitude, and temporarily disappeared for periods of about few minutes. In order to cope with the presence of these spurious lines, AURIGA data analysis has been modified through an adaptive algorithm capable to track their variation in amplitude and to whiten them. A Butterworth notch-filter was used when this was not possible because of rapid variability of the lines.

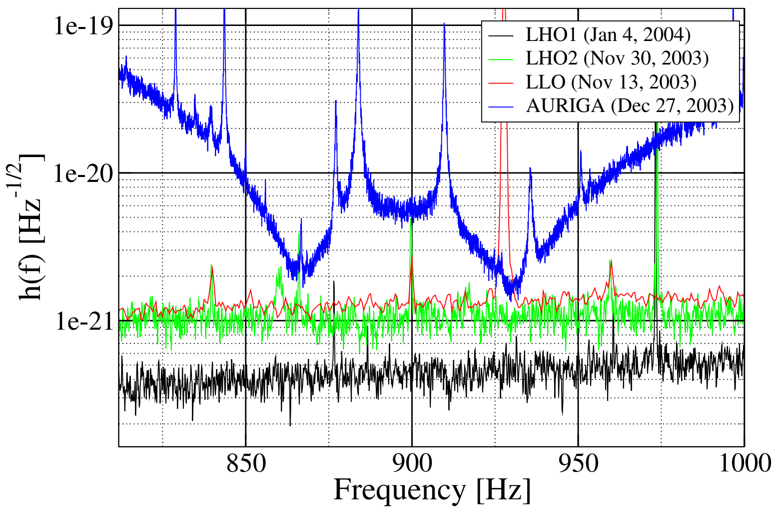

Figure 3.1: Best single-sided sensitivity spectra for AURIGA (blue curve) and the three LIGO interferometers during their first coincidence run, around the sensitivity band of AURIGA ($\sim 800 - 1000$ Hz). For LIGO (black, green and red curves), these are typical spectra during the scientific run S3 while it needs to be remarked that, during the coincidence run, LLO spectra was about 2-3 times worse than in this picture. AURIGA spectrum is affected by some spurious lines at 866.5, 877, 884, 909.5 and 935.5 Hz. In LIGO spectra the calibration lines arevisible (973 Hz for the Hanford detectors and 927 Hz for Livingston). Both the spurious and the calibration lines must be filtered by the analysis. (Figure from Cadonati *et al.* (2005)).

Figure 3.1 shows the four spectra of the detectors involved in the network. In order to make a more direct comparison between the performances of each detector during the coincidence run, it is useful to compare the response to the same waveform, injected in each detector with the same signal-to-noise ratio. For this purpose, let us consider a sine-Gaussian waveform (see also appendix B):

$$h(t) = h_0 \sin\left[2\pi f_0 (t - t_0)\right] \cdot e^{-\frac{(t-t_0)^2}{\tau^2}}\,, \tag{3.2}$$

where the central frequency has been fixed to $f_0 = 900$ Hz (in order to be fully included in the band of interest) and $\tau = 2/f_0$, corresponding to a quality factor $Q = 8.9$. Now we impose to detect its with the same signal-to-noise ratio $\rho = 1$, accordingly to the definition[1]:

$$\rho = \sqrt{4 \int_0^\infty df \, \frac{\left|\tilde{h}(f)\right|^2}{S(f)}} \tag{3.3}$$

where $\tilde{h}(f)$ is the Fourier transform of $h(t)$ and $S(f)$ is the single-sided power spectral density of the noise, (Flanagan & Hughes (1998)). By definition, h_{rss} is the square root of the total burst energy:

$$h_{rss} = \sqrt{\int_{-\infty}^{\infty} dt \, |h(t)|^2} = \sqrt{2 \int_0^\infty df \left|\tilde{h}(f)\right|^2} \tag{3.4}$$

In figure 3.2 the minimum detectable amplitude h_{rss} required to have signal-to-noise ratio $\rho = 1$ (for the test waveform in equation 3.2) is shown as a function of time. In this way it is possible to evaluate, for all the detectors in the network, the actual live time of a measurement at a given threshold, and the stationarity over the observed period.

From figures 3.1 and 3.2 the AURIGA detector might seem not to be of great advantage in the global sensitivity of the network. In particular, from figure 3.2 we can roughly estimate the sensitivity of AURIGA to be 1/3 of the sensitivity of LLO (the least sensitive, at these frequencies, between LIGO detectors) and of the LIGO network as a whole. Despite the sensitivity considerations, the addition of a fourth detector to the observatories of Hanford and Livingston improves

[1] This is the signal-to-noise ratio related to an optimal linear filter matched to the signal.

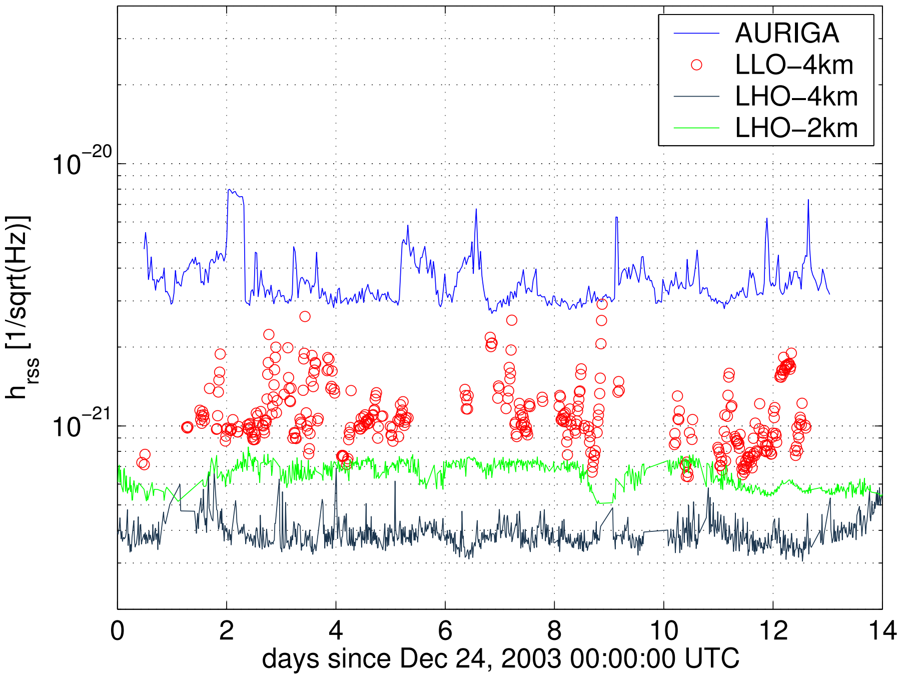

Figure 3.2: Comparison between h_{rss} (see equation (3.4)) of a 900 Hz Sine-Gaussian (characterized by $Q = 8.9$ and $\rho = 1$, see equation 3.3) as seen by AURIGA (blue line) and the three LIGO interferometers (respectively LHO1 in black, LHO2 in green and LLO in red circles) during the coincidence run. (Figure from Cadonati *et al.* (2005)).

the analysis from several points of view. First of, all it results in a consistent suppression of the false alarm rate of the network. As a second improvement, if we require at least two or three operating detectors to perform the coincidence analysis, adding a new observatory increases the effective observation time for the analysis. Besides, a network with at least 3 detector sites gives the opportunity to solve the so-called *"inverse problem"*; in fact the network AURIGA-LHO-LLO, in simultaneous observation with different antenna patterns, provides enough informations to fully characterize the incoming signal (two coordinates for the directions and two independent polarizations). In the case of the AURIGA-LIGO network, the overabundance of informations can be used as a physical consistency test on the candidate events. In general, the addition of a detector with different antenna pattern in a network results also in a better coverage of the sky. This is not particularly significant in this specific case because of the low sensitivity of AURIGA (as will be discussed in the next chapter 4).

Chapter 4

Methodological considerations for a network of non-homogeneous detectors

In this chapter we propose 2 strategies to combine non-homogeneous detectors, i.e. detectors with different directional sensitivities, or *antenna patterns*. The definitions of the 2 strategies in (section 4.1) take into account only the geometrical aspects of the detectors involved. In other words, only detectors type and location have been considered, not their relative sensitivities.

As a practical illustration, we have applied both the methodologies to the AURIGA-LIGO network. Here we will consider the 2 Hanford interferometers as a single one (called LHO) because co-located, with the same antenna pattern and very similar sensitivities. To be more realistic, in section 4.2, we have introduced a scaling factor to weight for the lower sensitivity of AURIGA. From this section, we neglect the simple case of circularly polarized signals and focus exclusively on the linearly polarized case. The analysis of sky coverages will be completed by considering a re-orientation of the bar.

In section 4.3 we address our investigation to the improvements of the sky coverage when AURIGA is added to the pair LHO-LLO. Both the methodologies introduced in section 4.1 are taken into consideration.

4.1 Strategies to combine detectors with different antenna patterns

The directional sensitivity of a detector depends on its orientation and its operating principle. The output of gravitational wave detectors is converted in equivalent strain at input h_{eq} assuming the most favorable direction and polarization of the wave. The antenna pattern F is the scalar function which projects the strain h of the incident wave to h_{eq}:

$$h_{eq} = F(\theta, \phi, \psi; t) \cdot h \tag{4.1}$$

$$|F(\theta, \phi, \psi; t)| \leq 1 \tag{4.2}$$

where the coordinates are: direction (θ and ϕ) and polarization (ψ) of the source and time (t).

For both the resonant bars and the interferometric detectors, the dependence on ψ is:

$$F(\theta, \phi, \psi) = A(\theta, \phi) \cos(2\psi + \delta(\theta, \phi)). \tag{4.3}$$

In other words the antenna pattern of each detector is simply a sinusoidal function of the polarization angle ψ of the source with a phase δ depending on the direction. For this reason, any gravitational wave detector can be considered a *linear polarizer*. The function F_i depends on the source direction only through the magnitude and the phase. The importance of δ will be introduced in next sections. The magnitude A of equation 4.3 can be expressed as:

$$A = \sqrt{({F_+}^2 + {F_\times}^2)} \tag{4.4}$$

where F_+ and $F_\times$ are the antenna patterns for the plus and cross independent components of the polarization of h_{eq}:

$$h_{eq} = F_+ h_+ + F_\times h_\times. \tag{4.5}$$

In equation 4.3 we described the general dependence of the antenna pattern on ψ. To be more precise, $F(\theta,\phi,\psi)$ will be written in different ways according to the kind of detector considered:

$$F(\theta,\phi,\psi)=\begin{cases} W_{kl}n^k n^l & (bar) \\ \\ \frac{1}{2}W_{kl}(n^k n^l - m^k m^l) & (interferometer)\end{cases} \tag{4.6}$$

where **n** and **m** are the versors along the arms of the interferometer (**n** for the bar) and **W** is the gravitational wave polarization tensor.

In a network coincidence analysis, in order to reconstruct the amplitude h of the wave, the amplitude measured by any detector must be divided by its $F(\theta,\phi,\psi)$. This procedure has been extensively used by IGEC to implement a directional search (Astone *et al.* (2003)).

In the IGEC method, the first step consisted in a data selection performed by putting, on each detector, a threshold proportional to its F^{-1} for the target direction and polarization. On the following sections, we will refer to this strategy as the *detector-threshold strategy*. We will also propose an alternative strategy (referred to as the *product-threshold strategy*), in which we will characterize the directional sensitivity of a detector pair by means of the product of their antenna patterns F_1 and F_2. This is the most natural choice in the case of a cross-correlation search. In this case the reconstructed square of the wave amplitude h^2 is inversely proportional to $F_1 \cdot F_2$.

In the following of this section we will analyze this second strategy and we postpone to section 4.2 a comparison (through an example of network) between detector-threshold and product-threshold strategies.

Let us reconstruct the product of directional sensitivities for the pair of detectors 1 and 2. According to equation 4.3, $F_1 \cdot F_2$ is written as:

$$\begin{aligned} F_1(\psi)\cdot F_2(\psi) &= A_1\cdot A_2\,\cos(2\psi+\delta_1)\cos(2\psi+\delta_2) \\ &= A_1\cdot A_2\,\frac{1}{2}[\cos(4\psi+\delta_1+\delta_2)+\cos(\delta_1-\delta_2)]. \end{aligned} \tag{4.7}$$

Now we apply to the pair of detectors AURIGA and LHO the detector threshold and product threshold strategies. The first thing we need is the magnitude of the antenna pattern for each one of the 2 detectors, evaluated as in equation 4.4. The magnitudes A_1 and A_2 (for our example) are shown in figure 4.1. In the next subsections 4.1.1 and 4.1.2 we will focus on the importance of the relative phase shift $\delta_1 - \delta_2$ of equation 4.7 and the way it affects the sensitivity of the pair according to the polarization of the incoming signal.

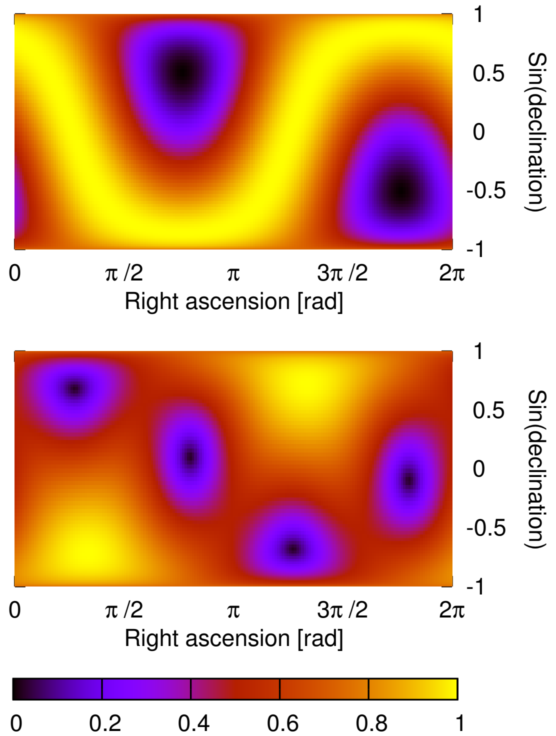

Figure 4.1: On the top: the magnitude A of the antenna pattern of AURIGA is shown respect to all the directions in the sky. On the bottom: the magnitude A of the LHO antenna pattern.

4.1.1 The case of linear polarization

Linearly polarized signals, by definition, are characterized by a polarization ψ which doesn't vary with time.

Let us consider again the pair of detectors AURIGA-LHO. To define the product of their antenna patterns we must combine (according to equation 4.7) the magnitudes A shown in figure 4.1 and their phases δ_1 and δ_2 (in figure 4.2 one can see the difference $\delta_1 - \delta_2$). Both magnitude and phase depend on the direction of the source. Moreover, $F_1 \cdot F_2$ is also modulated by the polarization signal ψ. For different values of ψ we get different sky coverages and, for each direction, there is a ψ for which $F_1 \cdot F_2$ nulls. To get a single representative picture of all the possible coverages, the absolute value of the product $F_1 \cdot F_2$ has been averaged over all the ψ. In figure 4.3 the result of $\langle |F_1 \cdot F_2| \rangle_\psi$ is shown for the pair of detectors in our example (AURIGA and LHO).

If we are interested in the sky coverage guaranteed by the single detectors AURIGA and LHO, the absolute value of their antenna pattern ($|F|$) must be averaged over ψ, see figure 4.4.

4.1.2 The case of circular polarization

Now we want to evaluate the product in equation 4.7 with respect to the other extreme case of signal polarization: the circular polarization.

A circularly polarized signal is, by definition:

$$\begin{pmatrix} h_+ \\ h_\times \end{pmatrix} = h(t) \begin{pmatrix} \cos(2\psi) \\ \sin(2\psi) \end{pmatrix} \tag{4.8}$$

where h_+ and $h_\times$ are the 2 independent components of wave amplitude. The polarization ψ can be written as:

$$\psi = 2\pi f_0 t \tag{4.9}$$

where f_0 is the rotation frequency of ψ and t is the time. If we assume that the amplitude $h(t)$ of the incoming wave is varying on time-scales longer than $1/f_0$ (i.e. if $h(t)$ can be considered constant during the period of ψ) we can state that the amplitude h, measured by two detectors in product-threshold strategy, is simply the product of the magnitudes of their antenna patterns. In fact, the relative phase $\delta_1 - \delta_2$ results in a *spurious time shift* Δt (see Gursel & Tinto (1989)) which can be written as:

$$\Delta t = \frac{\delta_1 - \delta_2}{2\pi f_0} \tag{4.10}$$

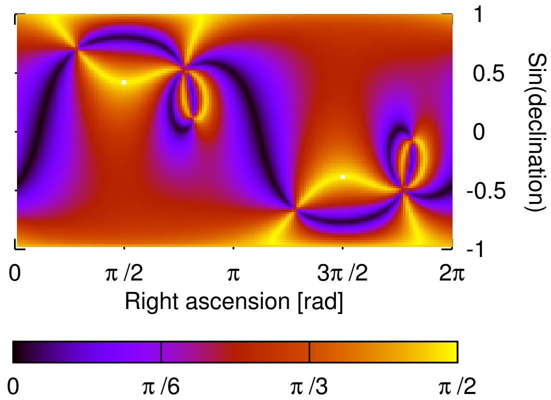

Figure 4.2: In this figure the absolute value of the difference $\delta_1 - \delta_2$, for the pair of detectors AURIGA-LHO, is shown for each direction in the sky.

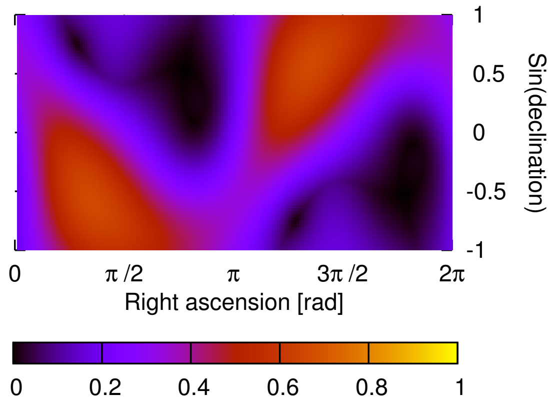

Figure 4.3: This is the result of the average, over all the polarizations, of the product $|F_1 \cdot F_2|$ for the pair of detectors AURIGA-LHO. This product fully corresponds to the integration over ψ, of the absolute value of equation 4.7 and represents the right procedure to multiply the 2 antenna patterns when the signal is linearly polarized. In the case of linearly polarized signal with polarizations isotropically distributed, this pattern represents the sky coverage of the network.

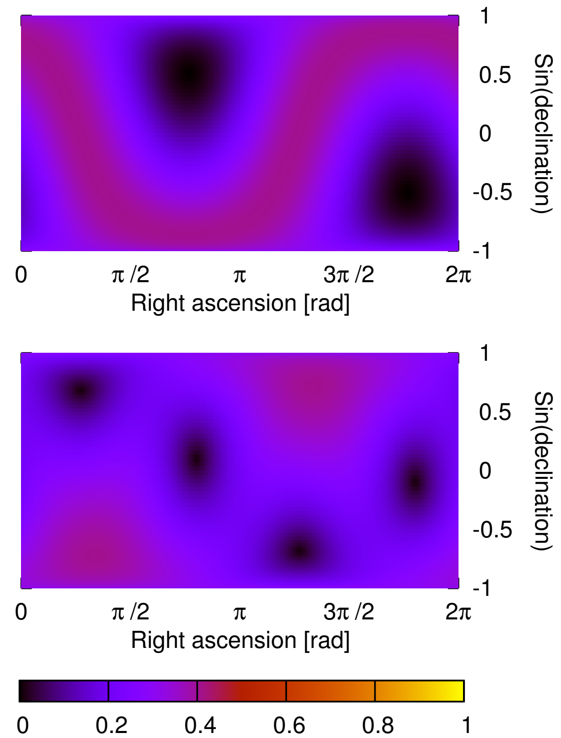

Figure 4.4: On the top: for each direction in the sky, the value of the AURIGA antenna pattern has been averaged over all the possible polarizations ($\langle |F_1| \rangle_\psi$). On the bottom: the same but evaluated for the Hanford interferometers ($\langle |F_2| \rangle_\psi$).

Its maximum value is:

$$|\Delta t| = \frac{1}{4f_0} \tag{4.11}$$

For a detector which works around 1 kHz this shift can reach 0.25 ms.

Hence, neglecting the contribution of the phase difference, the product of the antenna pattern of AURIGA and LHO is simply the product of the 2 magnitudes shown in figure 4.1 and it doesn't depend on ψ (see figure 4.5):

$$F_1 \cdot F_2 \quad = A_1 \cdot A_2 \tag{4.12}$$

It is worth to notice that there is a slight difference between the sky coverage guaranteed by the pair LHO-AURIGA in the case of linearly polarized signal (figure 4.3) and in the case of circularly polarized signal (figure 4.5).

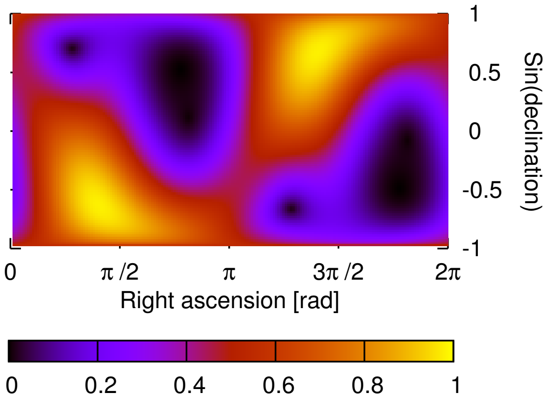

Figure 4.5: This is simply the product of the magnitudes of the antenna patterns for the two detectors AURIGA and LHO. This product correspond to the right procedure to multiply the two antenna patterns in the case of circularly polarized signal and gives the sky coverage in that particular situation.

4.2 The sky coverage of the network AURIGA-LHO-LLO

In this section we make a comparison between the product-threshold strategy and the detector-threshold strategy (introduced in section 4.1) by analyzing the sky coverage guaranteed by the same detectors with respect to linearly polarized signals. In fact, this is the most tangled case and final considerations on the network can be completed by considering the re-orientation of the bar. As an example, we will consider all the detectors involved in the AURIGA-LIGO data exchange.

In order to give more realistic coverage estimations, we have added to the geometrical considerations an "handicap factor" to decrease the sensitivity of AURIGA respect to the LIGO observatories. This has been done by means of a scaling factor 1/3 applied to the antenna pattern of AURIGA. In doing so we have simulated the configuration of a network where the 2 LIGO are 3 times more sensitive than AURIGA. The particular scaling factor introduced in this analysis is motivated by the sensitivities shown in figure 3.2.

4.2.1 The product-threshold strategy

As explained in section 4.1, the product threshold strategy requires thresholding the product of the detectors' antenna patterns.

In the case of a 3-detectors network, we decided to threshold all the possible pairs (2-fold coincidences), in order to maximize the sky coverage. Hence, in a product-threshold strategy, we calculate the sky coverage guaranteed by the network in 2-fold coincidence by imposing that (at least) one of the three products of pairs of antenna patterns is above a fixed threshold. A scalar which summarizes the sky coverage over all the directions (θ, ϕ) is simply the integration:

$$\alpha = \frac{1}{2} \int d(\sin\theta) \, \frac{1}{2\pi} \int d\phi \bigcup_{i,j;\ i \neq j} \left(\int_{F_i \cdot F_j > threshold} d\psi \right) \tag{4.13}$$

For the present orientation of AURIGA (44 degs, clockwise from North) the sky coverage of the AURIGA-LHO-LLO network is $\alpha = 0.5386$ (if we take a threshold of 0.1) and $\alpha = 0.9562$ (if we take a threshold of 0.01).

If we want to investigate if this coverage would be better by rotating the bar, we must repeat the same requirements as before but changing the azimuth of AURIGA in the formula of its antenna pattern. We get the results summarized in table 4.1.

Azimuth (degs)	Threshold at 0.1	Threshold at 0.01
10	0.5515	0.9630
20	0.5485	0.9601
30	0.5429	0.9564
40	0.5391	0.9566
50	0.5390	0.9552
60	0.5435	0.9527
70	0.5494	0.9532
80	0.5554	0.9514
90	0.5653	0.9486
100	0.5669	0.9495
110	0.5641	0.9537
120	0.5586	0.9574
130	0.5504	0.9611
140	0.5434	0.9653
150	0.5422	0.9657
160	0.5444	0.9661
170	0.5458	0.9653
180	0.5474	0.9644

Table 4.1: On the first column all the considered values of azimuth for the AURIGA detector are shown. The second column indicates the coverage (in the product-threshold sense) guaranteed by pairs of detectors in the network AURIGA-LHO-LLO over the threshold 0.1. On the third column: the same coverage (α) but referring to threshold 0.01. All these values refer to linearly polarized signals.

From table 4.1 we deduce that it is not of great relevance the orientation of the bar for this kind of search: the coverages are all very close.

4.2.2 The detector-threshold strategy

The second strategy introduced in section 4.1 is the so called detector-threshold strategy. In this case the antenna pattern of all the detectors must singularly be above a fixed threshold. In what follows, the thresholds have been chosen to be comparable with the ones applied in the product-threshold strategy, i.e. they are the square root of 0.1 and 0.01 (0.3 and 0.1). Considering the square root of the product thresholds allows only a first order comparison of the sky coverages in the 2 strategies. A complete comparison would require to completely specify each network analysis, to be able to take into account the detection efficiency and the false alarms. Here we limited our investigation on the effect of the directional sensitivity alone, neglecting the noises introduced by the detectors.

Of course, we expect that the sky coverage of the detector threshold strategy be smaller than the ones in section 4.2.1 because now we require a 3-fold coincidence.

The lower sensitivity of AURIGA is taken into account, as usual, by multiplying its antenna pattern by a factor 1/3. This, obviously, makes the threshold 0.3 not particularly significant: the maximum value AURIGA can take is 0.33.

The fraction of sky covered by a network, in the detector-threshold sense, must be defined as the average, over all the directions, of the fraction of polarizations simultaneously seen by all the detectors. Here, with the term "seen", we mean the antenna pattern of the detector must be above a predefined threshold.

We will analyze here the 3-fold coincidence, in detector-threshold sense, between AURIGA, LHO and LLO. For the present orientation of AURIGA (44 degs, clockwise from North), the sky coverage of this network is 0.4582 with a threshold 0.1.

In the following table 4.2 the fractions of sky covered by the 3 detectors (averaged over all directions and polarizations), are shown for different values of

AURIGA azimuth and the thresholds 0.3, 0.1 and 0.01.

Azimuth (degs)	Threshold at 0.3	Threshold at 0.1	Threshold at 0.01
10	0.0220	0.4321	0.9111
20	0.0275	0.4417	0.9114
30	0.0356	0.4493	0.9114
40	0.0450	0.4562	0.9118
50	0.0497	0.4586	0.9112
60	0.0478	0.4562	0.9111
70	0.0410	0.4489	0.9110
80	0.0357	0.4393	0.9108
90	0.0306	0.4360	0.9112
100	0.0267	0.4356	0.9109
110	0.0226	0.4353	0.9104
120	0.0238	0.4380	0.9103
130	0.0283	0.4385	0.9110
140	0.0323	0.4338	0.9110
150	0.0302	0.4334	0.9104
160	0.0248	0.4297	0.9108
170	0.0203	0.4249	0.9107
180	0.0187	0.4262	0.9104

Table 4.2: In the first column all the considered azimuth are shown. In the second one the fraction of the sky (averaged over all directions and polarizations) covered (in the detector-threshold sense) by the three detectors LHO, LLO and AURIGA is shown for linearly polarized signals. We have required that all the antenna patterns are simultaneously above a threshold of 0.3. (This column is not particularly significant: in fact, because of the handicap due to its lower sensitivity, AURIGA can reach, as a maximum value, only 0.33). In the third column the same is shown for a threshold at 0.1. The fourth column (threshold at 0.01) has been added to show that, to significantly improve the efficiency, we have to lower the threshold to few percent of the antenna pattern. We don't notice a great difference in reorienting the bar.

From table 4.2 it's possible to notice that there is not a great difference in the detection efficiency for different azimuths. Like in the previous strategy, we must conclude that it is not of any advantage re-orienting the bar.

4.3 Contribution of AURIGA to the network

In this section we will focus on the contribution to the sky coverage given by AURIGA and we will discuss how the sky coverage of the pair LHO-LLO changes after introducing the bar. We will analyze the problem from the different points of view of the product-threshold and the detector-threshold strategy. Also in this section the only class of considered signals is that of linearly polarized signals.

4.3.1 The product-threshold strategy

Let us consider the 2 networks: LHO-LLO and LHO-LLO-AURIGA. We choose, as a strategy of detection, the product-threshold strategy (i.e. to be above a certain threshold with the product of the antenna patterns). We want to compare the sky coverage of the first and the second network with the requirement of considering double coincidence detections. In other words, in the case of LHO-LLO we simply require that the product of the 2 antenna patterns is above the chosen threshold, and in the case of LHO-LLO-AURIGA we require that at least one of the three products (between the possible pairs LHO-LLO, LHO-AURIGA or LLO-AURIGA) is above the same threshold. If we assume an homogeneous distribution of source polarizations, we can interpret this result as the fraction of polarizations "seen" by the network with respect to each direction.

To make this comparison, we have taken into account the different sensitivity of the bar with respect to the interferometers: the antenna pattern of AURIGA is considered, as before, with an handicap of 1/3.

In figure 4.6 the product-threshold has been applied to LHO-LLO. Now, we recall the definition of α (see equation 4.13) which gives an average (over all the possible directions and polarizations) of the fraction of sky seen by a pair of detectors (with respect to a particular threshold). For LHO-LLO, if we take a threshold of 0.1 (top figure of 4.6) this integration gives $\alpha = 0.5206$, if we take a threshold of 0.01 it returns $\alpha = 0.8658$ (bottom figure of 4.6).

In figure 4.7 the product-threshold has been applied to the possible pairs in the network LHO-LLO-AURIGA. The values of α in this configuration are the same anticipated in section 4.2.1 (i.e. $\alpha = 0.5386$ for a threshold of 0.1 and $\alpha = 0.9562$ for a threshold of 0.01).

By comparing figure 4.6 and 4.7 we notice that: the improvement of the sky coverage obtained by adding AURIGA is not visible if we require to be above a threshold of 0.1 by at least one product of antenna patterns. The situation improves if we lower the threshold to 0.01: in this case the addition of the AURIGA detector, improves the "view" of the network with respect to almost all the directions. However, it is worth to notice that the sky coverage of LHO-LLO was already very high and this improvement is generalized in the sky but, on the average, limited to few percent of the fraction of visible polarizations.

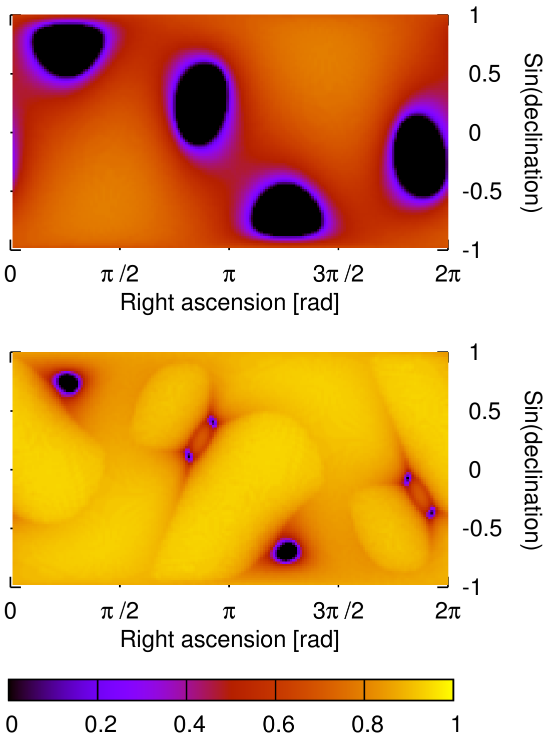

Figure 4.6: Fraction of polarizations seen by the pair LHO-LLO in the case of product-threshold: the product of the 2 antenna patterns of LHO and LLO is requested to be above a certain threshold. The fraction of polarizations which respects this requirement is plotted for each direction. On the top: threshold at 0.1. On the bottom: threshold at 0.01. The two interferometers have been considered with the same sensitivity.

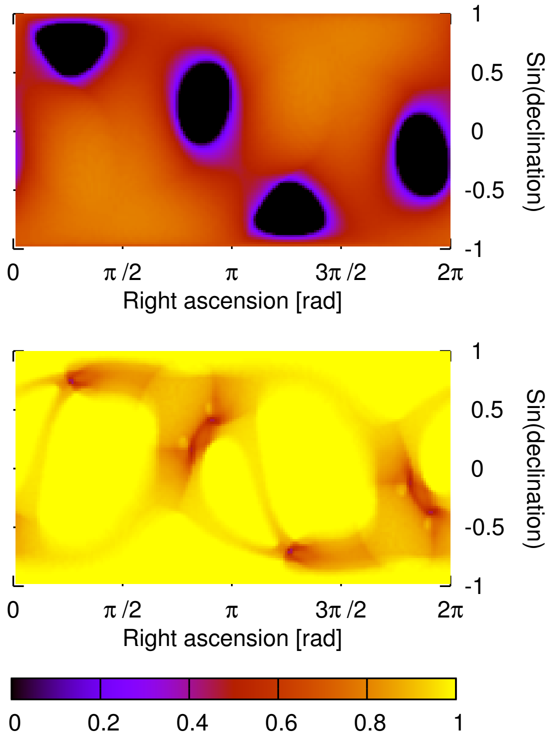

Figure 4.7: Fraction of polarizations seen by (at least!) one of the three possible pairs of detectors we can form with LHO, LLO and AURIGA in the case of product-threshold strategy. The threshold is put on the 3 possible products of pairs of antenna patterns, and we require that at least one of them is above the threshold. This gives us the fraction of polarizations seen in each direction in the case of homogeneous distribution of polarizations. As in figure 4.6: on the top: threshold at 0.1; on the bottom: threshold at 0.01. For this plot AURIGA has been weighted with a factor 1/3 to take account of its lower sensitivity with respect to the interferometers.

Now, it is interesting to inquire into the exact contribution given by the AURIGA detector to the plot of figure 4.7. In particular, we want to calculate the portion of the sky seen by at least one of the pairs LHO-AURIGA LLO-AURIGA while LHO-LLO is not sensitive.

We have calculated that, for the present orientation of AURIGA, the fraction of the sky (averaged over all the polarizations and directions) for which at least one of the two pairs AURIGA-LHO and AURIGA-LLO is sensitive (in the product-threshold sense) while the pair LHO-LLO is not is about $\alpha = 0.0180$ for a threshold at 0.1, and about $\alpha = 0.0904$ for a threshold at 0.01.

We can expect an improvement of these numbers if we tune opportunely the orientation of AURIGA. For this reason, it is of main importance to study how the joint coverage of AURIGA-LHO and AURIGA-LLO changes in rotating the bar.

For the present orientation of AURIGA (44 degs, clockwise from North), the fraction of the sky (averaged over all polarizations and directions) for which (at least!) one of the pairs AURIGA-LHO and AURIGA-LLO is sensitive (in the product-threshold sense) is about $\alpha = 0.2474$ in the case of threshold at 0.1, and about $\alpha = 0.8362$ if the threshold is at 0.01. If we want to see how α changes by rotating the bar, table 4.3 shows us the different coverages (referring to several azimuths) for the same thresholds.

From table 4.3 we notice that, if we reorient the bar, it is possible to improve the detection for threshold 0.1 only by a factor 1% (the best azimuth is about 60°), while if we put the threshold to 0.01, the better azimuth (about 160°) gives an improvement of about 3%. Because of these results, once again, we do not consider reorienting a convenient strategy.

4.3.2 The detector-threshold strategy

Now we change the strategy of detection and we require that the antenna pattern of each single detector in the network is simultaneously above the same threshold (here AURIGA is considered with the same handicap of 1/3 of section 4.3.1 and figures therein). The thresholds taken into account have been chosen to be the

Azimuth (degs)	Threshold at 0.1	Threshold at 0.01
10	0.2053	0.8534
20	0.2176	0.8488
30	0.2263	0.8438
40	0.2417	0.8378
50	0.2528	0.8341
60	0.2545	0.8359
70	0.2469	0.8371
80	0.2346	0.8377
90	0.2239	0.8374
100	0.2166	0.8415
110	0.2127	0.8469
120	0.2111	0.8510
130	0.2110	0.8542
140	0.2069	0.8564
150	0.2025	0.8593
160	0.1961	0.8608
170	0.1908	0.8597
180	0.1924	0.8565

Table 4.3: In the first column all the considered azimuths are indicated (with a step of $10°$). In the second one, the fraction of the sky (averaged over all polarizations and directions) for which at least one of the products of the antenna pattern LHO-AURIGA LLO-AURIGA is above the threshold 0.1 is indicated. In the third column: the same but with threshold at 0.01.

square root of the ones applied in section 4.3.1 (as in the previous sections). Once again we consider linearly polarized signals.

Figure 4.8 shows the sky coverage guaranteed by the pair LHO-LLO if we require that both their antenna patterns are above the threshold 0.3 (on the top) or 0.1 (on the bottom). Figure 4.9, instead, refers to the whole network LHO-LLO-AURIGA. Obviously the first threshold is not very significant: the sky coverage respect to a threshold 0.3 appears dominated by the shadow-zones of AURIGA because we have lowered its antenna pattern of 1/3, so its maximum value is now 0.33. The sky coverage referring to threshold 0.1 appears to be worse than the same threshold on figure 4.8 (0.4582 versus 0.7537) but we have to remind that, in the case of triple coincidence between three detectors, we have gained, for those regions in the sky, a better confidence of detection. In other words a search of this kind is not aimed to get a better sky coverage but to improve the false alarm rate.

Concluding, in this chapter we estimated the sky coverage of different network analysis strategies as applied to the AURIGA-LIGO network. Even though our estimations were based only on the directional sensitivity of the detectors, we can conclude that the AURIGA/LIGO-Hanford (LHO) and the AURIGA/LIGO-Livingston (LLO) pairs do not offer a significant improvement on the sky coverage of the LHO-LLO pair. This occurs mostly because the AURIGA sensitivity has been assumed 1/3 of the LIGO sensitivity. For this reason we cannot list a better sky coverage among the advantages of adding AURIGA to the LHO-LLO network. Nevertheless, AURIGA helps in the reduction of the network false alarm rate (in particular there is a significant portion of the sky seen by the 3-fold coincidences, see figure 4.9), it improves the statistical confidence of a possible detection and gives the possibility to solve the “inverse problem” and localize a source.

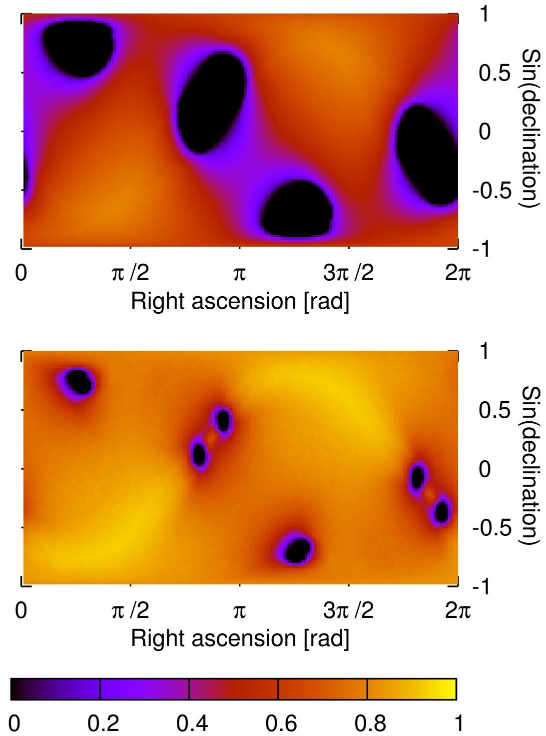

Figure 4.8: Fraction of polarizations seen by the pair LHO-LLO accordingly to a detector-threshold strategy: the threshold has been put on the single antenna patterns and we require that all satisfy the request to be above its. Top: threshold at 0.3; bottom: threshold at 0.1. These threshold have been chosen so that $0.3 \simeq \sqrt{0.1}$ and $0.1 = \sqrt{0.01}$, and we can roughly compare this plot with those of section 4.3.1.

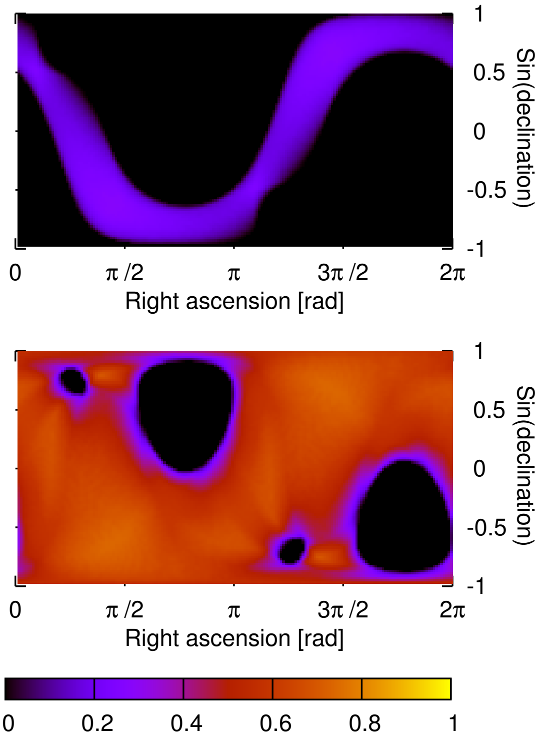

Figure 4.9: Fraction of polarizations seen by the network LHO-LLO-AURIGA in the detector-threshold sense: the requirement in this case is that all the antenna patterns of the three detectors must be above a threshold. In AURIGA, an handicap factor of 1/3 has been introduced. Top: threshold at 0.3; bottom: threshold at 0.1.

Chapter 5

Preliminary steps to the joint data analysis AURIGA-LIGO

This chapter starts describing the criteria used to select the joint observation time for the first AURIGA-LIGO joint analysis. All data quality assessments (applied independently by the two collaborations) are also presented in section 5.1.

The role of AURIGA in this analysis has been to provide the triggers for a wide-band cross-correlation analysis within the LIGO interferometers. To produce the triggers list, the AURIGA collaboration has been forced to modify the implemented AURIGA data analysis pipeline (`ada`) to take into account several noises featured by the spectrum during the coincidence run. A description of the analysis pipeline is given in section 5.2.

After the release of the triggers, the list has been processed in order to select only the events falling within the LIGO observation time (see section 5.3). The procedure has been repeated on a series of "off-source" data sets, built by time-shifting the LIGO data stream, with the purpose to get a representative set for tuning the analysis and estimate the rate of accidental coincidences in the not-shifted data set.

The subsequent step of the analysis, described in section 5.4, consists in a wide-band cross-correlation search performed on LIGO data around each trigger. First, all the "off-source" data sets have been processed. Then, once tuned and frozen the analysis as described in the next chapter, also the "on-source" data set has been analyzed.

5.1 Joint observation time

The first AURIGA-LIGO joint data taking covered the period from GPS time 756299212 to GPS time 757698029, with a total coincident run of 1398806 s ($\sim$ 388.6 h). This number takes into account just the superposition of LIGO run S3 (October 31, 2003 - January 9, 2004) and AURIGA run 331 (December 24, 2003 - January 13, 2004). Losses of lock (from LIGO side) and periods of operation in non-scientific mode (from both sides) are not taken into account in this number.

Before proceeding in the analysis, we have chosen to set aside a bench data set (called *playground*) to test the pipeline and the code in its first implementation. In order to avoid biases in the final results, the collaborations agreed to "sacrifice" this small subset of data ($\sim$ 10% of the whole data set) and exclude it from the final search. A detailed description of the criteria to select a representative playground will be given in section 5.1.1.

Next, a series of data quality assessments has been separately applied by the 2 collaborations before realizing the data exchange (as will be described in sections 5.1.2 and 5.1.3).

After the playground removal and the application of data validation criteria, the observation time of the network in quadruple coincidence resulted about 36 h. The triple coincidence AURIGA-LHO1-LHO2 has also been analyzed (other triple coincidence configurations were not considered, mostly because during $S3$ the Livingston interferometer featured the lowest duty cycle). The observation time in 3-fold coincidence (after playground and vetoes removals) reduces to 110 h (as summarized in table 5.3 of section 5.1.4). Of these, only the 74 h not yet analyzed as quadruple coincidence have been considered.

5.1.1 Playground selection and data subsets used for tuning the analysis

The use of a playground data set to test codes and pipelines is a strategy already used by the LIGO collaboration (e.g. LSC (2004), LSC (2005)). To be able to perform significant tests on the data analysis pipelines, the playground should be representative of all the features of the complete data set (such as non modelled noise, non stationary behavior, etc.). In this analysis, playground selection followed the definition used for the LIGO run S3 (Finn (2003)). The playground has been obtained by the rule:

$$T := \{[t_n, t_n + 600) : t_n = 729273613 + 6370n, n \in \mathbb{Z}\} \tag{5.1}$$

where 729273613 is the GPS start time of the previous LIGO run S2. Equation 5.1, in fact, has been inherited from the definition of playground used for S2. Time segments obtained from equation (5.1) can be considered a representative sample of S3 data and, in the same way, the intersection of the LIGO playground time with the AURIGA observation time gives a representative playground for the quadruple coincidence analysis. The intersection of LIGO playground with AURIGA livetime gives a test data set of 36.7 h ($\sim 9.4\%$ of the whole run, see also table 5.3). The extraction of playground time segments from the LIGO full data set has been performed by the tool `segwizard` of `LIGOtools` (see the LIGOtool web page).

Typically, the playground data set is exploited to set thresholds and tune the analysis before applying it to the remaining data set. This is important to prevent any a-posteriori choice in the analysis procedure which could jeopardize the statistical interpretation of the results. In our work, we used the playground data not only for a preliminary tuning of the analysis procedures but also for debugging the data analysis procedures. In fact, thanks to this exercise, we have been able to spot a code problem in drawing results.

After this initial step of tuning and debugging of the data analysis procedures, we have discarded the playground data set and decided to perform the final tuning of the analysis parameters (e.g. setting final thresholds etc.) on the remaining data. This has been accomplished by using the off-source instantiations of the complete data set obtained by time shifting the data series of the LIGO detectors with respect to each others (for a more detailed description see chapter 5.3).

Data from the playground have not been used for the final analysis, where only the remaining dataset (*non-playground*) has been analyzed.

5.1.2 AURIGA data quality selection

In principle, assuming Gaussian statistics, the AURIGA noise should be perfectly modelled by an analytic function expressed by a product of poles and zeroes. However, external non-modelled noises take part in affecting the detector sensitivity, as described in section 2.3. This environmental noise results in spurious lines and in a series of burst electromagnetic disturbances (referred to, in the following, as *wide-band events*). In order to overcome these problems, three main phases of vetoes have been implemented in the AURIGA data quality procedure: the *first level vetoes*, the *anti-coincidence vetoes* and the *second level vetoes*.

Periods of non-operation or maintenance vetoes belong to the first class of vetoes. None of these occurred during the coincidence run, since AURIGA took data continuously from December 24, 2003 to January 9, 2004.

However, during the coincidence run, data were significantly affected by *wide-band transients*. AURIGA is a resonant detector sensitive only in the 850-950 Hz range. None of the signals which deposit energy outside this bandwidth can be considered as a candidate event. Moreover, four sub-bands outside the AURIGA bandwidth (605-645 Hz, 655-685 Hz, 705-745 Hz and 755-795 Hz) have been continuously monitored to detect any excess of energy (with respect to a certain threshold) caused by the wide-band events. An anti-coincidence check has been implemented to veto the corresponding events detected in the sensitivity band, which can be considered as effects of wide-band electromagnetic spikes. This mechanism has also allowed to veto a great number of triggers due to other effects in band. In fact, most of the spurious lines featured by the AURIGA band during run 331 (see chapter 5.2) had a significant tail in the four sub-bands and the events they produced can be recognized by monitoring those frequencies. The number of candidate triggers vetoed using the wide-band check was about 30% of the total amount, while the loss in observation time was only 4%.

Second level vetoes applied to run 331 were those referring to non-Gaussianity of data (revealed by some quality monitors) or degraded detection efficiency. The whole run was divided in 579 time segments (each one of 2415.9 s [1]). On each time segment, software-injected signal (with a rate of 25 s^{-1} and a signal to noise ratio randomly distributed between 5.5 and 7.5) were introduced and searched by the AURIGA Data Analysis (`ada`), while an empirically-tuned algorithm selected "good" and "bad" segments, to keep or reject them. The validation criteria applied were the following: for each segment, the SNR distribution of the found events was evaluated; mean and sigma (m_1 and m_2) of the SNR distribution were evaluated for each time segment and compared to the mean values ($\overline{M}_1$ and $\overline{M}_2$) and RMS ($\sigma_{\overline{M}_1}$ and $\sigma_{\overline{M}_2}$) evaluated over all the segments. If m_1 or m_2 resulted at more than 3 sigmas from their mean values, the segment was rejected by a Chauvenet algorithm and the procedure was repeated recursively on the others. At the end, all the segments respecting the requirements:

$$\begin{aligned} Abs\left(m_1 - \overline{M}_1\right) \leq 3 \cdot \sigma_{\overline{M}_1} \\ Abs\left(m_2 - \overline{M}_2\right) \leq 3 \cdot \sigma_{\overline{M}_2} \end{aligned} \tag{5.2}$$

were kept.

As a final condition, a cut has been applied to the segments with much lower efficiency by requiring (for $SNR \geq 4.5$):

$$Efficiency \geq \tfrac{1}{3} \ . \tag{5.3}$$

As a result of criteria (5.2) and (5.3), 58% of the segments survived the cuts and have been considered for the data exchange.

[1] the length of the segments has been chosen to minimize bias effects from the model estimator tool. With longer segments we were unable to follow instabilities; with shorter segments we did not collect enough statistics for the estimations.

5.1.3 LIGO data quality selection

The first step in LIGO data quality validation has been performed on line in the control rooms of the Hanford and Livingston observatories. Here the scientific responsible defined *science mode* only those data streams which passed a certain number of figures of merits. Data passing this step were stored into series of non-overlapping time segments with extremes rounded off to integer seconds. Next data quality selection consisted in the application of a data quality flags set released by the LSC (LIGO Scientific Collaboration) Detector Characterization team (for the following analysis, version 05 of January 25, 2005 has been used, see for instance the LIGO Segment data quality repository on the web). These flags are associated to segments of data characterized by noise of known (or recognized) nature (e.g. seismic anomalies or calibration lines). After the release of the adopted version of data quality flags, the LSC found still a correlation between the gravitational channel and some auxiliary channels. For this reason care has been taken to extend by 1 minute both the extremes of seismic vetoes flags. All the applied flags (and the final rejected time associated to each one of them) are listed in table 5.1 (for the LHO1-LHO2-LLO coincidence) and table 5.2 (for the LHO1-LHO2 coincidence). The extraction of "good" segments from the full data set or from the non-playground data set has been done using the tool `segwizard` of `LIGOtools` (see the LIGOtool web page). The extensions of 1 minute to the end and the beginning of some flags has been performed by a shell script[1] based on `LIGOtool segments` v1.8.

5.1.4 AURIGA-LIGO: livetime of quadruple and triple coincidence

After the playground removal described in section 5.1.1, we reduced the total observation time from 388.6 h to 351.9 h with a playground of about 36.7 h (see table 5.3). During these 388.6 h, AURIGA livetime after vetoes resulted 190.6 h. After applying the LIGO validation criteria described in section 5.1.3, the LHO1-LHO2-LLO livetime resulted 61.4 h while the LHO1-LHO2 livetime resulted 132.0 h.

[1] `subtract_time_lists`, see the Handbook for the 1st LIGO-AURIGA analysis tools.

Flag	Affected IFOs	Extension	Vetoed time	
OUTSIDE_S3	H1 H2 L1		2396 s	(0.25 %)
UNLOCKED	H1 H2 L1		468 s	(0.05 %)
PRELOCKLOSS_10	H1 H2 L1		4309 s	(0.45 %)
DAQ_OVERFLOW	H1 H2 L1		12927 s	(1.35 %)
INVALID_TIMING	H1 H2		35349 s	(3.69 %)
LIGHTDIP	H1 H2 L1		589 s	(0.06 %)
CALIB_LINE_V03	H1 H2 L1		23191 s	(2.42 %)
FE_SYNCH_ERROR	L1		2071 s	(0.22 %)
ACOUSTIC_ELEVATED	H1 H2	± 60 s	3611 s	(0.38 %)
AIRPLANE	H1 H2 L1	± 60 s	16685 s	(1.74 %)
SEISMIC_ELEVATED	H1 H2	± 60 s	26973 s	(2.82 %)
SEISMIC_HIGH	H1 H2	± 60 s	1401 s	(0.15 %)
SEISMIC_TRANSIENT	H1 H2	± 60 s	1184 s	(0.12 %)
DUST	H1 H2 L1		154846 s	(16.18 %)

Table 5.1: List of data quality flags used in the selection of LIGO S3 data for the AURIGA-LHO1-LHO2-LLO burst search. In the first column the flags applied to reject data. The second column shows which interferometer was affected by each one. The third column specifies which flag was extended (of 60 seconds to both the extremes) because of recognized transient environmental disturbances. The last column reports on the livetime loss associated to each flag in S3 data (all times refer to full data set, the playground removal was not applied).

Flag	Affected IFOs	Extension	Vetoed time	
OUTSIDE_S3	H1 H2		13458 s	(0.41 %)
UNLOCKED	H1 H2		694 s	(0.02 %)
PRELOCKLOSS_10	H1 H2		6923 s	(0.21 %)
NO_DATA	H1 H2		595 s	(0.02 %)
NO_RDS	H1 H2		659 s	(0.02 %)
DAQ_OVERFLOW	H1 H2		2836 s	(0.09 %)
INVALID_TIMING	H1 H2		62300 s	(1.88 %)
LIGHTDIP	H1 H2		220 s	(0.01 %)
CALIB_LINE_V03	H1 H2		58894 s	(1.78 %)
ACOUSTIC_ELEVATED	H1 H2	± 60 s	11668 s	(0.35 %)
AIRPLANE	H1 H2	± 60 s	22827 s	(0.69 %)
SEISMIC_ELEVATED	H1 H2	± 60 s	141059 s	(4.26 %)
SEISMIC_HIGH	H1 H2	± 60 s	10361 s	(0.31 %)
SEISMIC_TRANSIENT	H1 H2	± 60 s	635 s	(0.02%)
DUST	H1 H2		244409 s	(7.38 %)

Table 5.2: Same of table 5.1 but referring to the LHO1-LHO2 coincidence used for the burst search with the network AURIGA-LHO1-LHO2.

If we restrict the observation time to the coincidence AURIGA-LIGO, the observation time after playground and vetoes removals was 36.0 h for the quadruple coincidence AUR-LHO1-LHO2-LLO and 110.0 h for the triple coincidence AUR-LHO1-LHO2. Of these, we have considered only 74.0 h, i.e. only the time not previously analyzed as "quadruple coincidence". The final livetimes used for the analysis of quadruple and triple coincidence are listed in table 5.3.

Coincident Run	1398806 s	388.6 h
Playground	132000 s	36.7 h
After playground removal	1266806 s	351.9 h
After AURIGA epoch veto (exchanged triggers):	686049 s	190.6 h
LHO1-LHO2-LLO triple-coincidence (with DQ flags):	221027 s	61.4 h
LHO1-LHO2 double coincidence (with DQ flags):	475201 s	132.0 h
AUR-LHO1-LHO2-LLO:	129699 s	36.0 h
AUR-LHO1-LHO2:	266544 s	74.0 h

Table 5.3: Observation times for the LIGO observatory, the AURIGA detector and the two network configurations AURIGA-LHO1-LHO2-LLO and AURIGA-LHO1-LHO2. All the observation times are computed after playground removal. The time budget of the configuration AURIGA-LHO1-LHO2 is obtained after removing the time segments already analyzed for the quadruple coincidence AURIGA-LHO1-LHO2-LLO.

5.2 The AURIGA triggers

Since the role of the resonant detector in the first AURIGA-LIGO joint analysis was to provide the triggers for the LIGO observatories, the AURIGA collaboration was forced to solve problems related to periods of large environmental disturbances in its data.

In fact, run 331 occurred during the first data taking after the hardware upgrade of the previous years (Bignotto *et al.* (2005), Zendri *et al.* (2003),Baggio *et al.* (2005)) but before the new suspensions setup was installed (as explained in section 2.3.2). The appearance of unexpected excess noise (see figure 5.1), due to the increase of the bandwidth, forced the AURIGA team to modify the AURIGA data analysis (`ada`) in order to cope with several "families" of spurious lines (see Fattori (2004)). All the spurious lines present in the AURIGA sensitivity band in that period can be reported to these main families of noise:

1. The first class of spurious lines can be clearly identified in figure 5.1 and is represented by 5 lines in the detection band: 866.6 Hz, 877.1 Hz, 883.9 Hz, 909.8 Hz and 935.7 Hz. These lines (all strongly correlated and characterized by the same peculiarities) were always present in the sensitivity band for all the duration of run 331 (except for short periods of minutes). Their amplitude was clearly related to human activities and featured an evident "day-night" effect. Their frequency was found to be slightly dependent on the amplitude. Sometimes, the presence of the line at $f_0 = 909.8$ Hz was coupled to the appearance of some other peaks regularly spaced at its sides with frequencies f_n following the rule:

$$f_n = (f_0 + n \times 5.26)\, Hz \tag{5.4}$$

   with $n = \pm 1$ or ± 2. A correlation between the appearance of these lines and an excitation of low-frequency lines (around 20 Hz), typical of the suspensions, has been observed. For this reason, the current interpretation connects these phenomena to up-conversions in band of seismic noise through non-linear terms in the suspension dynamics.

   To white raw data from this class of noise, the 5 spurious lines have been fitted as Lorentzian modes and their contributions have been subtracted to the noise spectrum model (see figure 5.1). Nevertheless, sometimes the non-stationarity of these lines was faster than the capability of the algorithm to track their fluctuations. In these cases, whitening of data became very hard and an excess of non-modeled noise "dirtied" the list of candidate events with clusters of non-Gaussian events.

2. The spectrum in band featured the presence of a second important class of noise which must be taken into account to get a reliable whitening of the raw data set. The lines of this family (867.9 Hz, 870.5 Hz, 900.2 Hz, 943.9 Hz, 946.6 Hz, 962.1 Hz and 967.6 Hz) shared with the previous family a

"day-night" effect but differed because of frequencies which did not vary with time. Because of the stable frequency, in the phase of whitening data these lines have been treated with a narrow band cut around the frequency of interest.

Besides, there was another class of noise which cannot be whitened with the strategies described above, the *wide band transients*: disturbances of short duration (less than 20 ms) which deposited most of their energy outside the sensitivity band. These transients were consistent with an impulsive electromagnetic excitation at the transducer. The spurious bursts produced in band by these phenomenas could be rejected from the list of candidate triggers only by means of the anti-coincidence vetoes described in section 5.1.2.

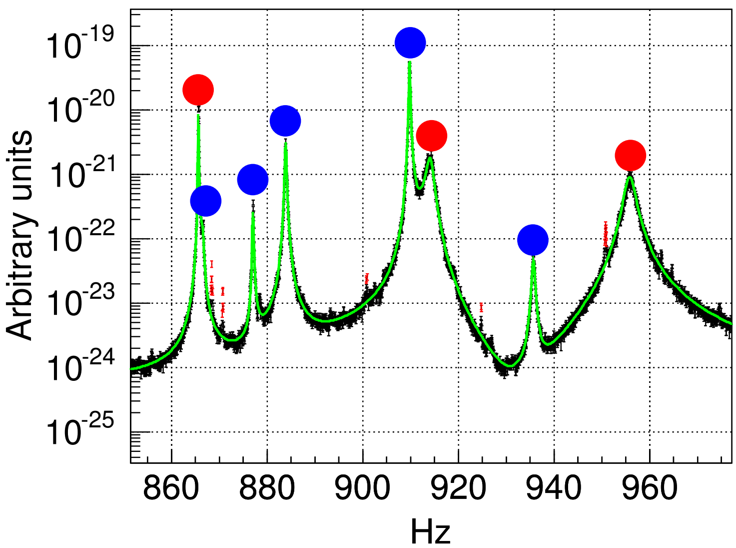

Figure 5.1: AURIGA (not calibrated) RAW spectrum during the coincidence run. Red markers indicates the 3 fundamental modes: at about 865 Hz, 914 Hz and 956 Hz. Blue markers refer to spurious lines of the first class. To be whitened from data, these lines have been fitted as Lorentzian modes and appear on the fitting poles-and-zeroes function (green line) which models the detector noise. Some more noisy line is visible in the plot (red dots) which refers to spurious lines of the second class.

5.2.1 Production

The AURIGA data analysis (`ada`) is based on a modular, open source project supported by libraries such as `root` (see the root web page), `FrameLib` (see the FrameLib web page), `fftw` (see the fftw web page), `lal` (see the lal web page), `mkfilter` (see the mkfilter web page). The triggers production is performed by several interacting modules of analysis. Here I will describe the main blocks which allowed to generate the released triggers list for the data exchange. The schema of the complete pipeline is resumed in figure 5.2.

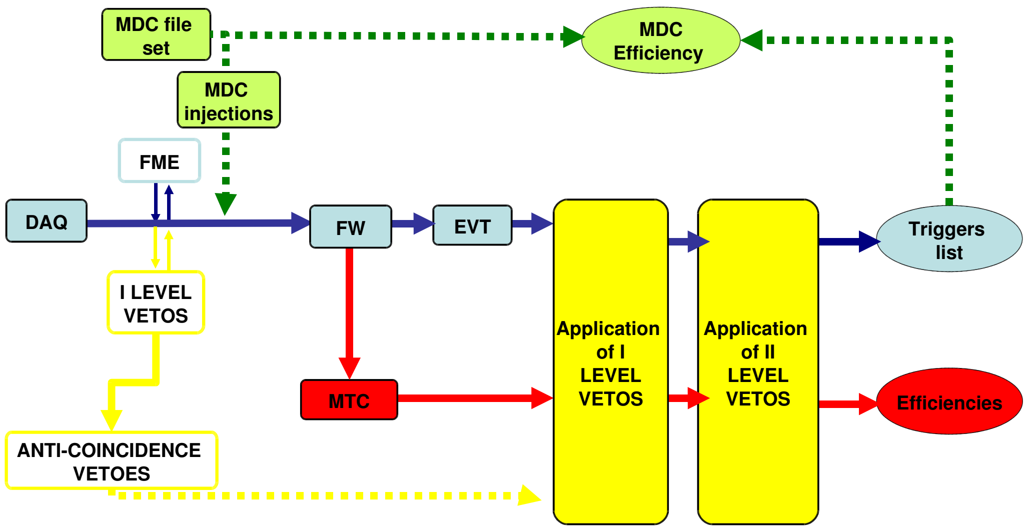

Figure 5.2: AURIGA analysis pipeline used to produce triggers for the AURIGA-LIGO analysis. In blue the main pipeline (i.e. the pipeline which refers to event production). In red: pipeline to produce the efficiency curve by means of Monte Carlo. In green: steps of analysis, introduced in the code for the first time for this analysis, which produce the efficiency curve by means of MDC injections. In yellow: the veto procedure. More details on each analysis-block in the text (section 5.2.1).

The storing of AURIGA data is possible through the acquisition system (Cesaracciu *et al.* (2003)). ADC-type (Analog-to-Digital Converter) frames are built and stored in the `DAQ` (Data Acquisition) module of `ada` and passed to the analysis. It is also possible to inject in the analysis pipeline a series of simulated frames (in that case called `DAQS`) constructed by `ada` using ARMA algorithms[1]. Moreover, it is possible to inject simulated signals directly on real data (bursts or periodic signals). To perform the LIGO-AURIGA analysis, `DAQ` module of `ada` has been modified to implement the possibility to menage MDCs data frames (see section 6.2).

After storing, raw data are passed to the module `FME` (Full Model Estimate). Through 2 subsequent phases, `FME` reconstructs the analytic part of the noise model and stores the evaluated parameters. In `phase 1` a buffer is filled with consecutive periodograms. Only a fraction of the periodograms is selected to reconstruct the spectrum, while a fixed percentage[2] of the most noisy ones is rejected. The remaining spectrograms are fitted using a `MIGRAD`[3] routine by taking care to exclude each frequency bin affected by spurious lines of the second class and to fit with Lorentzian poles and zeroes the spurious lines of the first class. After a first model has been produced, `FME phase 1` recycles the time series and the fit parameters are computed once more after removing the bins with higher deviation from the fit. Other outlier removal algorithms are called by the `phase 2` to smooth the fluctuations in time of the estimated parameters. This is helpful to get a reliable fit of the model also in case of transient noises.

The task of whitening is carried out by the module `FW` (Full Whitening). As a first step, this block performs a band-pass Butterworth filter and a decimation in the time domain. Then, `FW` gets the noise model from `FME phase 2`, performs accordingly the whitening in frequency domain of the AURIGA bandwidth and saves the resulting frames.

The final lists of events is produced by the `EVT` (Event search) module. This performs a matched template filtering and event search on whitened data. Care needs to be taken to provide whitened data suitable for the specified template to search. A max-hold algorithm searches for local maxima (with respect to a

[1] Also every subsequent module in the analysis provides the possibility to test each step with simulated data.

[2] This percentage is empirically chosen on the basis of the noise featured by each run.

[3] `MIGRAD` is an algorithm for minimization capable to calculate the differentials on the fly.

given dead time) and checks the crossing of a given threshold. If this happens, a candidate event trigger is issued. For each event trigger, the exact time of arrival and amplitude are computed after fine interpolation of the samples.

The task of computing the errors distribution and the efficiency of event parameters estimators is performed by `MTC` (Monte Carlo). This module returns a numerical estimation of the distributions of arrival time, amplitude errors and detection efficiency, for a chosen bank of templates. Software injection of signals (and subsequent search) takes place in the time domain, by adding the chosen template to the filtered data. This operation is cycled for specified time and amplitude increments and, finally, returns the residuals of differences between injected and measured event parameters.

To be released as triggers, the AURIGA events list needed to satisfy the data quality validation described in section 5.1.2. In particular, the wide-band vetoes affected the 4% of the observation time, while 42% of the time was affected by second level vetoes.

The list of candidate triggers for the first AURIGA-LIGO joint data analysis has been realized by thresholding the output of the optimal filter matched to a delta-like signal. After the data quality assessments, only the candidate triggers with $SNR \geq 4.5$ have been exchanged. The exchange threshold of 4.5 has been chosen to ensure a satisfactory significance of the candidate triggers. The triggers list released by the AURIGA collaboration for the joint analysis with LIGO consisted of 182516 events distributed over 190.6 h. Each event was characterized by the following informations:

i. Arrival time (with error). The arrival time was given in GPS seconds. Its error corresponded to the RMS of the arrival time as estimated by the Monte Carlo module. For this purpose a Monte Carlo simulation was run on a bank of δ-like software injected signals. The uncertainties estimated were inversely proportional to the SNR of each event.

ii. SNR (with error). The SNR is the measured signal to noise ratio in amplitude of the event. Its uncertainty was given at 1σ.

iii. Amplitude (with error). The amplitude (given in Hz^{-1}) corresponded to the amplitude of the δ template used in the search. The uncertainty (also in Hz^{-1}) corresponded to the standard deviation of the amplitude estimation and it is also provided by the Monte Carlo.

iv. χ^2 value (with 20 degrees of freedom) of the event respect to the δ template.

The events have been exchanged in the form of a `root` "ntuple".

5.2.2 Characteristics

To test the Gaussianity, stationarity and main statistical properties, the characteristics of the AURIGA triggers data set has been analyzed.

During the coincidence run, the uncertainties on the triggers arrival times (evaluated as explained in the previous section 5.2.1) varied from some fraction of ms to 40 ms, with an average of $\sim$ 10 ms. Besides, AURIGA featured a significant variability in the rate of events produced, as can be observed from figure 5.3. The rate per minute could vary of 1 order of magnitude in few minutes. Moreover, arrival time distribution was far from a Poisson distribution. This feature is enlightened in figure 5.5 where the autocorrelation of the triggers is shown with respect to the time of correlation. In this plot the number of coincidences has been evaluated between the trigger arrival times and theirselves after a shift. The shifts considered (from -500 s to $+500$ s) are shown on the x axis. For triggers over the higher thresholds, a clustering is clearly visible up to $\sim$ 300 s. This effect is the result of a non-perfect filtering of spurious lines with non-stationarity in that time scales. A correlation around 20 s is shown for events above the lower thresholds.

In figure 5.4 the time series of the exchanged h is shown with respect to the full coincidence run. The variability of h mirrors in a significant variability of the SNR. The SNR distribution for all the exchanged triggers has been produced and superimposed to the same distribution restricted to the periods of quadruple and triple coincidence (figure 5.6).

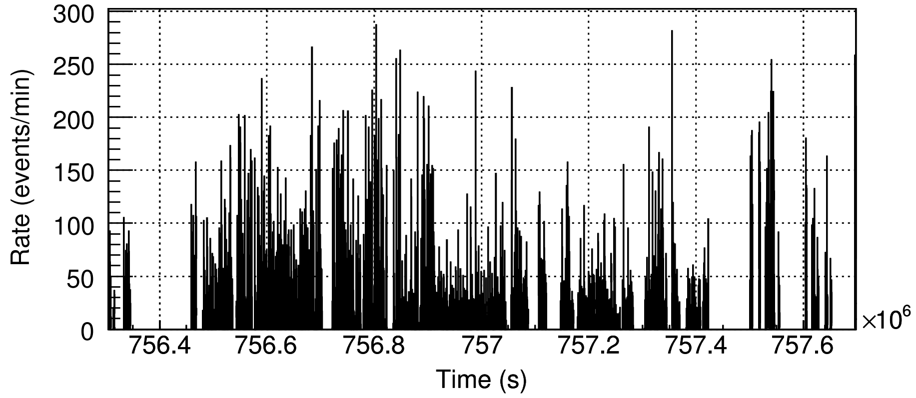

Figure 5.3: Rate of exchanged AURIGA triggers per minute. Time (on the x axis) is expressed in GPS seconds.

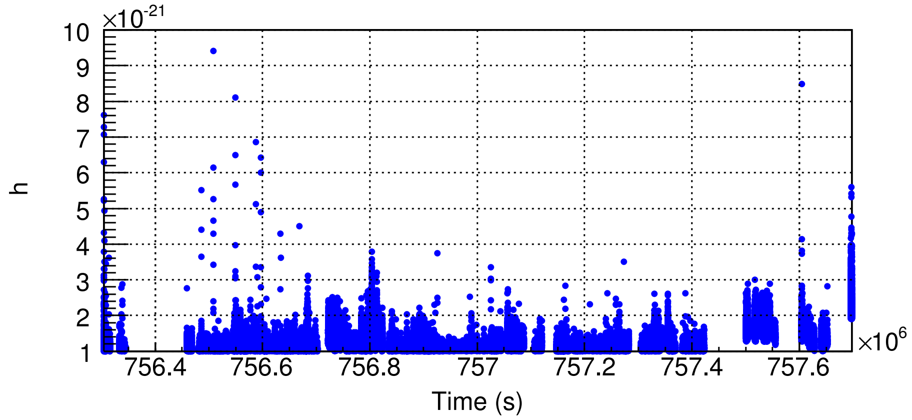

Figure 5.4: Time distribution of the amplitudes h of AURIGA triggers. Time (on the x axis) is expressed in GPS seconds.

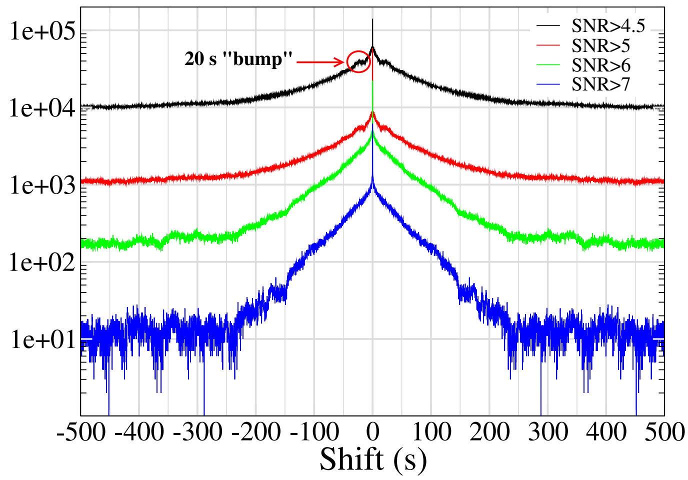

Figure 5.5: Auto-coincidences of the AURIGA exchanged triggers. The plot is obtained by shifting, back and forth, the triggers arrival time from -500 s to $+500$ s and counting the coincidences. Different curves refer to triggers above different thresholds: in black $SNR > 4.5$, in red $SNR > 5$, in green $SNR > 6$, and in blue $SNR > 7$. Highest events show a correlation within timescales of 200-300 s while, at the lower thresholds, a "bump" is present around 20 s.

5.3 Triggers selection and "off-source" measurements

The event list produced by the AURIGA analysis system (see previous section 5.2) must be reduced to the triggers falling in LIGO time segments before to be passed to the `CorrPower` algorithm (see section 5.4). In the quadruple coincidence analysis only AURIGA triggers which fall in the LIGO LHO1-LHO2-LLO segment list have been taken into account (the 221027 seconds obtained with the quality requirements described in section 5.1.3). The same has been done for the triple coincidence AURIGA-LHO1-LHO2, where the list to consider was the LHO1-LHO2 segment list (475201 seconds).

In order to estimate the rate of accidental coincidences, we built independent "off-source" data sets by applying many different time shifts to the LIGO data sets[1]: we kept fixed the AURIGA event time, assigned a time lag to the Hanford

[1]the two Hanford detectors have not been shifted relative to each other, in order to account, in our estimation, for local Hanford correlated noise.

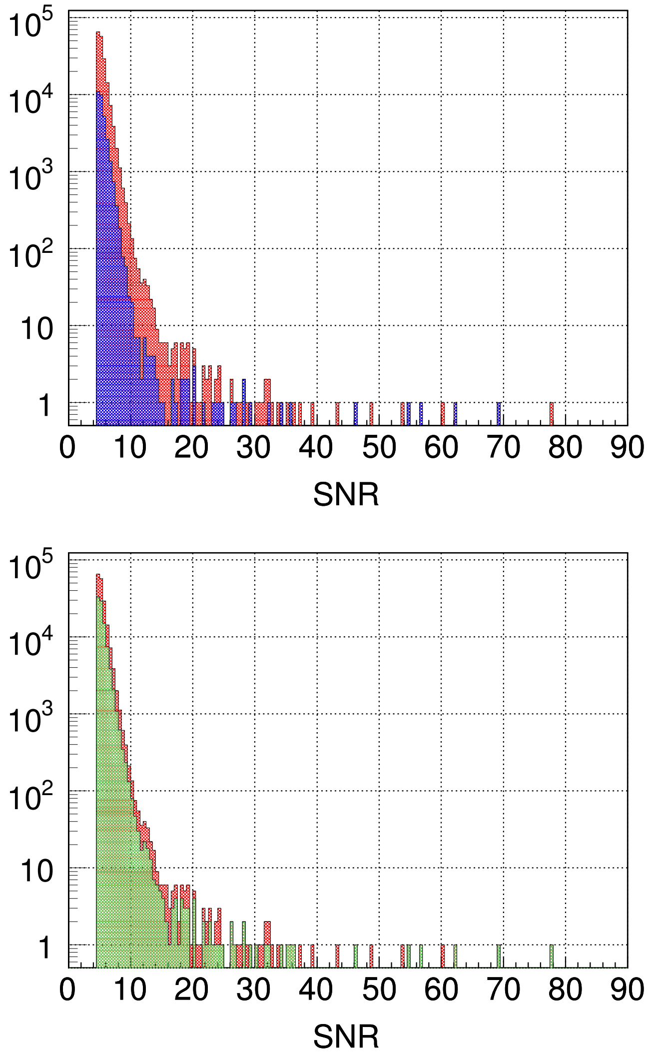

Figure 5.6: On the top: histogram of SNR distribution for all the triggers in the coincident run (182516 events, red histogram) and for triggers during the quadruple coincidence AURIGA-LHO1-LHO2-LLO (31533 events, blue histogram). On the bottom: histogram of SNR distribution for all the triggers in the coincident run (182516 events, red histogram) and for triggers during the triple coincidence AURIGA-LHO1-LHO2 not included in quadruple coincidence time segments (62074 events, green histogram).

observatories and a different time lag to the Livingston observatory. We defined a series of time shifted data sets (99 for quadruple coincidence and 93 for triple coincidences) as listed in tables 5.4 and 5.5. Each "off-source" data set was constructed as follows. Time-lags were both positive and negative: the code associated two positive lags to one third the sets, two negative lags to another third, and one positive and one negative lag to the remaining sets. The lags were randomly selected by the standard `c++` function `rand()` within the program which creates the lags (see the Handbook for the 1st LIGO-AURIGA analysis tools). The upper limit for the generated shift (100 s) was chosen to guarantee a sufficient stationarity on all the detectors involved. The lower limit (5 s) was chosen to avoid the intrinsic correlation of data. All time shifts were generated as integer multiples of 0.125 s. This choice, at the beginning, was driven by the need to debug a problem in the code. Once fixed the bug, the definition of time lags has not been changed. For each "off-source" set, we drew a new random number to set the Hanford time lag and took the previously generated one as the Livingston lag (see tables 5.4 and 5.5).

After defining the "off-source" data sets, a trigger selection was performed on each event of the AURIGA triggers list, released as a `root TTree` (see the root web page). The selection was performed by keeping all the triggers falling (before and after the shift) within the same segment of the LIGO time list. We took care to search a trigger in the same segment of the "on-source" data set because a different segment could be affected by a different noise statistics (for example the lock could be changed) and so could result in an event with different characteristics and not representative of the "on-source" events. However, selecting triggers falling in the same segment of the LIGO list (instead of in any possible segment) did not excluded a great number of triggers: the length of each time segment (both in LHO1-LHO2 and in LHO1-LHO2-LLO lists) was of the order of hundreds of seconds, while our shifts were of the order of some tens of seconds.

After the triggers selection, the output has been converted in an `ASCII` file consistent with the input of `CorrPower` and processed with this code. In particular, each event passed to `CorrPower` was centered at the trigger time of AURIGA, while its extremes were extended of its time uncertainty plus the light travel time[1]. The actual tuning of the analysis thresholds has been performed by looking at the first half of “off-source” data sets (see table 5.4). Then, all the available “off-source” data sets have been used to estimate the accidental coincidences (including those in table 5.5) to improve the statistical uncertainties.

5.3.1 Livetimes of the “off source” data sets

The livetimes of the not shifted data sets were simply given by the superposition of the time segments lists of the detectors involved in the analysis. In the case of quadruple coincidence we get 129699 s, while for the triple coincidence: 266544 s.

The equivalent observation time of each “off-source” data set has been computed as follows in order to comply with the trigger selection criterium presented in section 5.3. First, one considered the intersections of each time segment of the LIGO configuration at the true time with the same segment after applying the time shifts. Then, we intersected the resulting fragmented observation time of LIGO with the AURIGA livetime and we took the total duration. As a consequence, the trigger selection criterium adopted for the analysis implied that different “off-source” data sets had different livetimes. This has been performed both on the LHO1-LHO2 and on the LHO1-LHO2-LLO configurations.

The livetimes of all the “off-source” data sets (referring to 4-fold and 3-fold coincidences) are listed in tables 5.6 and 5.7.

The total livetime of the 99 “off-source” data sets in the case of quadruple coincidence is: 11965485 s.

The total livetime of the 93 “off-source” data sets in the case of triple coincidence is: 23743361 s. As previously said, in this analysis the time of quadruple and triple coincidences are disjoint since the 3-fold livetime refers to periods when LLO was off.

Since the duration of the several “off-source” data sets was fluctuating at most by $\sim \pm 7\%$, we approximated our model for the found number of accidental coincidences in each 4-fold set as a sample of the same Poisson random variable.

[1]in all cases, we have considered as “light travel time” the travel time between AURIGA and Hanford (i.e. 0.027 s).

Set name	H1	H2	L1	AUR
l50	89.1250	89.1250	28.0000	0
l51	7.3750	7.3750	89.1250	0
l52	29.7500	29.7500	7.3750	0
l53	91.8750	91.8750	29.7500	0
l54	34.6250	34.6250	91.8750	0
l55	85.1250	85.1250	34.6250	0
l56	51.7500	51.7500	85.1250	0
l57	65.6250	65.6250	51.7500	0
l58	33.0000	33.0000	65.6250	0
l59	77.3750	77.3750	33.0000	0
l60	79.2500	79.2500	77.3750	0
l61	49.8750	49.8750	79.2500	0
l62	66.1250	66.1250	49.8750	0
l63	28.7500	28.7500	66.1250	0
l64	30.5000	30.5000	28.7500	0
l65	83.8750	83.8750	30.5000	0
l66	69.8750	69.8750	83.8750	0
l67	-89.1250	-89.1250	-28.0000	0
l68	-7.3750	-7.3750	-89.1250	0
l69	-29.7500	-29.7500	-7.3750	0
l70	-91.8750	-91.8750	-29.7500	0
l71	-34.6250	-34.6250	-91.8750	0
l72	-85.1250	-85.1250	-34.6250	0
l73	-51.7500	-51.7500	-85.1250	0
l74	-65.6250	-65.6250	-51.7500	0
l75	-33.0000	-33.0000	-65.6250	0
l76	-77.3750	-77.3750	-33.0000	0
l77	-79.2500	-79.2500	-77.3750	0
l78	-49.8750	-49.8750	-79.2500	0
l79	-66.1250	-66.1250	-49.8750	0
l80	-28.7500	-28.7500	-66.1250	0
l81	-30.5000	-30.5000	-28.7500	0
l82	-83.8750	-83.8750	-30.5000	0
l83	-69.8750	-69.8750	-83.8750	0
l84	92.3750	92.3750	-69.8750	0
l85	-85.7500	-85.7500	92.3750	0
l86	97.1250	97.1250	-85.7500	0
l87	-8.1250	-8.1250	97.1250	0
l88	15.3750	15.3750	-8.1250	0
l89	-89.1250	-89.1250	15.3750	0
l90	80.6250	80.6250	-89.1250	0
l91	-53.7500	-53.7500	80.6250	0
l92	39.1250	39.1250	-53.7500	0
l93	-10.7500	-10.7500	39.1250	0
l94	77.5000	77.5000	-10.7500	0
l95	-28.6250	-28.6250	77.5000	0
l96	89.6250	89.6250	-28.6250	0
l97	-11.5000	-11.5000	89.6250	0
l98	95.3750	95.3750	-11.5000	0

Table 5.4: Definition of the time lags shifts $l50$-$l98$ (units of seconds).

Set name	H1	H2	L1	AUR
l1	72.5000	72.5000	88.8750	0
l2	35.7500	35.7500	72.5000	0
l3	78.6250	78.6250	35.7500	0
l4	33.1250	33.1250	78.6250	0
l5	83.2500	83.2500	33.1250	0
l6	15.5000	15.5000	83.2500	0
l7	90.6250	90.6250	15.5000	0
l8	41.8750	41.8750	90.6250	0
l9	64.3750	64.3750	41.8750	0
l10	70.0000	70.0000	64.3750	0
l11	15.1250	15.1250	70.0000	0
l12	17.2500	17.2500	15.1250	0
l13	5.7500	5.7500	17.2500	0
l14	31.3750	31.3750	5.7500	0
l15	67.7500	67.7500	31.3750	0
l16	34.6250	34.6250	67.7500	0
l17	25.5000	25.5000	34.6250	0
l18	-72.5000	-72.5000	-88.8750	0
l19	-35.7500	-35.7500	-72.5000	0
l20	-78.6250	-78.6250	-35.7500	0
l21	-33.1250	-33.1250	-78.6250	0
l22	-83.2500	-83.2500	-33.1250	0
l23	-15.5000	-15.5000	-83.2500	0
l24	-90.6250	-90.6250	-15.5000	0
l25	-41.8750	-41.8750	-90.6250	0
l26	-64.3750	-64.3750	-41.8750	0
l27	-70.0000	-70.0000	-64.3750	0
l28	-15.1250	-15.1250	-70.0000	0
l29	-17.2500	-17.2500	-15.1250	0
l30	-5.7500	-5.7500	-17.2500	0
l31	-31.3750	-31.3750	-5.7500	0
l32	-67.7500	-67.7500	-31.3750	0
l33	-34.6250	-34.6250	-67.7500	0
l34	-25.5000	-25.5000	-34.6250	0
l35	60.0000	60.0000	-25.5000	0
l36	-48.0000	-48.0000	60.0000	0
l37	37.5000	37.5000	-48.0000	0
l38	-27.7500	-27.7500	37.5000	0
l39	13.1250	13.1250	-27.7500	0
l40	-88.0000	-88.0000	13.1250	0
l41	52.3750	52.3750	-88.0000	0
l42	-54.8750	-54.8750	52.3750	0
l43	77.3750	77.3750	-54.8750	0
l44	-65.8750	-65.8750	77.3750	0
l45	18.0000	18.0000	-65.8750	0
l46	-62.3750	-62.3750	18.0000	0
l47	52.3750	52.3750	-62.3750	0
l48	-9.6250	-9.6250	52.3750	0
l49	72.0000	72.0000	-9.6250	0
l50	-65.6250	-65.6250	72.0000	0

Table 5.5: Definition of the time lags shifts $l1$-$l50$ (units of seconds).

Set name	Livetime (seconds)	Set name	Livetime (seconds)	Set name	Livetime (seconds)
0	129698.5	34	125722.4	68	119850.8
1	120081.3	35	120373.5	69	126270.9
2	121739.1	36	118054.7	70	119567.2
3	121109.0	37	120305.2	71	119567.2
4	121109.0	38	122445.4	72	120266.6
5	120646.3	39	125074.8	73	120266.6
6	120646.3	40	118645.2	74	122319.0
7	119904.9	41	114881.7	75	122319.0
8	119904.9	42	118112.8	76	121072.0
9	122591.7	43	115717.1	77	120875.2
10	121999.7	44	114660.5	78	120875.2
11	121999.7	45	120438.8	79	122265.1
12	127704.9	46	120802.9	80	122265.1
13	127704.9	47	117362.6	81	126186.8
14	126144.3	48	122831.7	82	120395.6
15	122234.8	49	120791.4	83	120395.6
16	122234.8	50	115185.3	84	112909.4
17	125790.0	51	120055.8	85	111452.1
18	119876.8	52	126321.4	86	111040.6
19	121584.6	53	119779.2	87	118432.1
20	120940.9	54	119779.2	88	126999.4
21	120940.9	55	120458.1	89	118307.3
22	120460.7	56	120458.1	90	112174.7
23	120460.7	57	122459.0	91	115522.2
24	119695.0	58	122459.0	92	119543.2
25	119695.0	59	121236.2	93	124121.1
26	122453.7	60	121045.7	94	120116.9
27	121850.4	61	121045.7	95	118284.0
28	121850.4	62	122405.8	96	117118.8
29	127679.1	63	122405.8	97	118830.3
30	127679.1	64	126239.5	98	118265.1
31	126088.1	65	120584.0	99	120055.8
32	122090.0	66	120584.0		
33	122090.0	67	119850.8	TOT=	11965485.2

Table 5.6: Livetimes of the "off-source" data sets referring to quadruple coincidences. The livetime of the not shifted data set is 129698.5 s, the total livetime (for the 99 "off-source" data sets) is: 11965485.2 s.

Set name	Livetime (seconds)
0	266544.3
1	251054.3
2	258757.5
3	249815.2
4	259321.0
5	248883.2
6	263110.9
7	247403.3
8	257453.7
9	252723.6
10	251565.3
11	263191.6
12	262735.1
13	265243.0
14	259696.3
15	252027.4
17	260954.8
18	250782.4
19	258648.6
20	249512.9
21	259222.0
22	248559.9
23	263070.9
24	247045.4
25	257311.0
26	252485.7
27	251306.8
28	263152.4
29	262689.5
30	265224.4
31	259604.3
32	251777.7

Set name	Livetime (seconds)
34	260889.2
35	253629.1
36	255979.8
37	258383.4
38	260396.7
39	263624.8
40	247582.7
42	254506.1
44	252170.3
45	262573.8
46	252907.5
47	255225.2
48	264355.6
49	251156.3
51	264883.8
52	260043.2
53	247151.8
54	258998.3
55	248504.8
56	255357.0
57	252464.0
58	259347.8
59	250068.5
60	249689.0
61	255750.0
62	252360.4
63	260256.4
64	259882.6
65	248757.0
66	251591.0
67	247352.7
68	264859.3

Set name	Livetime (seconds)
69	259959.2
70	246790.3
71	258893.4
72	248173.2
73	255173.8
74	252223.0
75	259249.6
76	249772.0
77	249383.0
78	255576.4
79	252117.5
80	260178.2
81	259795.3
82	248430.9
83	251332.8
84	247052.3
85	248044.9
86	246101.4
87	264689.4
88	263138.1
89	247352.7
90	249411.1
91	254746.4
92	258038.2
93	264108.5
94	250043.0
95	260205.3
96	247604.0
97	263944.7
98	246453.6
99	247704.6
TOT=	23743361

Table 5.7: Livetimes of the “off-source” data sets referring to triple coincidences. The livetime of the not shifted data set is 266544.3 s, the total livetime (for the 93 “off-source” data sets) is: 23743361 s.

Similarly, for the 3-fold sets the duration fluctuated at most by $\sim \pm 4\%$. The Poisson model will be tested in section 6.1.

To give an unbiased estimate of the expected accidental coincidences in the "on-source" data sets, we have to take into account their longer duration with respect to the "off-source" ones. This is easily accomplished by scaling the total number of found "off-source" accidental coincidences by the ratio between the duration of the not-shifted data set and the total duration of the"off-source" data sets:

$$b = \frac{T_{on}}{T_{off}} \cdot n \tag{5.5}$$

where b is the mean number of accidental coincidences expected in the "on-source" data set, T_{on} is the livetime of the "on-source" data set, T_{off} is the sum of all livetimes in "off-source" data sets and n is the total number of accidental coincidences found in the "off-source" data sets.

5.4 The LIGO coincidences

After the list of AURIGA triggers has been produced according to criteria described in section 5.2, and selected according to criteria described in section 5.3, a wide-band cross-correlation search has been performed on LIGO data around each trigger. The code used for this step of the analysis is `CorrPower` which implements the same analysis used for cross-correlation in the LIGO run S2 (LSC (2005)).

In this step of the analysis, the random variable called *r-statistic* is evaluated:

$$r = \frac{\sum_i (x_i - \overline{x})(y_i - \overline{y})}{\sqrt{\sum_i (x_i - \overline{x})^2}\sqrt{\sum_i (y_i - \overline{y})^2}} \tag{5.6}$$

which expresses the correlation between a pair of detectors which timeseries are x_i and y_i. In equation (5.6), index i spans an integration time window of 20, 50 or 100 ms[1]. Each of these time windows slided with 99% overlap around the AURIGA

[1]this time windows have been chosen to take into account several durations of the target signal.

trigger time; the closer end of each sliding window was kept within $\pm[27\,\mathrm{ms} + \sigma_t]$ from the AURIGA trigger time[1], where σ_t is the estimated 1σ timing error of the AURIGA trigger. Equation (5.6) gives 1 if x_i and y_i are perfectly correlated and -1 if perfectly anti-correlated (Cadonati (2004), see appendix A.1.1).

For each trigger and each j^{th} pair of interferometers, the variable Γ_j has been evaluated, being $10^{-\Gamma_j}$ the statistical significance of the null-hypothesis test for r. In this way, $10^{-\Gamma_j}$ expresses the probability to obtain the measured cross-correlation value if no correlation is present between the two interferometers in the pair j.

When more than one pair of interferometers was available (such as in the case of 4-fold coincidence AURIGA-LHO1-LHO2-LLO), the coherent statistic we took was the arithmetic mean (Γ) of all Γ_j.

The same procedure has been repeated for all the considered time windows and the maximum Γ was kept and used (together with the SNR) to characterize each trigger.

In our analysis we considered only the LIGO coincidences with $\Gamma \geq 4$. This value is to be intended as a minimal threshold for the subsequent analysis. The reasonable choice in case of perfectly Gaussian noise would have been $\Gamma \geq 3$ but the presence of broadband instrumental transients during the LIGO run S3 forced the collaboration to increase this threshold.

[1] 27 ms is approximatively the light travel time between AURIGA and the Hanford site.

Chapter 6

The joint data analysis AURIGA-LIGO

As explained in the previous chapter, the method implemented for the first AURIGA-LIGO joint analysis relies on the cross-correlation of data from the LIGO interferometers triggered by the AURIGA burst candidate events (Cadonati *et al.* (2005)). No *a-priori* hypothesis is made on the source direction of the signal; we just assume a detectable spectral power in the AURIGA bandwidth (850-950 Hz) to be above the AURIGA threshold. After the triggers exchange, LIGO performs a cross-correlation search between pairs of interferometers around each trigger time (as seen in section 5.4). Then, the final list of candidate events is characterized by several parameters (such as the statistical significance of the cross-correlation Γ[1], the estimated h_{rss} at each detector, etc...) which can still be used to further select the events and tune the analysis.

The two collaborations agreed to perform a *blind search* in order to avoid biases on the results. With *blind search* we mean an analysis not tuned on its results (as for an *exploratory search*). To satisfy this requirement, the Joint Working Group agreed to adopt a strategy consisting in three points:

i. a *playground* of $\sim 10\%$ of the total observation time is used to test the analysis pipeline and then excluded from the search (as seen in section 5.1.1);

[1] Γ corresponds to the arithmetic mean of three pairwise confidences for the no-correlation hypothesis in the LIGO detectors, see appendix A.

ii. the tuning of the analysis is performed on "off-source" data sets obtained by time shifting the LIGO data (as seen in section 5.3);

iii. once the analysis procedure and thresholds are frozen, "the box is opened" to search for gravitational wave bursts in the original data set.

In this chapter, tuning and results of the analysis are presented. The tuning consists mainly on the choice of two thresholds: one for SNR and one for Γ. In the final step of the analysis, only the events above the chosen thresholds will be taken into consideration. It is important to notice that these two values are very different physical quantities: SNR is the amplitude to noise ratio (measured by AURIGA) of the triggers, while Γ gives the significance of the null hypothesis test referring to the cross-correlation on LIGO data. The choice of the thresholds for these two quantities will be done as a compromise between a small false-alarm rate and large detection efficiency. The minimal thresholds considered here are $SNR = 4.5$ and $\Gamma = 4$. The estimation of false alarms will be presented in section 6.1, while the efficiency will be presented in section 6.2. The final choice of the thresholds and the results will be presented in sections 6.3 and 6.4, respectively.

6.1 Estimation of false alarms

As explained in section 5.3, "off-source" data sets have been formed by introducing un-physical delays between the LIGO interferometers. The number of time shifts considered is 99 for the 4-fold coincidence mode and 93 for the 3-fold coincidence mode. The total number of events over the exchange thresholds we get for our "off-source" coincidences is 422 in the case of 4-fold network and 234460 in the case of 3-fold.

In order to reduce this number we have applied a cut on the sign of the correlation between the two interferometers LHO1 and LHO2. Since they are co-located, these two detectors must be positively correlated with respect to any incoming gravitational wave. This test (which we will refer to in the following and in the captions as "LHO-sign cut") reduces to 203 events the "off-source" accidental coincidences for the 4-fold data set and to 119071 the same value for the 3-fold.

Another strategy to suppress the number of accidental coincidences is to require the consistency of the estimated h_{rss} in the co-located LHO1 and LHO2. Tests have shown that this cut is effective at suppressing about half the false alarms. However, at the time of this analysis, the h_{rss} estimation code was not mature for implementation.

On figure 6.1 the Γ distribution is shown for all the events before and after applying the LHO-sign cut. In figure 6.2 the scatter plots of Γ versus SNR are shown for the same events.

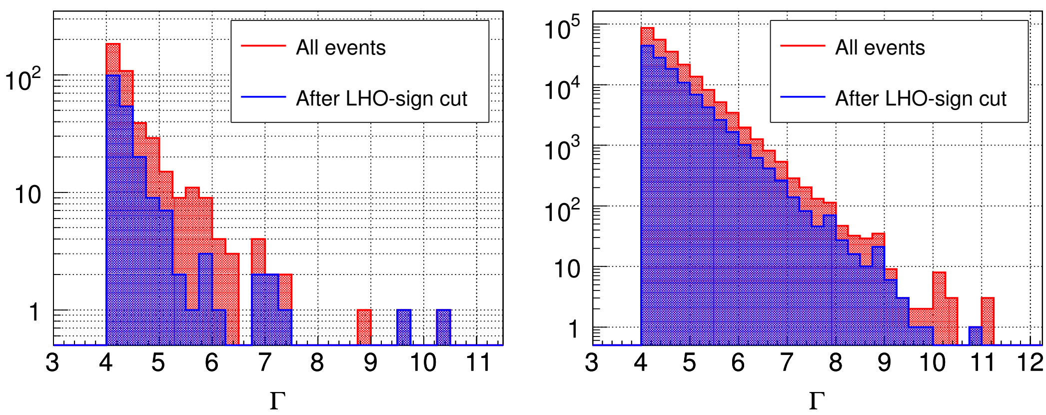

Figure 6.1: Histogram of Γ distribution for all the events (black curve) and after the LHO-sign cut (blue curve). Left: network in quadruple coincidence. Right: network in triple coincidence. Only events above the exchange thresholds are shown.

In order to choose the suitable thresholds for this analysis, it is important to study how the false alarm rate depends on the values of SNR and Γ. Figure 6.3 shows the number of false alarms expected in the "on-source" data set (after the LHO-sign cut) according to the false alarms obtained from the "off-source" data sets. Levels have been drawn by normalizing the number of "off-source" accidental coincidences with the ratio between the livetimes of the "on-source" and "off-source" data sets (as in equation 5.5).

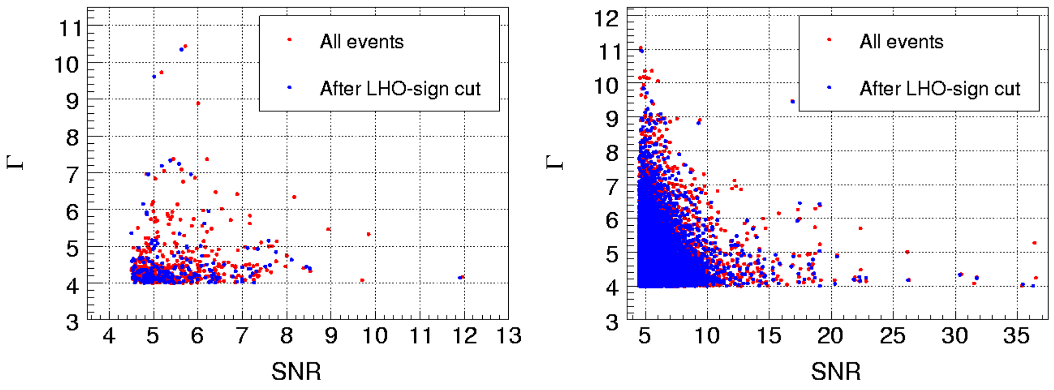

Figure 6.2: Scatter plot of Γ vs SNR of the accidental events: for all the events (black dots) and after the LHO-sign cut (blue dots). Left: network in quadruple coincidence; right: network in triple coincidence. Only events above the exchange thresholds are shown.

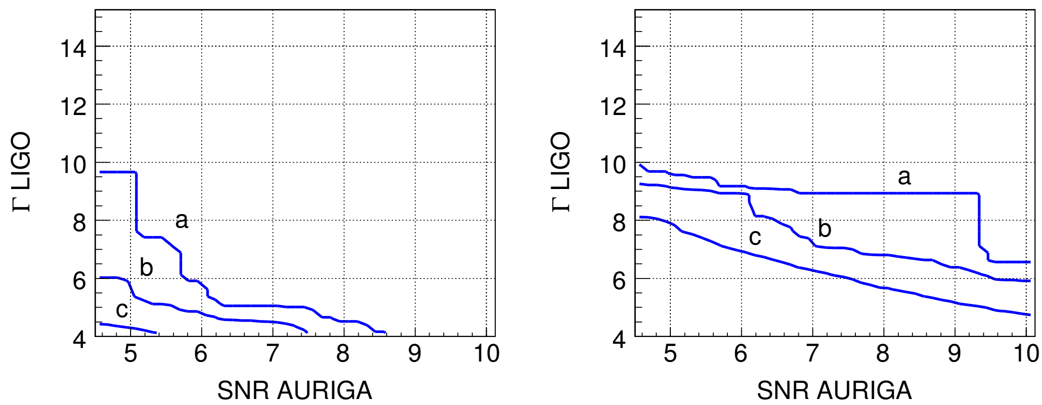

Figure 6.3: Number of accidental coincidences expected for the “on-source” data sets by studying the “off-source” data sets after the LHO-sign cut. Plot on the left is obtained from the 99 “off-source” quadruple coincidence data sets. Plot on the right refers to triple coincidences and has been obtained from the 93 “off-source” triple coincidence data sets. For both the pictures, contour lines are drawn to indicate the thresholds corresponding to: (a) 0.02 events, (b) 0.1 events and (c) 1 event.

In order to predict the number of false alarms (and its error) in the "on-source" data set, it is important to know the statistical distribution of the "off-source" accidental coincidences, which should be Poisson distributed.

Under the ergodic hypothesis, each shifted data set has the same statistical properties of the not shifted one. For this reason we consider each data set as an independent trial of the same counting experiment. Independence is guaranteed by the fact that time shifts are greater than the auto-correlation time of the events. The number n of accidental coincidences in each data set is expected to follow a Poisson distribution:

$$P_\mu(n) = e^{-\mu}\frac{\mu^n}{n!} \tag{6.1}$$

where μ is the mean number of accidental coincidences in each set.

Actually, each "off-source" data set has a slightly different length (as seen in tables 5.6-5.7) and, in principle, should not be considered as a trial of the same experiment. A possible solution is normalizing the number of coincidences on the effective time of each set. However, in this way, the distribution is no longer Poisson because the output of each trial is not integer. For this reason, since the livetime differences are small (see section 5.3.1 and tables within), we have chosen a simplified approach and we have neglected them.

A test has been performed on the "off-source" data sets to check the overall distribution of Γ. We expect a distribution fitting with the Poisson curve in equation 6.1 multiplied by the number of considered data sets (i.e. 99 for quadruple coincidence and 93 for triple coincidence).

In figure 6.4 the distribution of Γ for the number of accidental events (above the minimal threshold $\Gamma \geq 4$) is shown for quadruple and triple coincidence "off-source" data sets (red histogram). We have superimposed, to the first histogram, the expected Poisson values while, to the second, (because of the great number of events) the expected Gaussian values (gray markers). These theoretical curves have been constructed using the means we get from the "off-source" data sets ($\mu = 2.05$ for quadruple coincidences and $\mu = 1280.33$ for triple coincidences) and the corresponding number of sets to normalize (99 for quadruple coincidences and 93 for triple coincidences). For each bin, a gray bar indicates the expected error according to the Poisson (or Gaussian) distribution (i.e. the square root of the number of counts).

For both quadruple and triple coincidences, we have evaluated the χ^2 between the real distributions and the models. The number of counts of each bin in the "off-source" distribution has been compared to the expected one in the theoretical curve. Only bins with more than 5 counts in the expected Poisson distribution have been taken into account to evaluate the χ^2. For the quadruple coincidences, the χ^2 (with 3 degree of freedom) resulted 0.82 with a p-value[1] of 84.4%. For the triple coincidences, the χ^2 (with 3 degree of freedom) resulted 4.07 with a p-value of 25.3%. In both cases we conclude that the Poisson model is accepted.

However, we must consider that the "on-source" data sets have to be analyzed after applying some thresholds (referred to, in the following, as "analysis thresholds"). For this reason it is important to check the Γ distribution close to those thresholds. However, because of the small number of "off-source" data sets, our Γ distribution for the quadruple coincidences results poorly populated. At higher thresholds the number of bins with integral ≥ 5 becomes too small to consent a χ^2 test. For this reason, we performed the check with higher thresholds only on the triple coincidences data sets (see figure 6.5). In this case, the highest threshold we can choose is $\Gamma > 7.5$. For this value we get a χ^2 (evaluated with the same criteria described above) equal to 1.83 for 3 degree of freedom, with a p-value of 61%. Also in this case we conclude that the Poisson model is accepted.

6.2 Detection efficiency of the network

The estimation of the pipeline's efficiency and the code validation have been performed with the standard mechanism developed and used by the LSC: the so-called *"Mock-Data Challenges"* (MDCs), which consists of software-generated signals superimposed to real data (Yakushin, Klimenko & Rakhmanov (2004)).

[1]The p-value is the probability, if the test statistic really was distributed as it would be under the null hypothesis, of observing a test statistic (as extreme as, or more extreme than) the one actually observed. In this case the null hypothesis is the assumption of samples Poisson distributed.

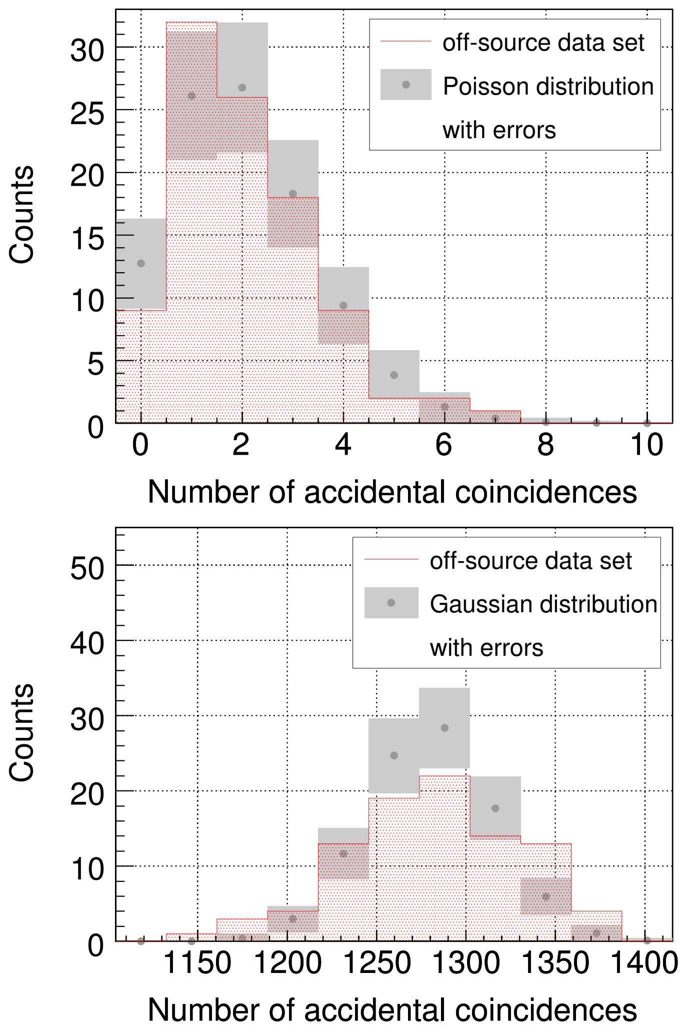

Figure 6.4: Distribution of the number of accidental coincidences with $\Gamma \geq 4$ and passing the "LHO-sign cut" for the "off-source" data sets (red histograms). On the top: quadruple coincidences. On the bottom triple coincidences. Each distribution is compared to its model: a Poisson distribution with $\mu = 2.05$ and normalization factor $= 99$ for quadruple coincidences and a Gaussian distribution with mean $= 1280.33$ and normalization factor $= 93$ for triple coincidences (in gray): for each bin a gray marker and bar indicate the expected number of coincidences and its error (evaluated as the square root of the counts).

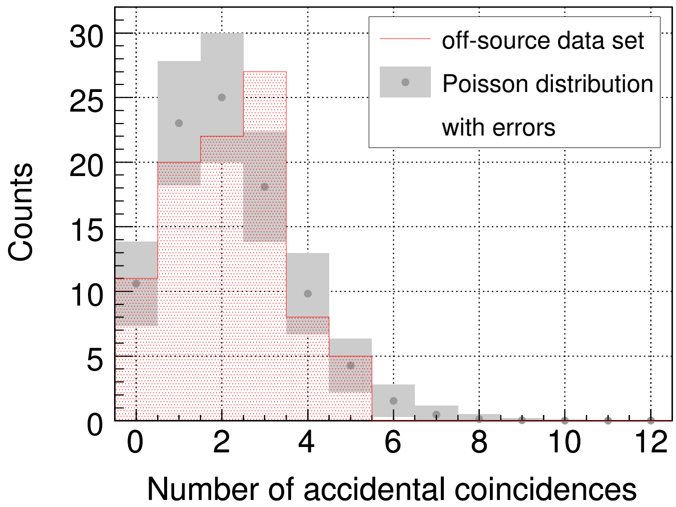

Figure 6.5: Distribution of the number of accidental coincidences with $\Gamma \geq 7.5$ and passing the "LHO-sign cut" for the "off-source" triple coincidence data sets (red histogram). The distribution is compared to its model: a Poisson distribution with $\mu = 2.17$ and normalization factor $= 93$ (in gray): for each bin a gray marker and bar indicate the expected number of coincidences and its error (evaluated as the square root of the counts).

The signals added in these time series are characterized by known statistical properties and can be used to test the data analysis pipeline (as was be done in LSC (2004) and LSC (2005)). The classes of signals considered for this analysis are:

- LA_SG2: Gaussians, sine-Gaussians and cosine-Gaussians (see sec. B.1)
- LA_DS2: damped sinusoids (see sec. B.2)

Both sets of MDC frames have been produced in a two-step process.

First, a set of signal parameters (see table 6.1) are generated and stored into an `ASCII` file. In particular, the source locations for the signals are simulated as isotropically distributed over the sky: ϕ is uniform over $[0, 2\pi]$, $\cos\theta$ is uniform over $[-1, 1]$ and the polarization angle ψ is distributed randomly on $[0, \pi]$ (for more details, see table 6.1).

Frame production is performed by the LIGO software `LDAS` (see the LDAS web page) by reading the parameters log file and writing a time series consisting mostly of zeroes plus the injected waveforms (other informations are needed in this step, such as the detectors calibration file and their sampling rates). All the standard MDC production implemented by LIGO needed adaptations to the AURIGA detector and this made necessary the tests described in Sutton (2005). The `Matlab` scripts used for the check, the `tcl` scripts and the log files used for the MDC production are publicly available in the MDC Matlab and tcl scripts repository.

As explained in appendix B, all the considered waveforms (both of LA_SG2 and LA_DS2 class) have an "intrinsic" amplitude $A = 7.5 \times 10^{-21}/\sqrt{\text{Hz}}$. However, the signal waveforms have been injected in the MDC frames after scaling them by a set of scale factors, chosen in such way to cover a wide range of signal amplitudes. After the injection, we have studied the response of the network to the different simulated amplitudes of signal. For the 2 classes of signals, the considered scale factors are:

LA_SG2 scale factors $s =$ `0.0625 0.125 0.25 0.5 1 2 4 8 16 32 64 128 256 512 1024 2048 4096`

LA_DS2 scale factors $s =$ `0.25 0.5 1 2 4 8 16 32 64 128 256 512 1024 2048`

Signals of the LA_SG2 class, injected with intrinsic amplitude $h_{rss} = A = s \cdot 7.5 \times 10^{-21}/\sqrt{\text{Hz}}$, will be seen at Earth (from the optimal orientation) with that amplitude. Instead, for signals of the LA_DS2 class (see equation B.6) we must average over the inclination angle ι: $h_{rss} = \sqrt{2}s \cdot 7.5 \times 10^{-21}/\sqrt{\text{Hz}}$.

We estimate the detection efficiency and its error using the binomial distribution statistics:

$$
\begin{aligned}
\varepsilon(h_{rss}) &= N_{det}(h_{rss})/N_0 \\
\sigma(h_{rss}) &= \sqrt{\varepsilon(h_{rss})(1-\varepsilon(h_{rss}))/N_0}
\end{aligned}
\tag{6.2}
$$

where N_0 is the number of injected waveforms and N_{det} is the number of the detected ones. The set of points $(h_{rss}, \varepsilon(h_{rss}))$ can be fitted using empirical sigmoid curve:

$$
\varepsilon(h_{rss}) = p_3 \left[1 + (h_{rss}/p_1)^{p_0(1+p_2 \tanh(h_{rss}/p_1))}\right]^{-1} \tag{6.3}
$$

where:

$p_0 =$ parameter describing the steepness of the efficiency curve;

1	integer part of GPS signal time (s)
2	decimal part of GPS signal time at LHO (ns, rounded)
3	decimal part of GPS signal time at LLO (ns, rounded)
4	decimal part of GPS signal time at GEO (ns, rounded)
5	decimal part of GPS signal time at TAMA (ns, rounded)
6	decimal part of GPS signal time at AURIGA (ns, rounded)
7	(signal time at LLO) - (signal time at LHO) (ns, rounded)
8	(signal time at GEO) - (signal time at LHO) (ns, rounded)
9	(signal time at TAMA) - (signal time at LHO) (ns, rounded)
10	(signal time at AURIGA) - (signal time at LHO) (ns, rounded)
11	antenna response factor F_+ for LHO
12	antenna response factor $F_\times$ for LHO
13	antenna response factor F_+ for LLO
14	antenna response factor $F_\times$ for LLO
15	antenna response factor F_+ for GEO
16	antenna response factor $F_\times$ for GEO
17	antenna response factor F_+ for TAMA
18	antenna response factor $F_\times$ for TAMA
19	antenna response factor F_+ for AURIGA
20	antenna response factor $F_\times$ for AURIGA
21	azimuthal sky coordinate ϕ of source (rad)
22	polar sky coordinate θ of source (rad)
23	polarization angle ψ of signal (rad)
24	name of the waveform type
25	RSS sky amplitude of the plus polarization ($1/\sqrt{Hz}$)
26	RSS sky amplitude of the cross polarization ($1/\sqrt{Hz}$)

Table 6.1: List of parameters characterizing the injected signals of each set of MDC frames (LA_SG2 and LA_DS2). In this list, the "GPS signal time" is the start time if the injection (the signal peaks approximately after 0.5 s). The "polar sky coordinate" is expressed respect to Earth-based coordinates (the x-axis points from the Earth's center to the intersection of the Greenwich meridian with the equator, the z-axis points from the Earth's center to the North pole, while the y-axis is chosen to form a right-handed coordinate system with the other two). The "polarization angle" is the angle counterclockwise about the signal direction of propagation from the line of constant θ (pointing to decreasing ϕ) to the x-axis of the source coordinate system (the direction associated with the + polarization). Of course, inputs referring to TAMA and GEO detectors have not been used in this analysis.

p_1 = scale factor, close to the point with 50% detection efficiency (which we will call, in the following, $h_{rss}50\%$);
p_2 = asymmetry parameter: it is 0.5 for the detection efficiency of optimally oriented signals, but diverges from this value for sources that are uniformly distributed in the sky;
p_3 = asymptotic detection efficiency for loud signals (1 in our curves).

Equation 6.3 proved to be representative of the real data in the case of LIGO-only analysis but in the case of AURIGA, we introduce an offset parameter p_4 to take into account the not negligible number of false alarms at the threshold of $SNR \geq 4.5$. In fact, also in the case of very low h_{rss} injections, it could happen to find an event which, by chance, occurs at the injection time of the signal. For this reason, equation 6.3 becomes:

$$\varepsilon(h_{rss}) = p_4 + p_3 \left[1 + (h_{rss}/p_1)^{p_0(1+p_2 \tanh{(h_{rss}/p_1)})}\right]^{-1} \tag{6.4}$$

Once introduced the parameter p_4 the AURIGA-only efficiency to the injections fits perfectly with the curve in equation 6.4. A check has been performed (see figure 6.6) to test the consistency of the MDC-injections method on the AURIGA data and the built-in Monte Carlo method normally used by the AURIGA collaboration. The check confirmed the consistency of the two methods, apart from a small discrepancy due to the fact that, while the AURIGA Monte Carlo has been performed on all the exchanged data set (211 h), the MDC injections (in this case sine-Gaussians) were applied to a subset of 12 h.

To get an efficiency estimate both for the 4-fold and the 3-fold mode, each class of MDC signals has been injected both in the LIGO and in the AURIGA pipelines on their calibrated data sets. The number of events considered for each class is listed in tables 6.2 and 6.3). In the same tables, the results for the efficiency are given, with respect to the minimal thresholds $SNR \geq 4.5$ and $\Gamma \geq 4$, in terms of $h_{rss}50\%$ (i.e. the h_{rss} value corresponding to a 50% detection efficiency). In the applied pipeline, the same cuts used for the analysis have been applied.

Figure 6.7 shows the efficiency curves (obtained from real points by fitting with the function in equation 6.4).

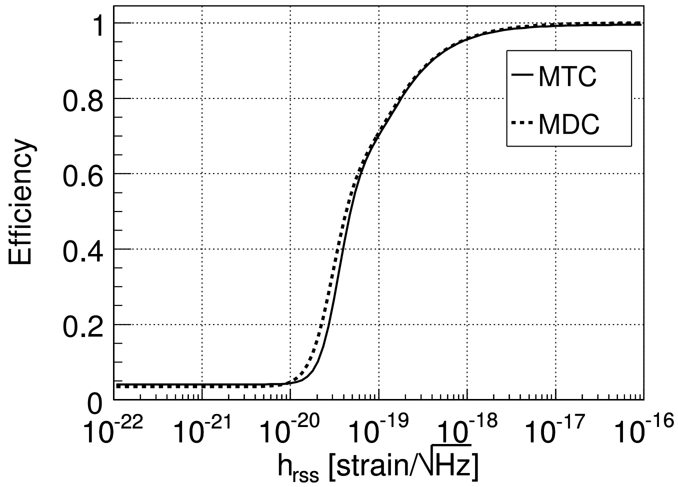

Figure 6.6: Efficiency versus h_{rss} as evaluated in AURIGA detector using built-in Monte Carlo over all AURIGA exchanged data set (with a 25 Hz injection rate) and using MDC injections. In both cases the injected signal is a sine-Gaussian centered at 900 Hz and with $Q = 9$ uniformly distributed in the sky. The polarization is linear with an arbitrary polarization angle. MDC injections regarded only the quadruple coincidences livetime with an injection rate of 1/64 Hz.

Waveform	Num of injections	h_{rss}50%	h_{rss}90%
Sine-Gaussians	1348	$5.3\times10^{-20}/\sqrt{Hz}$	$4.7\times10^{-19}/\sqrt{Hz}$
Gaussians	698	$15\times10^{-20}/\sqrt{Hz}$	$10\times10^{-19}/\sqrt{Hz}$
Damped sinusoids	2045	$5.5\times10^{-20}/\sqrt{Hz}$	$3.2\times10^{-19}/\sqrt{Hz}$

Table 6.2: List of the injections and efficiencies referring to the network in 4-fold coincidence mode and to the minimal thresholds ($SNR \geq 4.5$ and $\Gamma \geq 4$). The search has been completed with the check on the sign correlation between LHO1 and LHO2. On the first column the waveform. On the second the number of injections. On the third and fourth column the value of h_{rss}50% (the value of h_{rss} which gives an efficiency of 50%) and h_{rss}90% (the value of h_{rss} which gives an efficiency of 90%) obtained by fitting the esperimental point (see also figure 6.7).

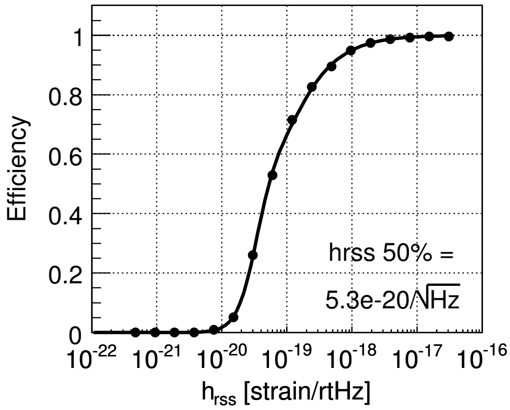

a) sine/cosine-Gaussians

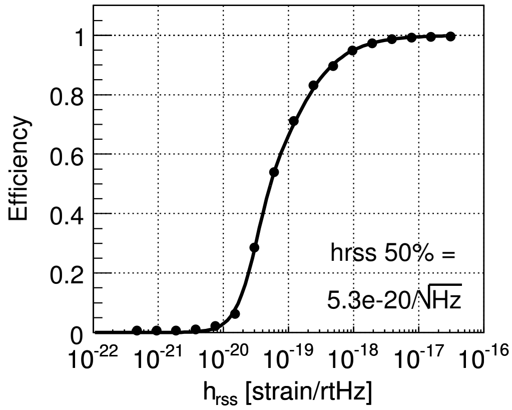

d) sine/cosine-Gaussians

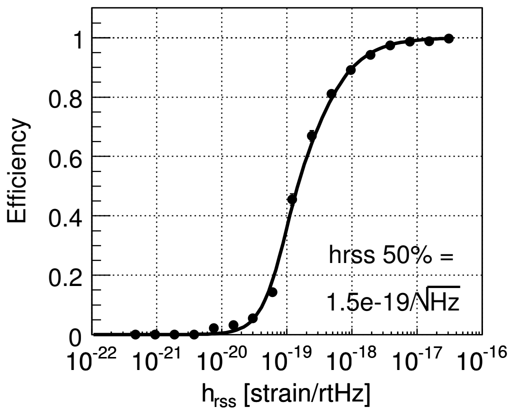

b) Gaussians

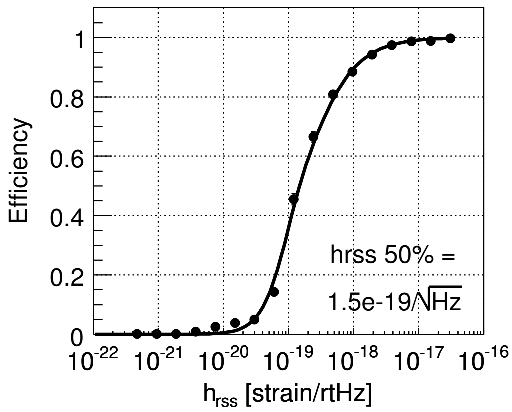

e) Gaussians

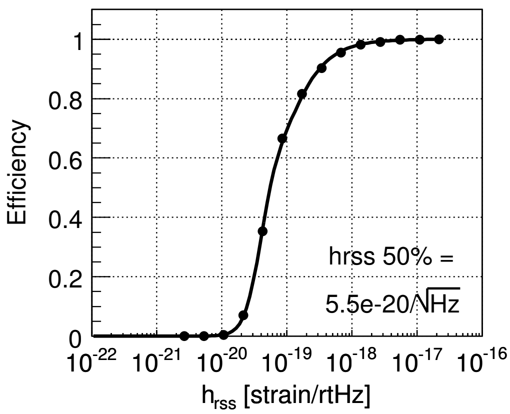

c) Damped sinusoids

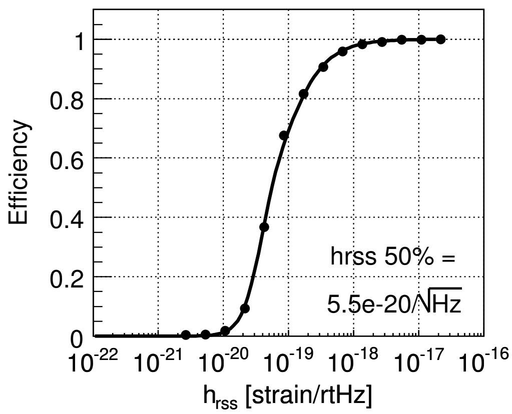

f) Damped sinusoids

Figure 6.7: Detection efficiency vs h_{rss} of injection for the network in 4-fold (left) and 3-fold (right) coincidence mode and for different waveforms. Here, the analysis pipeline includes the cut on the sign of correlation between LHO1 and LHO2. The thresholds considered are $SNR \geq 4.5$ and $\Gamma \geq 4$. The experimental points have been fitted with the curve described by equation 6.4. The value of $h_{rss}50\%$ is indicated for each fitting curve.

Waveform	Num of injections	$h_{rss}50\%$	$h_{rss}90\%$
Sine-Gaussians	1348	$5.3\times10^{-20}/\sqrt{Hz}$	$4.7\times10^{-19}/\sqrt{Hz}$
Gaussians	698	$15\times10^{-20}/\sqrt{Hz}$	$10\times10^{-19}/\sqrt{Hz}$
Damped sinusoids	2045	$5.5\times10^{-20}/\sqrt{Hz}$	$3.1\times10^{-19}/\sqrt{Hz}$

Table 6.3: List of the injections and efficiencies referring to the network in 3-fold coincidence mode and to the minimal thresholds ($SNR \geq 4.5$ and $\Gamma \geq 4$). The search has been completed with the check on the sign correlation between LHO1 and LHO2. On the first column the waveform. On the second the number of injections. On the third and fourth column the value of $h_{rss}50\%$ (the value of h_{rss} which gives an efficiency of 50%) and $h_{rss}90\%$ (the value of h_{rss} which gives an efficiency of 90%) obtained by fitting the esperimental point (see also figure 6.7).

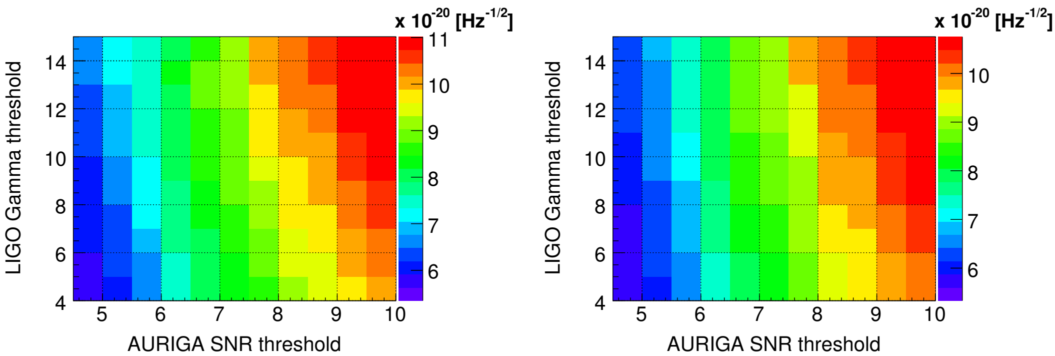

Figure 6.8: Efficiency to sine/cosine-Gaussians centered at a frequency of 900 Hz and with $Q \approx 3$. On the x axis the value of SNR from the exchange threshold to $SNR = 10$. On the y axis the value of Γ from the exchange threshold to $\Gamma = 15$. The colour scale indicate the value of $h_{rss}50\%$ for the network at the corresponding thresholds (efficiency is lower where $h_{rss}50\%$ is higher). Both the 4-fold (left) and 3-fold (right) coincidences have been considered.

6.3 Tuning

The plan for the last step of the analysis has been agreed by the AURIGA and LIGO collaborations before "opening the box" of final results, in order to keep blind the analysis. It has been agreed to perform the analysis on the entire observation time by merging the two data sets of 4-fold and 3-fold coincidences. According to this intent, thresholds on Γ and SNR have been chosen to render the 2 data sets (after the LHO-sign cut) very similar in terms of the rate of accidental coincidences. For our case also the efficiency to selected waveforms results very close. The agreed plan for the statistical treatment of the results is presented in section 6.3.2.

6.3.1 Analysis thresholds

Figure 6.9 is a superposition of the efficiency plots of figure 6.8 and the false alarm contour lines obtained in section 6.1. In correspondence of each $\Gamma - SNR$ pair it is possible to compare the value of $h_{rss}50\%$ for the network and the number of accidental coincidences expected in the not shifted data set. We have tuned the thresholds (from the exchange values $\Gamma = 4$ and $SNR = 4.5$) by paying the least on the detection efficiency while lowering the number of accidental coincidences down to the desired level. As one can see from figure 6.9, the optimal way of doing this is moving the thresholds towards higher Γ without changing the value of SNR. We have chosen the thresholds: $\Gamma \geq 6$ and $SNR \geq 4.5$ for quadruple coincidences and $\Gamma \geq 9$ and $SNR \geq 4.5$ for triple coincidences.

If we apply these thresholds to the 99 quadruple coincidences "off-source" data sets we get 8 events surviving the LHO-sign cut in $\approx$ 3323.7 hours. The false alarm rate (in events per day) and the total events expected in "on-source" data set are:

$$\begin{aligned} rate_{4-fold} &= 0.058 \pm 0.021 \;\; events/day \\ &= 0.09 \pm 0.03 \;\; events\, in\, the\, \text{“}on - source'' \,data\, set \end{aligned} \tag{6.5}$$

where the uncertainty is the 1σ error of the Poisson distribution of the counts.

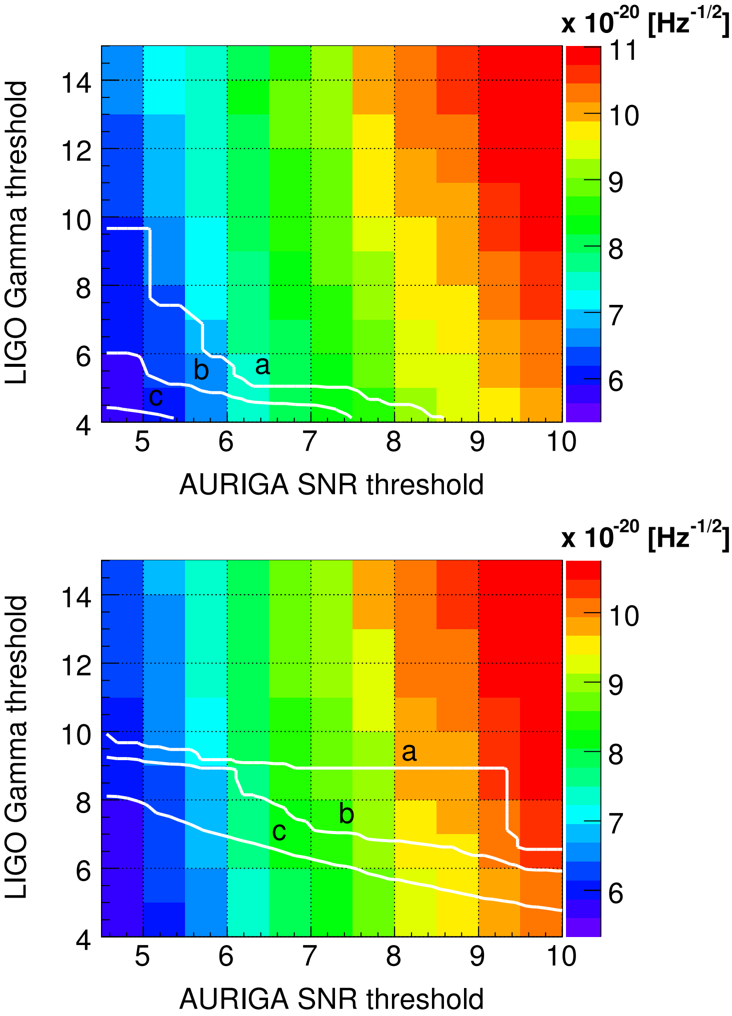

Figure 6.9: On the top color scale plot: efficiency to sine-Gaussians waveforms and false alarms for the 4-fold network. On the bottom color scale plot: the same but referring to the 3-fold network. Sensitivity is given in terms of h_{rss} at 50% efficiency. For both plots, contour lines refer to the accidental coincidences expected in the not shifted data set: (a) 0.02 events, (b) 0.1 events and (c) 1 event.

If we set to $\Gamma \geq 9$ and $SNR \geq 4.5$ the thresholds on the triple coincidence events, from the 93 "off-source" data sets we get 12 events surviving the LHO-sign cut in ≈ 6595.4 hours. The false alarm rate (in events per day) and the total events expected in "on-source" data set are:

$$\begin{aligned} rate_{3-fold} &= 0.044 \pm 0.013 \quad events/day \\ &= 0.13 \pm 0.04 \quad events\, in\, the\, \text{``}on - source'' \, data\, set \end{aligned} \tag{6.6}$$

where the uncertainty is the 1σ error of the Poisson distribution of the counts.

From equations 6.5 and 6.6 and from figure 6.9 we can notice that, after the tuning, both the 4-fold and the 3-fold networks predict about 0.1 events in the "on-source" data set.

For the selected thresholds, the efficiency in figure 6.9 has been evaluated with respect to the sine and cosine-Gaussians waveform. In figure 6.10, the efficiency (for quadruple and for triple coincidences) has been plotted for all the considered templates (sine-Gaussians, Gaussians and damped sinusoids) with respect to the h_{rss} of the injection. From figure 6.10, the values of the $h_{rss}50\%$ have been extrapolated and listed in tables 6.4 and 6.5. From the tabulated values, it is possible to notice the very similar efficiencies of the 4-fold and 3-fold data set at the chosen thresholds.

Waveform	Num of injections	$h_{rss}50\%$	$h_{rss}90\%$
Sine-Gaussians	1348	$5.6{\times}10^{-20}/\sqrt{Hz}$	$4.9{\times}10^{-19}/\sqrt{Hz}$
Gaussians	698	$15{\times}10^{-20}/\sqrt{Hz}$	$10{\times}10^{-19}/\sqrt{Hz}$
Damped sinusoids	2045	$5.7{\times}10^{-20}/\sqrt{Hz}$	$3.3{\times}10^{-19}/\sqrt{Hz}$

Table 6.4: List of the injections and efficiencies referring to the network in 4-fold coincidence mode after the LHO-sign cut and to the thresholds $SNR \geq 4.5$ and $\Gamma \geq 6$. On the first column the waveform. On the second, the number of injections. On the third and fourth column, the values of $h_{rss}50\%$ and $h_{rss}90\%$ obtained by fitting the experimental points (see also figure 6.10).

We combine the 4-fold and 3-fold data sets at the tuned threshold to form a single data set. We take, as a number of accidental coincidences in the combined

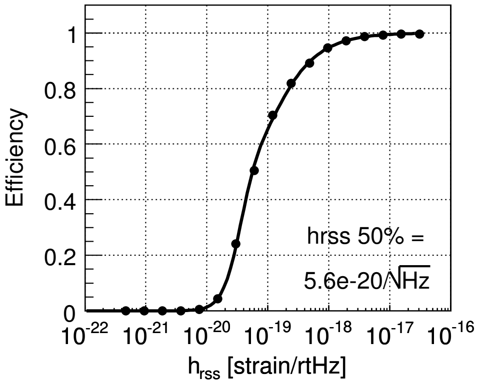

a) sine/cosine-Gaussians

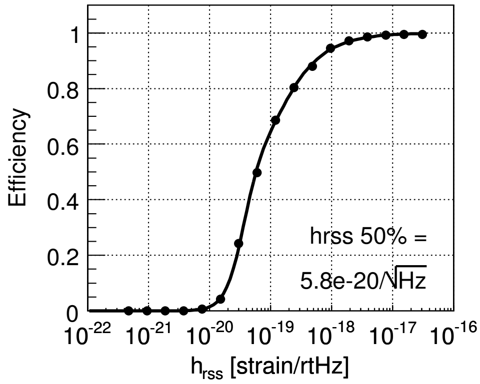

d) sine/cosine-Gaussians

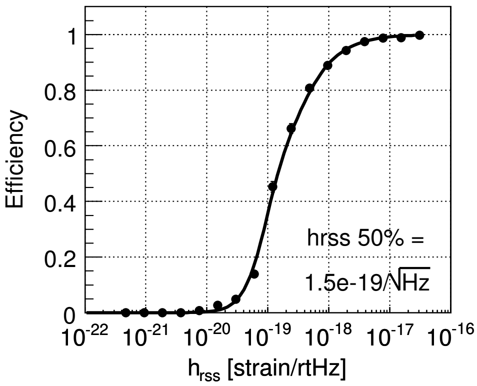

b) Gaussians

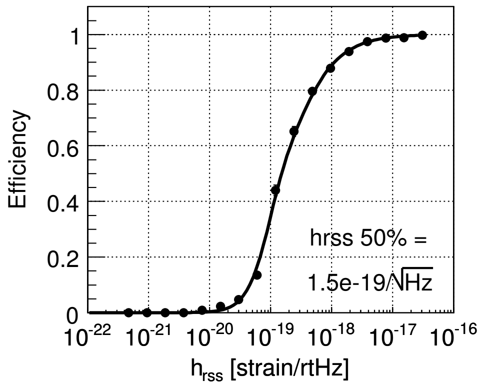

e) Gaussians

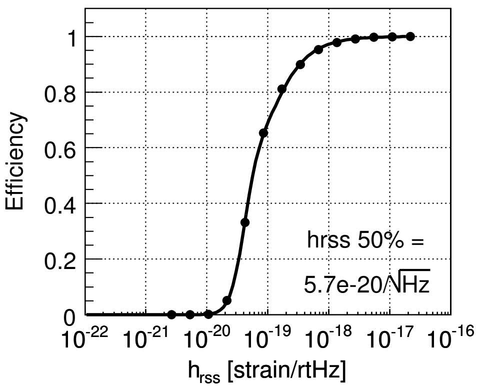

c) Damped sinusoids

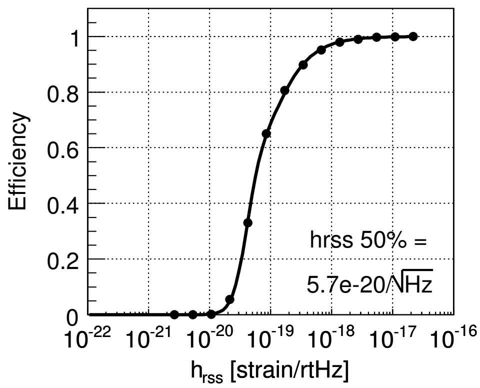

f) Damped sinusoids

Figure 6.10: Efficiency of detection vs h_{rss} of injection for the network in 4-fold (left) and 3-fold (right) coincidence mode and for different waveforms. Here, the analysis pipeline includes the cut on the sign of correlation between LHO1 and LHO2. The thresholds considered are $SNR \geq 4.5$ and $\Gamma \geq 6$ for the 4-fold coincidence and $SNR \geq 4.5$ and $\Gamma \geq 9$ for the 3-fold. The experimental points have been fitted with the curve described by equation 6.4. The value of $h_{rss}50\%$ is indicated for each fitting curve.

Waveform	Num of injections	$h_{rss}50\%$	$h_{rss}90\%$
Sine-Gaussians	1348	$5.8\times10^{-20}/\sqrt{Hz}$	$5.3\times10^{-19}/\sqrt{Hz}$
Gaussians	698	$15\times10^{-20}/\sqrt{Hz}$	$11\times10^{-19}/\sqrt{Hz}$
Damped sinusoids	2045	$5.7\times10^{-20}/\sqrt{Hz}$	$3.4\times10^{-19}/\sqrt{Hz}$

Table 6.5: List of the injections and efficiencies referring to the network in 3-fold coincidence mode and to the thresholds $SNR \geq 4.5$ and $\Gamma \geq 9$. The search has been completed with the check on the sign correlation between LHO1 and LHO2. On the first column the waveform. On the second, the number of injections. On the third and fourth column, the values of $h_{rss}50\%$ and $h_{rss}90\%$ obtained by fitting the experimental points (see also figure 6.10).

data set, the sum of the "off-source" coincidences in quadruple and triple coincidence sets $(8+12)$. The full observation time is $3323.7+6595.4$ hours. The rate and the number of events expected in the "on-source" data set are:

$$\begin{aligned} rate_{4+3-fold} &= 0.048 \pm 0.011 \quad events/day \\ &= 0.22 \pm 0.05 \quad events\, in\, the \text{ ``}on - source'' \, data\, set \end{aligned} \tag{6.7}$$

The efficiency of the combined data set can be approximated with an average between the efficiencies of the 4-fold and 3-fold data sets. This average must be weighted for the observation times according to:

$$\varepsilon(h_{rss})_{4+3-fold} = \frac{\varepsilon(h_{rss})_{4-fold} \cdot T_{4-fold} + \varepsilon(h_{rss})_{3-fold} \cdot T_{3-fold}}{T_{4-fold} + T_{3-fold}} \tag{6.8}$$

where T_{4-fold} and T_{3-fold} are the livetimes of the "on-source" quadruple and triple coincidence data sets and $\varepsilon(h_{rss})_{4-fold}$ and $\varepsilon(h_{rss})_{3-fold}$ are their efficiency curves.

6.3.2 Plan for the statistical analysis

The final step of the analysis consists in the statistical treatment of the results of this counting experiment aiming at testing the compliance of the null hypothesis and to set confidence intervals with selected coverage. According to the null hypothesis, the actual number of events we will find in the "on-source" data set has to be compliant with estimated distribution of the accidental coincidences. With only one trial planned, we have chosen 99% as a threshold on the confidence.

Given the expected accidental coincidences, the null hypothesis is rejected if at least 3 coincidences will be found.

Rejecting the null hypothesis does not imply a claim on gravitational wave detection but, instead, a claim for an excess correlation in the observatory at the true time, which has not been measured by looking at the accidental coincidences in our "off-source" data sets. It might be due to: correlated noise in the detectors, deviations from the Poisson noise model or gravitational waves.

We have agreed to set the confidence intervals according to Feldman and Cousins (Feldman & Cousins (1998)) with at least a 95% coverage. The uncertainties on the estimate of the accidental coincidences will be taken into account in the confidence belt construction, by considering an uncertainty of the mean accidental counts b of $\pm 3\sigma$. The standard Feldman and Cousins construction has been modified according to our null hypothesis test. If the null hypothesis is confirmed at 99% coverage, we will consider the upper bound of the Feldman and Cousins construction at 95% coverage but we will extend its lower bound to 0; otherwise, in the critical region of the null hypothesis test we will keep the original confidence intervals. As a result, we will get a confidence belt with controlled false alarm probability in rejecting the null hypothesis. Our confidence belt will be slightly more conservative than the standard Feldman and Cousins's for small values of the signal.

Once that confidence interval is set, the result will be converted in equivalent gravitational wave rate by dividing for the measured efficiency of detection for each selected waveform.

In case the null hypothesis is confirmed, the result will be an upper limit on the gravitational wave rate. If the null hypothesis is rejected, the causes should be investigated to check for any problems in the analysis procedures (e.g. background estimation) or in the hardware (e.g. instrumental correlations). The investigation should include further independent checks for each detector data and code and, more important, targeted analysis to estimates arrival times and spectral amplitudes. This targeted analysis can be more powerful than the present one since it can exploit coherent methods of analysis (i.e. taking advantage on the phase informations of LIGO data with respect to AURIGA data).

6.4 Results

As the last step of the analysis, we "opened the box" to investigate the "on-source" data sets. The results can be summarized as follows. In the triple coincidence data set, 1288 events survived the LHO-sign cut (over the exchange thresholds). None of these are above the analysis threshold $\Gamma \geq 9$. In the quadruple coincidence data set no events surviving the LHO-sign cut have been found. As a result, our "on-source" data set counts no events and therefore the null hypothesis is confirmed.

To compare the resulting distribution of "on-source" events with the estimated distribution predicted by the "off-source" data sets, we have taken into account also the events under the analysis thresholds. In figure 6.11 the triple coincidence events with $\Gamma \geq 4$ which pass the LHO-sign cut on the "on-source" data set are superimposed to the distribution predicted by the "off-source" data sets. We note a good agreement between the "on-source" events and the expected distribution (within its spread).

To quantify the agreement between the 2 data sets, we have applied the Kolmogorov-Smirnov test to the "on-source" and "off-source" cumulative distributions of Γ ($F(\Gamma)$ and $S(\Gamma)$, respectively). The cumulative distributions have been empirically estimated from the Γ_i values of the coincident events, by simply counting how many events have $\Gamma_i \leq \Gamma$. Even though the resulting "off-source" distribution is sampled, it can be considered a good approximation of the model distribution since the number of "off-source" samples is about 100 times larger than the number of the "on-source" ones. The two distributions and their residuals:

$$d(\Gamma) = F(\Gamma) - S(\Gamma) \tag{6.9}$$

are shown in figure 6.12. The Kolmogorov-Smirnov statistic is simply:

$$D = max|d(\Gamma)| \tag{6.10}$$

For our "on-source" samples:

$$D = 0.01385 \ \ at \ \Gamma = 4.3926 \tag{6.11}$$

Given the number of "on-source" samples (1288) the resulting probability of getting a larger deviation, assuming the correctness of the "off-source" model, is very high, 0.6.

Once verified the compliance of the "on-source" and "off-source" data sets, we can return to consider the analysis thresholds and set the confidence intervals for the resulting null "on-source" counts. As seen in section 6.1 the number of accidental coincidences in all the "off-source" data sets can be described as a Poisson process. The known mean number of predicted accidental coincidences is $b = 0.22$ (as seen in section 6.3). We assume that also the "on-source" coincidences (n) follow a Poisson distribution with a mean given by b plus an unknown mean μ (related, for example, to a flux of gravitational waves). The probability to get n coincidences for a given μ is given by:

$$P(n|\mu) = (\mu + b)^n \exp[-(\mu + b)]/n! \tag{6.12}$$

Using the procedure described in Feldman & Cousins (1998), we can build the confidence intervals $[\mu_1, \mu_2]$ which guarantee a coverage (C.L.) of 95%. To take into account the uncertainty on b we build the confidence belts for $b = 0.22 + 3\sigma$[1] and $b = 0.22 - 3\sigma$ and take the union of the 2 belts (to be conservative). Then, we have modified the standard Feldman and Cousins belt as follows. When the null hypothesis is confirmed at 99% coverage, we consider, as the upper bound, the classical costruction of Feldman and Cousins at 95% coverage and we extend the lower bound to 0. When the null hypotesis is not verified we keep the original confidence intervals. The resulting confidence belt is shown in figure 6.13.

From figure 6.13 we can set a one-sided confidence interval for $n < 3$, or a two-sided confidence interval otherwise. In our case $n = 0$ and the upper limit we get is:

$$\begin{aligned} Upper\ limit\ 95\% &= 3.02\ \ events\,in\,the\,\text{“}on - source\text{''}\,data\,set \\ &= 0.66\ \ events/day \end{aligned} \tag{6.13}$$

The result in formula 6.13, scaled by the overall efficiency of the network, gives us the possibility to set a limit on the flux of gravitational waves of a given

[1] here $\sigma = 0.05$ as we get in section 6.3 (see equation 6.7).

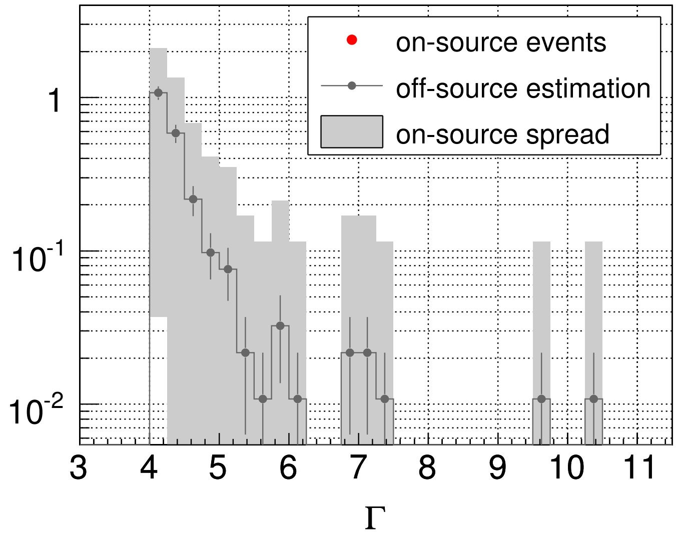

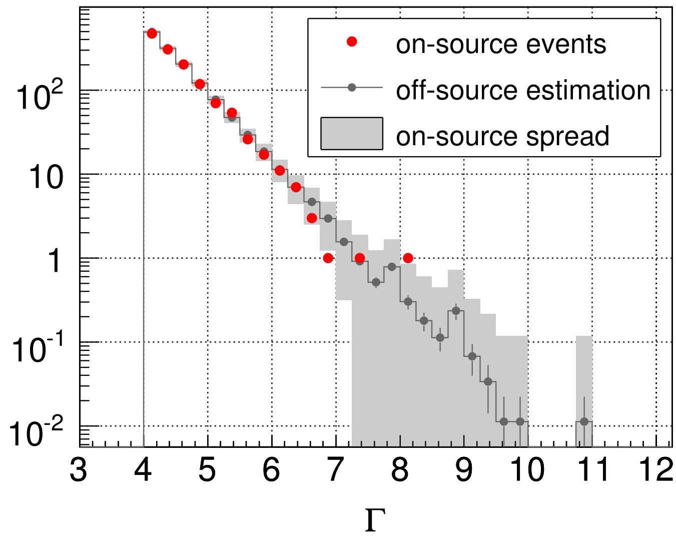

Figure 6.11: Comparison between the "on-source" data sets and the corresponding expected distribution as estimated from "off-source" data sets. On the top: quadruple coincidence AURIGA-LHO1-LHO2-LLO. On the bottom: triple coincidence AURIGA-LHO1-LHO2. In both cases, only the events with $\Gamma \geq 4$ which pass the LHO-sign cut have been considered. The analysis thresholds are (respectively) $\Gamma = 6$ and $\Gamma = 9$. We have no events above these thresholds. Gray markers and stair-step curve: distribution of the predicted accidental coincidence counts in the "on-source" data set. The distribution is just the histogram of the accidental coincidences (n) found in the "off-source" data sets scaled by the ratio of "on-source" and "off-source" livetimes (T_{on}/T_{off}, see equation 5.5). 1σ statistical uncertainties of each bin are indicated as thin gray error bars ($\sqrt{n} \cdot T_{on}/T_{off}$). Gray shadows: 1σ statistical fluctuations of the expected "on-source" event distribution (evaluated as $\sqrt{n \cdot T_{on}/T_{off}}$). Red markers: events of the "on-source" data set.

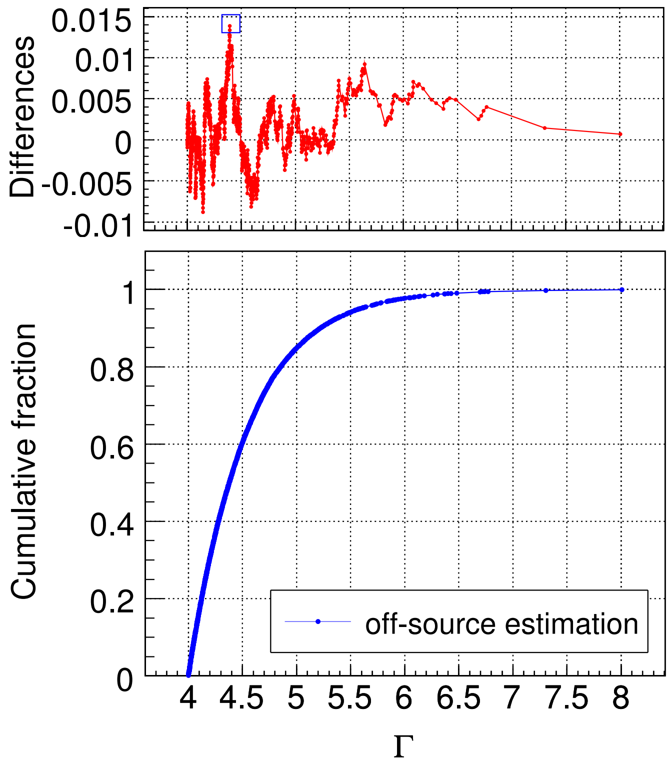

Figure 6.12: On the bottom: cumulative distribution of Γ for the "off-source" data set. On the top: differences between the "off-source" and the "on-source" data sets are shown for each value of Γ. The value of the maximum difference (Kolmogorov-Smirnov statistic D) is indicated with a blue marker and corresponds to $D = 0.01385$.

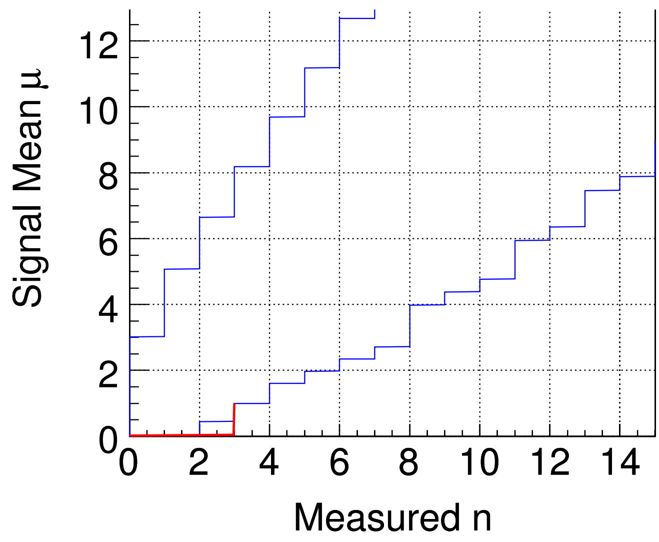

Figure 6.13: Confidence belt (based on Feldman & Cousins's procedure), for 95% C.L. confidence intervals, unknown Poisson signal mean μ and a Poisson background with $b = 0.22 \pm 3\sigma$ (evaluated from the "off-source" data sets). As described in the plan for the statistical analysis (see section 6.3.2), we modify the standard Feldman and Cousins construction in this way (red line in the plot): in case the null hypothesis is confirmed at 99% coverage, we consider the upper bound of the Feldman and Cousins construction at 95% coverage but we extend its lower bound to 0; otherwise we keep the original confidence intervals.

waveform and a given amplitude. As pointed out in section 6.3.1, the efficiency of the combined (4-fold+3-fold) data set can be written as an average of the two efficiencies (see equation 6.8). In figure 6.14 the upper limits on the event rate versus h_{rss} are shown for sine-Gaussians, Gaussians and damped sinusoids. For all the waveforms, when the efficiency approaches 1, the asymptotic behavior of the event rate at large h_{rss} is 0.66 events/day. Values of h_{rss} for which the efficiency vanishes give a rate limit which reaches infinity asymptotically. The region of the plot above each curve defines the region of h_{rss}-rate excluded by the AURIGA-LIGO search at 95% coverage or greater.

It is possible to compare figure 6.14 with similar results obtained by IGEC (Astone *et al.* (2003)) and LIGO-only analysis (LSC (2004), LSC (2005)). The asymptotic event rate at high of h_{rss} of the presented AURIGA-LIGO analysis is much higher than the one set by IGEC (0.66 events/day against 4×10^{-3}

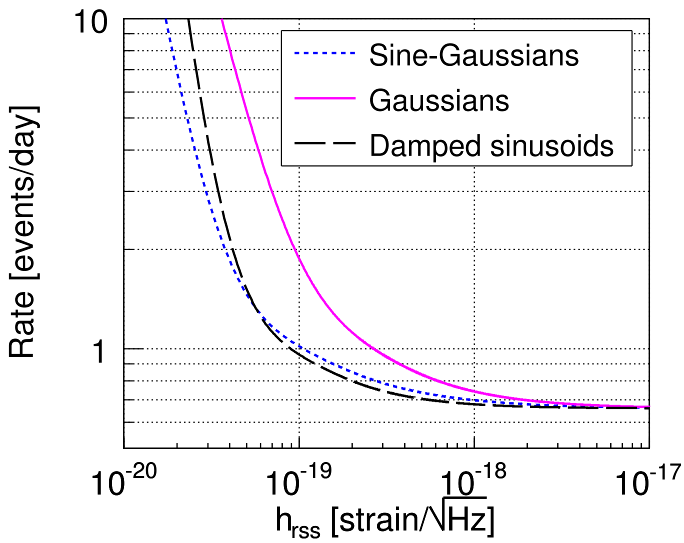

Figure 6.14: Upper limits on the event rate versus h_{rss} for the considered waveforms (sine-Gaussians at $f_0 = 900$ Hz and $\tau = 0.2$ ms, Gaussians with $\tau = 0.2$ ms, and damped sinusoids with $f_0 = 930$ Hz and damping time $\tau = 6$ ms). These curves have been built by scaling the upper limit of 0.66 events/day (95% C.L.) by the average efficiency of 4-fold and 3-fold coincidence data sets (see equation 6.8).

events/day, at 95% C.L.) while comparable with the LIGO S2 analysis (0.33 events/day, at 95% C.L.). These numbers can be easily explained by considering that, at high h_{rss}, the upper limit is inversely proportional to the observation time (much longer in IGEC analysis). At low h_{rss}, the comparison depends on the signal morphology and the assumptions on the source population and is dominated by the detection efficiency of the network. However, we can conclude that at low h_{rss} the present AURIGA-LIGO event rate is better than the IGEC one because the S_{hh} sensitivity of AURIGA (and to a greater extent that of the LIGO detectors) are better than the previous sensitivity of the bars in the IGEC 1997-2000 search, mainly because of the wider bandwidth. However, the improvement cannot be computed easily because the published IGEC result did not take into account the detection efficiency of the IGEC network for a given signal class.

The comparison with the LIGO S2 results can be performed more quantitatively by using the same signal morphology (sine Gaussian with $Q = 8.9$) and source population model (isotropically distributed in the sky). If we scale our coverage from 95% to 90% the AURIGA-LIGO resulting upper limit is 0.51 events/day. This value can be compared to the upper limit at 90% coverage set by the LIGO S2 and TAMA-LIGO S2 analysis on the sine-Gaussian with central frequency at 850 Hz and $Q = 8.9$ (see figure 6.15). Even if the sine-Gaussian waveform considered for AURIGA-LIGO efficiency curve was centered at 900 Hz, this difference in frequency does not significantly affect the comparison between the networks. In fact, it has been estimated that, for sine-Gaussians $Q = 9$, the detection efficiency of AURIGA, for central frequencies in the range 850-960 Hz, is penalized at most by 16% with respect to the one measured for central frequency 900 Hz. Therefore, the resulting upper limit of the present search for such waveforms would worsen at most by the same factor in the cited spectral range. For this sine-Gaussians, LIGO-only S2 analysis set an upper limit of 0.26 events/day (see LSC (2005)), while TAMA-LIGO S2 set an upper limit of 0.12 events/day (see Abbott *et al.* (2005b)).

In the bandwidth of sensitivity of this search, the resulting AURIGA-LIGO upper limit on the rate is worse by a factor of $\sim 2-3$ with respect to the LIGO S2 one, at the same confidence level. Taking into account the scaling of the upper limit curves due to the different observation times (LIGO S2 could use 239.5 h of on source data, double with respect to the 110 h of AURIGA-LIGO-S3) the two curves differ of about a factor 2. The same considerations on preliminary LIGO-only S3 results would give an handicap of a factor 2 (Katsavounidis (2005)). This is due to the fact that the overall network efficiency of AURIGA-LIGO is limited by the AURIGA detector.

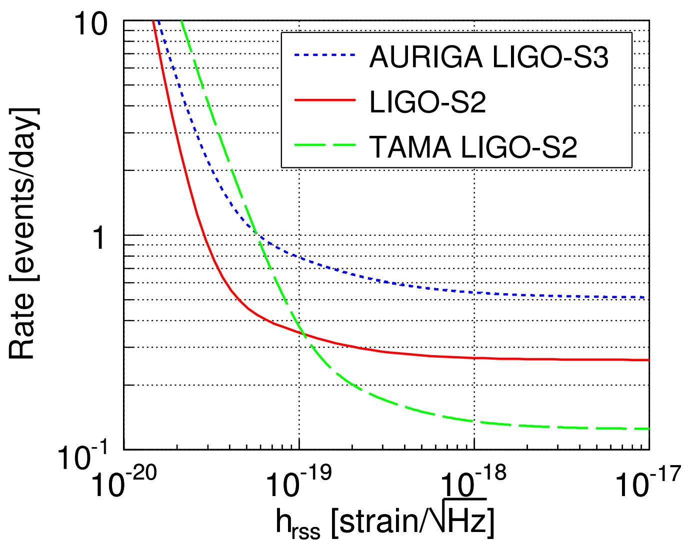

Figure 6.15: Upper limits on the event rate versus h_{rss} for the sine-Gaussian waveform in different network analysis: AURIGA-LIGO S3 (in blue), LIGO-only S2 (in red) and TAMA-LIGO S2 (in green). The sine-Gaussians considered have central frequency 900 Hz (for AURIGA-LIGO S3) and 850 Hz (for LIGO-only S2 and TAMA-LIGO S2). The Q is 8.9. In this plot, all the upper limits have been evaluated at 90% C.L. With this coverage, the upper limit rate of the AURIGA-LIGO network is 0.51 events/day and can be compared to the same value from the LIGO-only S2 analysis (0.26 events/day) and from the TAMA-LIGO S2 analysis (0.12 events/day).

Chapter 7

Conclusions

This work presents all the analysis steps and my personal conclusions on the first AURIGA-LIGO burst search. This is the first joint search for bursts by non-homogeneous detectors such as resonant and interferometric. The analysis methods have already been published in Cadonati *et al.* (2005) and in Poggi *et al.* (2006). At present, results are still under review by the 2 collaborations for a final publication. Because of the shortness of the coincidence run (2 weeks from December 24, 2003 to January 9, 2004) and the non-stationarities of AURIGA, the 2 collaborations chose to consider this data exchange as a playground for future analysis. As a consequence, it has been agreed to consider this analysis simply as a methodological study on a network of non-homogeneous detectors.

In fact, the AURIGA-LIGO analysis involved detectors based on different technologies and resulting in different spectral sensitivities, bandwidths and antenna patterns. Detectors considered here are the AURIGA bar (Legnaro, Italy), and the interferometers LHO1 (Hanford, USA), LHO2 (Hanford, USA) and LLO (Livingston, USA). The resulting network has been considered in 4-fold coincidence (i.e. AURIGA-LHO1-LHO2-LLO coincidence) and in 3-fold coincidence (i.e. AURIGA-LHO1-LHO2 coincidence).

The problem of different bandwidths has been addressed by performing a search of coherent power in the wideband LIGO interferometers around the trigger times provided by AURIGA. Obviously, the AURIGA efficiency limited the sensitivity of the network to signals showing suitable power in the 850-950 Hz spectral range. As a consequence, the choice of the target signal fell on bursts with high frequency content. In literature, the most suitable sources for such a kind of signals are black holes ring-downs, mergers of coalescing neutron stars and black holes binary systems.

The study of the AURIGA-LIGO network sensitivity has been addressed in chapter 4. In order to establish (from a geometrical point of view) which fraction of the sky can be seen by these detectors, we outlined 2 strategies to accomplish for the combination of different antenna patterns. In both cases we considered only signals with linear polarization and we completed the study with the analysis of the possibility to reorient the bar.

According to the "product-threshold" strategy, we threshold a product of all the possible pairs of antenna patterns and we require that, at least, one of these products is above a fixed threshold. To take into account the different sensitivity of the bar with respect to the LIGO ones, we introduced an "handicap factor" of 1/3 to scale the AURIGA antenna pattern. In these conditions we studied the average (over all the source directions and polarizations) of the fraction of sky "seen" by the network. We concluded that the sky coverage of the pair LHO-LLO is already very high and the addition of the AURIGA detector improves the coverage only when the threshold on the antenna pattern product is low (about 0.01). In this case, the improvement regards almost all the directions but it is limited to few percent of the sky coverage. At the same threshold, the fraction of the sky which is not seen by the LIGO-only network but is seen by the AURIGA-LIGO network is about 0.01. If we change the orientation of the AURIGA bar, these results do not change significantly. For this reason we do not consider reorienting a convenient strategy.

According to the "detector-threshold" strategy, we require that the antenna patterns of all the detectors are, singularly, above a fixed threshold. Also in this case we adopted the "handicap factor" of 1/3 to scale the AURIGA antenna pattern. The fraction of the sky (averaged over all the source directions and polarizations) "seen" by the AURIGA-LIGO network in detector-threshold strategy is 0.4582 at a threshold of 0.1. For this fraction of the sky we can guarantee a triple coincidence detection (by the three sites of Hanford, Livingston and AURIGA) and, as a consequence, a better false alarm rate. The sky coverage improves of few percent in changing the azimuth of AURIGA, so we must conclude, like in the previous strategy, that it is not of any advantage reorienting the bar.

As a consequence of these considerations, we cannot state that AURIGA improves significantly the sky coverage of the LIGO network. However, we must remember that it can give a contribution to reduce the false alarm rate, to improve the statistical confidence of detection and to localize a source (through the solution of the "inverse problem"). The study of false alarm rate has been addressed in chapter 5 and finalized in chapter 6.

Before starting the analysis, a series of data quality assessments has been applied by the AURIGA and LIGO collaborations. Of the remaining time, a 10% of the whole data set has been set aside to be used as a playground for testing the pipeline. The final observation time of the network in quadruple coincidence (AURIGA-LHO1-LHO2-LLO) is about 36 h. Moreover, we have exploited the 74 h of triple coincidence (AURIGA-LHO1-LHO2) corresponding to off-periods of LLO. These two disjoint periods of observation sum up to 110 h. In order to get an indirect measure of the accidental coincidences, we considered a series of "off-source" data sets, built by time-shifting LIGO data. Livetimes of the quadruple and triple coincidence "off-source" data sets represent more than 90 times the length of the corresponding "on-source" sets. Using the "off-source" data sets we were able to tune the thresholds and optimize the search before "opening the box" of "on-source" data and avoiding in this way biases on the statistical interpretation of the results.

The two collaborations agreed to perform a triggered search of burst sources. AURIGA produced a trigger list according to its usual analysis pipeline. After the triggers exchange, a cross-correlation search was performed on LIGO data around each candidate event using integration windows of some tens of ms. This was performed by the `CorrPower` code. In this step of the analysis, a value of Γ_i was evaluated for each pair of interferometers in correspondence of each trigger (being $10^{-\Gamma_i}$ the statistical significance of the corrrelation between 2 detectors).

The final value of Γ associated to each trigger is simply the arithmetic mean of the Γ_i from each pair, maximized over all the considered integration windows.

In this way, after the `CorrPower` process, each trigger has been characterized by a pair of variables: SNR and Γ. We chose to consider, as minimal thresholds for the analysis, $SNR = 4.5$ and $\Gamma = 4$.

In chapter 6 a tuning has been performed on these 2 thresholds by studying the "off-source" data sets which resulted, at the minimal thresholds, sufficiently Poisson distributed. The tuning resulted in the choice of $SNR = 4.5$ and $\Gamma = 6$ as the analysis thresholds for the quadruple coincidence data set and of $SNR = 4.5$ and $\Gamma = 9$ for the triple coincidence data set. It has been agreed to suppress, from the list of events above these thresholds, all the events for which the 2 Hanford detectors do not show a positive sign in the correlation (LHO-sign cut). This strategy suppressed a significant fraction of false alarms. With this requirement, the study of the "off-source" data sets predicted about 0.1 events above the analysis thresholds in the "on-source" quadruple coincidence data set. The same was expected for the triple coincidences. Moreover, for these thresholds, the estimation of the efficiency to the same waveform gave very similar results in both the sets ($h_{rss}50\% = 5.6 \times 10^{-20}/\sqrt{Hz}$ for a sine-Gaussian centered at 900 Hz and with $Q = 8.9$, being $h_{rss}50\%$ the h_{rss} at 50% efficiency).

The plan for the statistical interpretation of the results has been established before "opening the box" of "on-source" data sets. First of all, it has been agreed to consider the overall quadruple and triple observation time, making a single trial. This choice is justified by the very similar false alarm rates we get after the tuning.

The compliance between the number of events in the "on-source" and in the "off-source" data sets (null hypothesis) has to be tested; we decided to test it with a 99% of significance. In the case of an excess of coincidences in the "on-source" data set, we might not exclude a correlation of the detector noises between the possible causes. For this reason, in this case, more investigations would be necessary both on the analysis pipeline and on the found candidate events. The 2 collaborations agreed to set confidence intervals according to Feldman and Cousins procedure with, at least, a coverage of 95%. The construction of the confidence belt and the subsequent confidence intervals have been set by taking into account the uncertainty on the mean accidental counts (conservatively we considered $\pm 3\sigma$).

In the "on-source" data set we did not find any event over the chosen analysis thresholds which survived to the LHO-sign cut and therefore the null hypothesis is confirmed. The only "on-source" events found occurred in the 3-fold set under the analysis thresholds; these events have been verified to be compliant with the estimated "off-source" distribution.

The upper limit which resulted from the absence of events above the analysis thresholds is 0.66 events/day at 95% confidence level. This rate has been converted in equivalent gravitational wave rate by dividing for the detection efficiency corresponding to the considered waveforms (sine-Gaussians, Gaussians and damped sinusoids). For each waveform, the efficiencies of quadruple coincidence and the triple coincidence data sets have been averaged (weighted for their respective livetimes) to get the efficiency of the overall data set. The resulting rate versus h_{rss} exclusion plots are very similar to the ones obtained by LIGO-only S2 analysis and TAMA-LIGO S2 analysis.

After the period of simultaneous observation of AURIGA and LIGO considered in this analysis (December 24, 2003 - January 9, 2004), both detectors have been improved (see figure 7.1). AURIGA is taking data with a very satisfactory quality since December 2004 (as described in section 2.3.2). The duty cycle has been improved to above 90% after the last suspension upgrade in May 2005. The AURIGA operating temperature remained 4.5 K and therefore the sensitivity improvement has been limited to a factor 2 in signal amplitude, thanks to the disappearance of the spurious noise lines. LIGO detectors have performed a 4 week scientific run in early 2005 (run S4) and started a long term observation since mid November 2005 (run S5). Their S_{hh} sensitivity improved significantly, being currently about one order of magnitude better than the one of AURIGA within its bandwidth (see figure 7.1). At present, a collaborative search is possible between the LIGO observatories and the four bar detectors participating to the IGEC-2 collaboration (ALLEGRO, AURIGA, EXPLORER, NAUTILUS, see Prodi (2005)). Given the current sensitivity handicap of the bar detectors, their main contribution would be the opportunity to add significant confidence of detection to candidates identified by LIGO at high SNR. The added confidence would rely on the very low false alarm probability of the bar observatory. Moreover, the addition of a detector to the LIGO network consents to solve the inverse problem and localize a source.

As for what concerns the near future, we plan to lower the operating temperature of AURIGA to 0.1 K in 2007, and we expect to reach $S_{hh} \sim 3 \cdot 10^{-22}/\sqrt{Hz}$ with a slightly improved bandwidth (see figure 7.2). This figure would be very close to the sensitivity now achieved by the LHO2 detector. In that scenario, the current analysis could be repeated as is, getting to a very similar picture for what concerns the efficiency of the LIGO-only search to a possible AURIGA-LIGO search. Of course, more detectors are planning to begin observations, above all the wide-band detectors VIRGO (see the VIRGO web page) and GEO600 (see the GEO web page): these news will greatly affect the scenario and the methodologies of future searches for gravitational waves. In particular, it will be possible to develop and implement methods of network analysis which take advantage also of the phase information (coherent methods, see Rakhmanov & Klimenko (2005) and Parameswaran (2005)) and solve the inverse problem of reconstructing all the gravitational wave parameters.

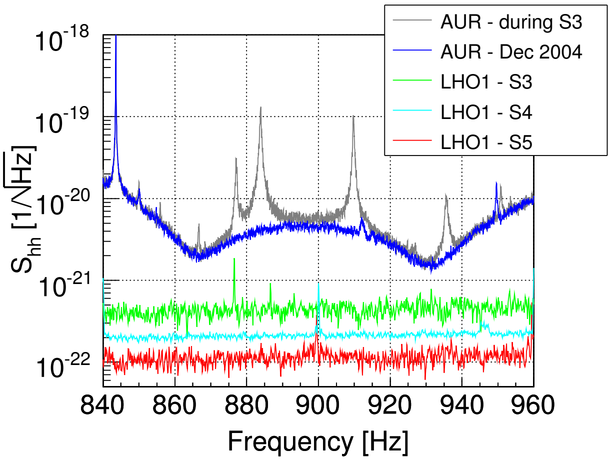

Figure 7.1: AURIGA strain sensitivity during the coincidence run (in gray) and with the new suspensions (in blue). LHO1 strain sensitivity during the coincidence run (in green), during S4 (in cyan) and during S5 (in red). (Courtesy of LIGO laboratory).

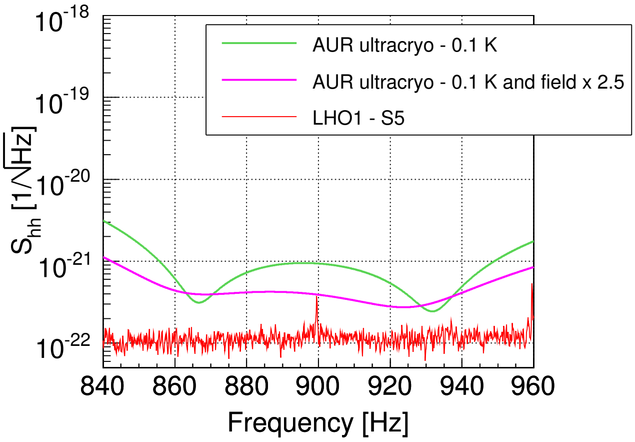

Figure 7.2: Predicted strain sensitivity for AURIGA in ultracryogenic mode: in green temperature at 0.1 K, in magenta temperature at 0.1 K and with a transducer bias field increased by a factor 2.5. In red the LHO1 noise spectra during S5. (Courtesy of LIGO laboratory).

Appendix A

The CorrPower analysis

Because of the typically unknown (or poor modelled) nature of bursts, the search for them cannot consider a precise template but have to be as broad as possible. By renouncing to a template waveform we renounce also at the the possibility to get an *optimal* search and to the parameters to discriminate it.

A *correlation search* is performed on 2 time series:

$$\begin{aligned} s_1(t) &= h(t - t_1) + n_1(t) \\ s_2(t) &= h(t - t_2) + n_2(t) \end{aligned} \tag{A.1}$$

where h is the signal, n_i is the noise detected by the i^{th} detector and s_i is the output from that detector. The cross-correlation of signals in equation A.1 is defined as:

$$\begin{aligned} C(t, t_w, t_{off}) &= \int_{-t_w/2}^{+t_w/2} s_1(t') s_2(t' + t_{off}) dt' \\ &\approx \int_{t_w} h^2(t) dt + \int_{t_w} n_1(t) n_2(t) dt \end{aligned} \tag{A.2}$$

where t_w is the adopted integration window. First term in equation (A.2) is called h_{rss} for that signal (see equation 3.4), while the second gives 0.

A.1 CorrPower algorithm

`CorrPower` is a Cross-Correlation based algorithm thought to perform a gravitational burst search on LIGO data in a triggered or untriggered mode (Cadonati & Marka (2005)). This kind of software permits several modalities of search: first of all it consents a cross-correlation between two or more interferometers and it generates a list of events on the base of an *excess of coherent power*. As a second point, it permits to "promote" to event a candidate which passes the *r-statistic consistency test* (see next section). At least, CorrPower can perform a search of bursts triggered by an external source (e.g. triggered by GRBs events, as in Mohanty *et al.* (2004)).

The general strategy of this software is to detect eventual excesses of power in the coherent components of detectors' data streams. For doing this, the r-statistic test is exploited.

A.1.1 The r-statistic test

The *r-statistic test* is a consistency test included in the LIGO burst analysis from the second science run (S2) and which demonstrated to be capable of suppress the burst false alarm rate by 2-4 orders of magnitudes (Cadonati (2004)). This test, which purpose is to find accidental coincidence between two or more detectors, is based on a statistic defined as:

$$r = \frac{\sum_i (x_i - \overline{x})(y_i - \overline{y})}{\sqrt{\sum_i (x_i - \overline{x})^2}\sqrt{\sum_i (y_i - \overline{y})^2}} \tag{A.3}$$

where x_i and y_i are the two sequences we want to correlate. Equation (A.3) returns 1 in the case of perfect correlation and -1 in the case of perfect anti-correlation. If there is not any correlation between x_i and y_i, we expect from equation (A.3) a Gaussian distribution with a 0 mean and $\sigma = 1/\sqrt{N}$ (with $N =$ number of point in which calculate r) (Cadonati (2004)). Equation (A.3) detects each component of correlation between x_i and y_i as a deviation respect to the normal distribution. The number N of points considered for the evaluation of r must be established as a compromise between a too large window (which involves loosing the signal in too much averages) and a too narrow window (which means a poor statistic).

In an application of equation (A.3) to real data, we must consider several time shifts (k) and several integration windows between the different time series l and m. Hence, for each interval j, we will have a value of r which corresponds to:

$$r^k_{plmj} = \frac{\sum_i (x^i_{plmj} - \overline{x}_{plmj})(y^{i+k}_{plmj} - \overline{y}^k_{plmj})}{\sqrt{\sum_i (x^i_{plmj} - \overline{x}_{plmj})^2}\sqrt{\sum_i (y^{i+k}_{plmj} - \overline{y}^k_{plmj})^2}} \tag{A.4}$$

The distribution which results from equation (A.4) is compared to a zero mean normal distribution. If the distribution doesn't fit with a Gaussian, the *one-sides significance*:

$$S^k_{plmj} = erfc\Big(|r^k_{plmj}|\sqrt{\frac{N}{2}}\Big) \tag{A.5}$$

and the *confidence*:

$$C^k_{plmj} = -log_{10}(S^k_{plmj}) \tag{A.6}$$

are evaluated. The confidence assigned to each interval j for the cross-correlation of the pair $l - m$ is:

$$\gamma_{plmj} = max_k C^k_{plmj} \tag{A.7}$$

Equation (A.7) refers to the pair of detectors $l - m$, but if (more in general) we are considering a network of more than 2 detectors, we must resume all the γ_{plmj} in one single value, which depends only on the integration window p:

$$\gamma_{pj} = \frac{1}{N_{ifo}(N_{ifo} - 1)} \sum_{l \neq m} \gamma_{plmj} \tag{A.8}$$

where N_{ifo} is the number of pairs we can form within the network. Now, if we want to resume also the informations about the integration window p and we desire to define a correlation confidence which is univocally associated to the event, we must maximaze γ_{pj} first on the intervals j and then on p:

$$\Gamma_{pj} = max_p[max_j \gamma_{pj}] \tag{A.9}$$

Finally, the waveform consistency test is performed by comparing Γ with a chosen threshold β. If $\Gamma > \beta$ the event has passed the test.

Appendix B

Template waveforms

To tune the search algorithm and interpret the results of the analysis, the LIGO-AURIGA working group has focused its analysis on particular classes of signals and tuned their parameters so that the waveforms result fully included in the narrow band of AURIGA.

The efficiency of the network in 4-fold and 3-fold coincidence (see section 6.2) have been studied for the following classes of simulated signals.

B.1 LA_SG2 class: Gaussians, sine-Gaussians and cosine-Gaussians

Gaussians waveforms (very often used in LIGO analysis) represents an optimal signal (even if no known astrophysical source is associated to them) because of their simple interpretation in the contest of the analysis. For the injections referring to this MDC set, we assume a null $\times$-polarization, while the $+$-polarization contains a Gaussian-modulated signal. The waveform is randomly selected between the three possible choices listed below.

The definition for a *Gaussian* waveform is:

$$\begin{aligned} h_+(t) &= h_{peak}\, \mathrm{e}^{-(t-t_0)^2/\tau^2} \\ h_\times(t) &= 0 \end{aligned} \tag{B.1}$$

In definition B.1 the strain associated to the cross polarization is chosen to be zero. The plus polarization, instead, is shaped as a Gaussian signal. The same rule is used in the sine-Gaussians and cosine-Gaussians templates. The parameter τ is chosen as $\tau = 0.2$ ms, in this way the maximum fraction (5%) of the signal energy falls in AURIGA band. This signal is not properly the best choice when dealing with narrow band detectors such as AURIGA but it has been chosen as a standard reference function.

For tuning the analysis, *sine-Gaussians* signals (as those used in LSC (2004) and LSC (2005)) of the form:

$$\begin{aligned} h_+(t) &= h_{peak}\, \mathrm{e}^{-(t-t_0)^2/\tau^2} \sin(2\pi f_0(t-t_0)) \\ h_\times(t) &= 0 \end{aligned} \tag{B.2}$$

have been injected in the data stream, with central frequency $f_0 = 900\, Hz$, $\tau = 2/f_0 = 2.2\, ms$ and $Q \equiv \sqrt{2}\pi f_0 \tau = 8.9$. f_0 has been chosen to be in the middle of the band of interest.

A variation on the last template are the *cosine-Gaussians* signals:

$$\begin{aligned} h_+(t) &= h_{peak}\, \mathrm{e}^{-(t-t_0)^2/\tau^2} \cos(2\pi f_0(t-t_0)) \\ h_\times(t) &= 0 \end{aligned} \tag{B.3}$$

where f_0 and τ are defined as in equation B.2. The analysis pipeline developed for LIGO-AURIGA data exchange makes no distinction between sine and cosine-Gaussians, for this reason signals of the class in equation B.2 or in equation B.3 can be merged in one single case (which we call, in general, *sine-Gaussians*).

B.2 LA_DS2 class: damped sinusoids

Another kind of *ad-hoc* built-in functions, are the *damped sinusoids*. They can be associated to the behavior of perturbed systems, such as ringing black holes in their late stages (see section 3.1).

The definition of damped sinusoid is:

$$h_+(t) = \begin{cases} h_{peak}\,\frac{1}{2}(1+\cos^2\iota)\;\cos(2\pi f_0 t+\delta)\,\mathrm{e}^{-t/\tau} & t \geq 0\,, \\ h_{peak}\,\frac{1}{2}(1+\cos^2\iota)\;\cos(2\pi f_0 t+\delta)\,\mathrm{e}^{t/(10\tau)} & t < 0\,, \end{cases} \tag{B.4}$$

$$h_\times(t) = \begin{cases} h_{peak}\,\cos\iota\;\sin(2\pi f_0 t+\delta)\,\mathrm{e}^{-t/\tau} & t \geq 0 \\ h_{peak}\,\cos\iota\;\sin(2\pi f_0 t+\delta)\,\mathrm{e}^{t/(10\tau)} & t < 0 \end{cases} \tag{B.5}$$

In equation B.5, the +-polarization behaves as a damped cosine, the $\times$-polarization as a damped sine. In the LIGO-AURIGA analysis, we considered as null the arbitrary phase δ of equation B.5. The angle ι corresponds to the inclination of the source and has been chosen so that $\cos\iota$ is uniformly distributed over the range $[-1, 1]$. All the signals have "intrinsic" amplitude $A = 7.5 \times 10^{-21}/\sqrt{\mathrm{Hz}}$ for each polarization separately but each polarization must be rescaled according to the inclination ι:

$$\begin{aligned} hrss_+ &= \frac{1}{2}A(1+\cos^2\iota); \\ hrss_\times &= A\cos\iota. \end{aligned} \tag{B.6}$$

As a central frequency for equation B.5 we have used $f_0 = 930\,Hz$. For the damping time τ, we have considered $\tau = 6\,ms$ (which correspond, for a black-hole ring-down, to masses and spins of approximately $(M, a) = (30M_\odot, 0.98)$ respectively (Echeverria (1989); Flanagan & Hughes (1998)).

Bibliography

Abbott, B. *et al.*. Search for gravitational waves from binary balck hole inspiral in LIGO data. `arXiv:gr-qc/0509129`. 3.1

Abbott, B. *et al.* (2005b). Upper limits from the LIGO and TAMA detectors on the rate of gravitational-wave bursts. *Phys. Rev.* **D 72**, **122004**, `arXiv:gr-qc/0507081`. 3.2, 6.4

Allen, B. Gravitational Wave Detector Sites. `arXiv:gr-qc/9607075`. 2.2

Ando, M. *et al.* (2005). Observation results by the TAMA300 detector on gravitational wave bursts from stellar-core collapses. *Phys. Rev.* **D 69**, **082002**. 3.2

Astone, P. *et al.* (1993). Long-term operation of the Rome “Explorer” cryogenic gravitational wave detector. *Phys. Rev.* **D 47**, **362**. 2.2

Astone, P. *et al.* (1994). Coincidence experiments between interferometric and resonant bar detectors of gravitational waves. *Class. Quantum Grav.*, **11**, 2093–2112. 2.2

Astone, P. *et al.* (1997). The Gravitational Wave Detector NAUTILUS Operating at T= $0.1\,k$. *Astrop. Phys.* **7**, **231**. 2.2

Astone, P. *et al.* (2003). Methods and results of the IGEC search for burst gravitational waves in the years 1997-2000. *Phys. Rev.* **D 68**, **022001**. 2.2, 3.2, 3.3, 4.1, 6.4

AURIGA. Web page: `http://www.auriga.lnl.infn.it/`. 2.2, 2.3.1

Baggio, L. *et al.* (2004). Proposal for the First AURIGA-LIGO Joint Analysis. LIGO-T040202-00, LIGO and AURIGA internal report. 3.3

Baggio, L. *et al.* (2005). 3-mode detection for widening the bandwidth of resonant gravitational wave detectors. *Phys. Rev. Lett.*, **94**, 241101, `arXiv:gr-qc/0502101`. 2.3.2, 5.2

Baker, J. *et al.* (2002). Modeling gravitational radiation from coalescing binary black holes. *Phys. Rev.* **D 65**, **124012**, `arXiv:astro-ph/0202469`. 3.1

Bignotto, M. *et al.* (2005). New suspensions system for the gravitational wave bar detector AURIGA. *Rev. Sci. Instrum.* **76**, **084502**. 2.3.2, 5.2

Cadonati, L. (2004). Coherent Waveform Consistency Test for LIGO Burst Candidates. *Class. Quantum Grav.*, **21**, S1695–S1703, `arXiv:gr-qc/0407031`. 5.4, A.1.1, A.1.1

Cadonati, L. & Marka, S. (2005). Corrpower: a cross-correlation-based algorithm for triggered and untriggered gravitational-wave burst searches. *Class. Quantum Grav.*, **22**, S1159–S1167. 3.3, A.1

Cadonati, L. *et al.* (2005). The AURIGA-LIGO Joint Burst Search. *Class. Quantum Grav.*, **22**, S1337–S1347. (document), 3.3, 3.1, 3.2, 6, 7

Cesaracciu, A. *et al.* (2003). *A Modular Object Oriented Data Acquisition System for the Gravitational Wave AURIGA Experiment*. La Jolla, San Diego, proceeding of the "CHEAP 2003 conference". 2.3.2, 5.2.1

Chakrabarty, I. (1999). Gravitational Waves: An Introduction. 2

Crivelli-Visconti, V. *et al.* (2000). *The Auriga Ultracryogenic Test Facility: a New Capacitive Resonant Transducer*. S. Meshov, AIP Conference Proceedings, New York, in "Gravitational Waves", proceeding of the "Third Edoardo Amaldi Conference". 2.3.1

Cutler, C. *et al.* (1993). The Last Three Minutes: Issues in Gravitational-Wave Measurement of Coalescing Compact Binaries. *Phys. Rev. Lett* **70**, **20**, 2984–2987. 3.1

DIMMELMEIER, H., FONT, J.A. & MULLER, E. (2002). Relativistic simulations of rotational core collapse. II. Collapse dynamics and gravitational radiation. *Astron. Astrophys.* **393**, **523**, arXiv:astro-ph/0204289. 3.1

ECHEVERRIA, F. (1989). Gravitational-wave measurements of the mass and angular momentum of a black hole. *Phys. Rev.* **D 40**, **10**. B.2

FATTORI, S. Risultati del primo run scientifico del rivelatore di onde gravitazionali AURIGA-II. Degree thesis. Unpublished, (in italian). See http://www.auriga.lnl.infn.it/auriga/papers_src/tesi_fattori.PDF. 5.2

FELDMAN, G. & COUSINS, R. (1998). Unified approach to the classical statistical analysis of small signals. *Phys. Rev.* **D 57**, 3873–3889. (document), 6.3.2, 6.4, 6.13

fftw. Web page: http://www.fftw.org. 5.2.1

FINN, L.S. (2003). S3 Playground Selection. LIGO-T030256-00-Z, LIGO internal report. 5.1.1

FLANAGAN, E.E. & HUGHES, S.A. (1998). Measuring gravitational waves from binary black hole coalescences. I. Signal to noise for inspiral, merger, and ringdown. *Phys. Rev.* **D 57**, **4535**. 3.1, 3.3.1, B.2

FrameLib. Web page: http://wwwlapp.in2p3.fr/virgo/FrameL. 5.2.1

GEO. Web page: http://www.geo600.uni-hannover.de/. 2.2, 7

GIFFARD, R. (1976). Ultimate sensitivity limit of a resonant gravitational wave antenna using a linear motion detector. *Phys. Rev.* **D 14**, 2478–2486. 2.3.1

GURSEL, Y. & TINTO, M. (1989). Near optimal solution to the inverse problem for gravitational-wave bursts. *Phys. Rev.* **D 40**, **12**, 3884–3938. 2.2, 4.1.2

Handbook for the 1st LIGO-AURIGA analysis tools. http://ligo.au.tn.infn.it/Forum/Attachments/doc/index.html. 1, 5.3

INFN (Istituto Nazionale di Fisica Nucleare). Web page: http://www.infn.it/. 1

KATSAVOUNIDIS, E. Searches for gravitational-wave bursts with LIGO. Slides of the talk for the "Sixth Edoardo Amaldi Conference" in: http://tamago.mtk.nao.ac.jp/amaldi6/07.da2/Thu1125_bwg-amaldi6-v3.ppt. 6.4

lal. Web page: http://www.lsc-group.phys.uwm.edu/lal. 5.2.1

LDAS web page. http://www.ldas-sw.ligo.caltech.edu/cgi-bin/index.cgi. 6.2

LIGO. Web page: http://www.ligo.caltech.edu/. 2.2

LIGO-AURIGA MoU (2004). LIGO-M040010-00-M and http://www.auriga.lnl.infn.it/auriga/MOU.html. 1

LIGO Parameter Estimation web page. http://emvogil-3.mit.edu/~zanolin/parameter_estimation.html. 3.3

LIGO Segment data quality repository on the web. http://gallatin.physics.lsa.umich.edu/~keithr/S3DQ/. 5.1.3

LIGOtool web page. http://www.ldas-sw.ligo.caltech.edu/ligotools/segments/. 5.1.1, 5.1.3

LSC (2004). First upper limits from LIGO on gravitational-wave bursts. *Phys. Rev.* **D 69**, **102001**, arXiv:gr-qc/0312056. 3.2, 3.3, 5.1.1, 6.2, 6.4, B.1

LSC (2005). Upper limits on gravitational wave bursts in LIGO's second science run. *Phys. Rev.* **D 72**, **062001**, arXiv:gr-qc/0505029. 3.2, 3.3, 5.1.1, 5.4, 6.2, 6.4, B.1

MAUCELI, E. *et al.* (1996). The Allegro gravitational wave detector: Data acquisition and analysis. *Phys. Rev.* **D 54**, **1264**. 2.2

MDC Matlab and tcl scripts repository. The MDC Matlab and tcl scripts and log files are available publicly at http://www.ligo.caltech.edu/~psutton/MDC/S3_LIGO-AURIGA/. 6.2

MEZZENA, R. *et al.* (2001). Sensitivity enhancement of Quantum Design dc superconducting quantum interference devices in two-stage configuration. *Rev. Sci. Instrum.*, **72**, 3694. 2.3.2

MISNER, C., THORNE, K. & WHEELER, J. (1973). *Gravitation*. W. H. Freeman Ed, New York. 2, 2.1

mkfilter. Web page: http://www-users.cs.york.ac.uk/~fisher/mkfilter. 5.2.1

MOHANTY, S.D. *et al.* (2004). Search algorithm for a gravitational wave signal in association with gamma ray burst GRB030329 using the LIGO detectors. *Class. Quantum Grav.*, **21**, S1831–S1837. A.1

NYQUIST, H. (1928). Thermal agitation of electric charge in conductors. *Phys. Rev.* **32**, 110–113. 2.3.1

OTT, C.D. *et al.* (2004). Gravitational waves from axisymmetric, rotational stellar core collapse. *Ap. J.*, **600**, `arXiv:astro-ph/0307472`. 3.1

PARAMESWARAN, A. Implementing the null-stream veto in the network analysis of gravitational-wave bursts. Slides of the talk for the GWDAW 10 Conference in: http://www.phys.utb.edu/GWDAW10/other/files/AP0001_AjithParameswaran.pdf. 7

POGGI, S. *et al.* (2006). Status of the LIGO-AURIGA Joint Burst Search. *Submitted to the proceeding of the "Sixth Edoardo Amaldi Conference"*. 3.3, 7

PRADIER, T. *et al.* (2001). Efficient filter for detecting gravitational wave bursts in interferometric detectors. *Phys. Rev.* **D 63**, **042002**. 3.2

PRICE, J. (1987). Optimal design of resonant-mass gravitational wave antennas. *Phys. Rev.* **D 36**, 3555–3570. 2.3.1

PRODI, G. Status of the IGEC-2 joint burst search. Slides of the talk for the "Sixth Edoardo Amaldi Conference" in: http://tamago.mtk.nao.ac.jp/amaldi6/07.da2/Thu1005_134Prodi.ppt. 7

RAKHMANOV, M. & KLIMENKO, S. (2005). A cross-correlation method for burst searches with networks of misaligned gravitational-wave detectors. *Class. Quantum Grav.*, **22**, S1311–S1320. 7

root. Web page: http://root.cern.ch. 5.2.1, 5.3

SUTTON, P. Checks on LIGO-AURIGA MDCs on: http://www.ligo.caltech.edu/~psutton/MDC/S3_LIGO-AURIGA/LA_SG1/Test/mdc_checks.html. 6.2

SYLVESTRE, J. (2002). Time-frequency detection algorithm for gravitational wave bursts. *Phys. Rev.* **D 66**, **102004**. 3.2

TAFFARELLO, L. The status of the AURIGA detector. Slides of the talk for the "Sixth Edoardo Amaldi Conference" in: http://tamago.mtk.nao.ac.jp/amaldi6/04.scd/Tue1015_AurigaStatus.ppt. 2.3.2

TAMA. Web page: http://tamago.mtk.nao.ac.jp/. 2.2

TAYLOR, J.H. (1994). Binary pulsars and relativistic gravity. *Rev. Mod. Phys.*, **66**, 711–719. 3.1

THORNE, K. (1987). *300 Years of Gravitation*. S. W. Hawking and W. Israel, Cambridge University Press, Cambridge, England. 3.1

THORNE, K. (1995). Gravitational Waves. 3.1

VINANTE, A. (2006). Present performance and future upgrades of the AURIGA capacitive readout. *Submitted to the proceeding of the "Sixth Edoardo Amaldi Conference"*. 2.3.2

VINANTE, A. *et al.* (2001). Dc superconducting quantum interference device amplifier for gravitational wave detectors with a true noise temperature of 16 μk. *Appl. Phys. Lett.*, **79**, 2597–2599. 2.3.2

VINANTE, A. *et al.* (2002). A 200$\hbar$ two-stage dc SQUID amplifier for resonant gravitational wave detectors. *Class. Quantum Grav.*, **19**, 1979–1984. 2.3.2

VIRGO. Web page: http://www.virgo.infn.it/. 2.2, 7

Yakushin, I., Klimenko, S. & Rakhmanov, M. (2004). MDC frames for S2 burst analysis. LIGO-T040042-00-Z-00 D, LIGO internal report. 6.2

Zendri, J.P. *et al.* (2002). Status report and near future prospects for the gravitational wave detector AURIGA. *Class. Quantum Grav.*, **19**, 1925–1933. 2.3.2

Zendri, J.P. *et al.* (2003). *Status report of the gravitational wave detector AURIGA*. Dumarchez and J. Tran Thanh Van, The Gioi Publishers, Vietnam, in "Gravitational Waves and Experimental gravitation", proceeding of the "XXXVIIIth Moriond Workshop". 2.3.2, 5.2

Zwerger, T. & Muller, E. (1997). Dynamics and gravitational wave signature of axisymmetric rotational core collapse. *Astron. Astrophys.*, **320**, 209. 3.1

Acknowledgements

I would like to thank all the components of the LIGO group of MIT for giving me the opportunity to work within their team for 2 months.

I am particularly grateful to Laura Cadonati for generously sharing her knowledge and for the help during my stay in Boston.

I would also like to acknowledge all components of the Joint Working Group who contributed to the realization of the AURIGA-LIGO data exchange.

I thank my supervisor Giovanni Prodi for providing me the opportunity to contribute to this work.

A special thanks to Andrea Vinante for his encouragement, his observations and comments, and for the help in the review of this thesis.

I would like to thank Alessandro Mion and Paola Leaci for sharing the happy (and not) experiences of this PhD.

I am grateful to Renato Mezzena whose assistance was vital in solving the (daily) problems with my PC during the first years of my PhD. With him, I thank Paolo Falferi, Jean Pierre Zendri, Luca Taffarello and the other experimentalists who patiently tolerate my presence in the lab during the "experimental hours".

Last, but not least, I extend my sincere gratitude to whom, in the AURIGA group, contributed to support my work with suggestions and assistance.